Studies of the Timing Behaviour of the ATLAS Pixel Detector

Masterarbeit
zur Erlangung des akademischen Grades
Master of Science
(M.Sc.)

dem Fachbereich Physik der
Universität Siegen

vorgelegt von
Michael Köhler

August 2008

Contents

1 Introduction **4**

2 LHC and ATLAS Detector **6**
2.1 Large Hadron Collider 6
2.2 ATLAS Detector 8
2.2.1 Inner Detector 8
2.2.2 Calorimeter System 11
2.2.3 Muon Spectrometer 12
2.2.4 Trigger and Data Acquisition System 13

3 Physics at the LHC **15**
3.1 Standard Model 15
3.2 Higgs Searches at the LHC 17

4 Semiconductor Detectors **19**
4.1 Energy Transfer of Particles in Semiconductors 19
4.2 Principles of Semiconductor Detectors 22
4.3 Radiation Damage 23

5 The ATLAS Pixel Detector **26**
5.1 Overall Layout 26
5.2 The Sensor 28
5.3 The Front-End Chip 30
5.4 The Module Controller Chip 34
5.5 Pixel Detector Readout 36
5.5.1 The Readout Electronics Crate 37
5.5.2 Optical Data Transmission 37
5.5.3 The Readout Subsystem 38

6 Timing Issues **39**
6.1 Timewalk Effect 39
6.2 Timing Adjustments 41
6.3 Timing Related Calibration Scans 42
6.3.1 Threshold Scan 42
6.3.2 Analogue T0 Scan 43
6.3.3 Intime Threshold Scan 45
6.3.4 Timewalk Scan 45

6.4 Timewalk Parameterisation 47
6.5 Temperature Dependency of Timing Scans 49
6.5.1 Temperature Dependency of the Analogue T0 Scan 50
6.5.2 Temperature Dependency of the Intime Threshold Scan 53
6.5.3 Temperature Dependency of the Timewalk Scan 54

7 Timing Studies with the Cosmics Test 60
7.1 Cosmics Test Setup 60
7.2 Timing Studies 61
7.2.1 Analysis Method 61
7.2.2 Results 62

8 Timing Studies with the ToothPix Setup 64
8.1 The ToothPix Setup 64
8.2 Measurement Procedure 65
8.2.1 Tuning 66
8.2.2 Data Taking 68
8.3 Determination of the True Delay 68
8.4 Calibration Parameters 70
8.4.1 ToT Calibration 70
8.4.2 Timewalk Parameters 75
8.4.3 Strategies for Calibration Parameters 76
8.5 LVL1A Fit Method 77
8.5.1 Input Data 77
8.5.2 Simulation 77
8.5.3 Fit 79
8.5.4 Error Analysis 82
8.5.5 Results 85
8.6 Minimum ToT Method 91
8.6.1 Efficiency 91
8.6.2 Error Analysis 92
8.6.3 Results 93

9 Conclusion and Outlook 98

A Temperature Dependency of Timing Scans 101
A.1 Results of Timing Scans at Different Temperatures 101
A.2 MCC Strobe Delay Line Calibration with TurboDAQ 104

B Threshold Scan 107

Acronyms and Abbreviations 108

Bibliography 111

Acknowledgements 116

Chapter 1

Introduction

ATLAS (A Toroidal LHC Apparatus) is one of the particle detectors currently being commissioned at the Large Hadron Collider (LHC). The LHC is a new proton-proton collider at CERN, the European Organization for Nuclear Research. It is designed to accelerate bunches of protons in two counter-circulating beams up to an energy of 7 TeV. The beams are brought to collision at four points along the circumference of the LHC. The first collisions are expected for the second half of 2008. Chapter 2 of this thesis introduces the LHC and the ATLAS detector. ATLAS is designed as a general purpose detector in order to investigate a wide range of particle physics topics. The Standard Model of particle physics and one of the most important topics of research at ATLAS, the search for the Higgs boson, are overviewed in Chapter 3.

Once fully commissioned, the LHC produces bunch crossings every 25 ns. Each collision creates numerous particles and hence numerous hits in the detector. All hits are temporarily stored in the front-end electronics of the sub-detectors. Due to the large amount of data, only events which promise to contain "interesting" physics can be read out. The selection is achieved by a trigger mechanism, which issues the readout of the data recorded by the sub-detectors for a certain bunch crossing. To ensure that the correct data can be read out, a Bunch Crossing Identifier (BCID) is assigned to each hit. For the correct assignment of the BCID's to the hits, timing adjustments are required for the different sub-detectors. The timing is adjusted by delaying the clock signal, which is sent to the sub-detectors.

This thesis investigates methods to determine the necessary timing adjustments for the ATLAS Pixel Detector. The Pixel Detector employs a silicon sensor and is the innermost tracking sub-detector. It is designed to provide three measurement points per track for charged particles. After an introduction into the basics of semiconductor detectors in Chapter 4, the ATLAS Pixel Detector is described in Chapter 5.

In this context of timing adjustments, it is important to consider the timewalk effect: it leads to the fact that hits, which deposit a low charge in the sensor, are detected later than hits, which deposit a high charge in the sensor. This requires accurate timing adjustments such, that the highest charge hits are detected well at the beginning of a clock window in order to minimise the number of hits falling into a later readout window. The timewalk

effect and implications on the readout of the Pixel Detector are described in Chapter 6. Also, the temperature dependency of timing related characteristics of the Pixel Detector is discussed in this chapter.

Chapter 7 gives a summary of studies investigating the timing behaviour of the Pixel Detector with data from cosmic rays. With those studies, the delay between the clock edges and detection of the highest charge hits is determined for each pixel module separately. The knowledge of these delays is necessary for the determination of the required timing adjustments. A validation of the methods to determine the delay is presented in Chapter 8. The Chapter describes test measurements with adjusted delays between the clock edges and the detection of the highest charge hits, performed at a Pixel Detector test setup at CERN. The analysis is performed similarly to the analysis of the data from cosmic rays. Then, the determined delays are compared to the adjusted delays in order to investigate the systematic error.

Chapter 2

LHC and ATLAS Detector

2.1 Large Hadron Collider

The Large Hadron Collider (LHC) [B+04b] is the world's largest particle accelerator located at CERN, the European Organization for Nuclear Research. It is currently being commissioned and first particle collisions are forseen for the second half of 2008. The circular collider is housed in the tunnel of the former Large Electron-Positron Collider (LEP), which has a circumference of 26.7 km and a depth between 50 and 175 m underground. The LHC produces collisions either between protons or ions. Once fully commissioned, collisions will happen at a centre of mass energy of $\sqrt{s} = 14$ TeV for protons and at $\sqrt{s} = 5.5$ TeV per nucleon pair for ions. Since the ATLAS Pixel Detector is mainly designed for proton collisions, this thesis does not go into further details of ion collisions.

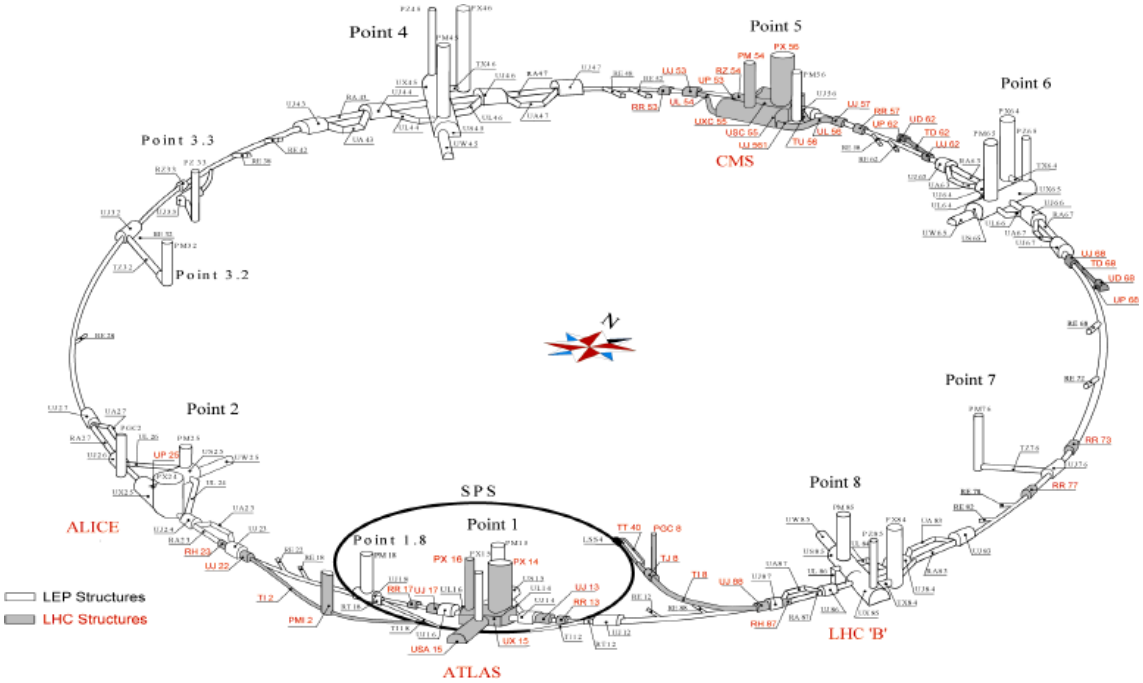

Figure 2.1: The underground structures of the LHC [B+04c].

The protons for the LHC are preaccelerated by an injector chain [B+04a] beginning with the linear accelerator Linac2. From Linac2 the protons are injected via the Proton Synchrotron Booster (PSB) and the Proton Synchrotron (PS) into the Super Proton Synchrotron (SPS). Each step of this chain increases the proton energy until it has reached 450 GeV when injected from the SPS into the LHC. There are two insertion lines feeding the particles into the LHC, one for each direction of circulation. To bend the protons on counter-circulating tracks the LHC employs mechanical structures with twin bore dipole magnets. The magnets are superconducting and deliver a peak magnetic dipole field of 8.3 T, which is necessary to keep protons at the design energy of 7 TeV in their orbit. To obtain the required field strength the magnets have to be operated at 1.9 K. The acceleration of protons within the LHC from 450 GeV to 7 TeV is accomplished by Radio Frequency (RF) cavities [BL99] working at a frequency of 400 MHz and thus generating RF buckets with a period of 2.5 ns. These cavities, located at Point 4 (see fig. 2.1), are also superconducting and have to be operated at 4.5 K. The beams are focused by superconducting quadrupole magnets. Within one bunch train, at design luminosity every tenth RF bucket is filled with a proton bunch leading to bunches every 25 ns. Along one orbit there are several bunch trains separated by empty beam gaps, which are given by the rise times of the injection kicker magnets and the beam dump kickers (see fig. 2.2). The lengths of these gaps differ between 200 ns and 3 μs. In total, one orbit is filled with 2808 bunches consisting of 1.5×10^{11} protons each. When working below design luminosity, not all bunches are filled and the number of protons per bunch is smaller.

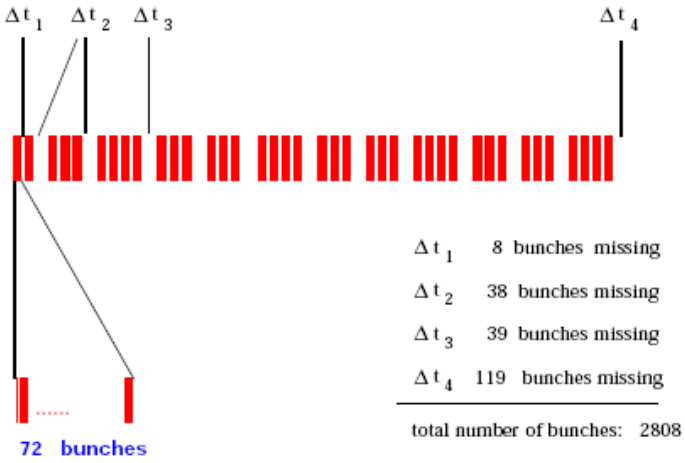

Figure 2.2: The nominal bunch filling scheme of the LHC [A+07c].

The two counter-circulating beams are brought to collision at four points of the LHC. At each collision point a particle detector is located: ATLAS, CMS, ALICE, LHCb, LHCf and TOTEM. Two of them, ATLAS (A Toroidal LHC Apparatus) and CMS (Compact Muon Solenoid), are general purpose detectors designed to allow measurements in a wide range of physics (see chapter 3). The ALICE detector (A Large Ion Collider Experiment) is optimised to study heavy ion collisions. Finally, the LHCb (Large Hadron Collider beauty) detector is optimised for b-physics. Two smaller detectors, LHCf (Large Hadron

Collider forward) and TOTEM (Total Cross Section, Elastic Scattering and Diffraction Dissociation at the LHC) share their interaction points with ATLAS and CMS, respectively. The design luminosity for ATLAS and CMS will reach $\mathscr{L} = 1.0 \times 10^{34}\text{cm}^{-2}\text{s}^{-1}$, whereas it will be $\mathscr{L} = 3.6 \times 10^{30}\text{cm}^{-2}\text{s}^{-1}$ for ALICE and LHCb.

The LHC is innovative, both in its characteristics and in its technology. The centre of mass energy at the LHC for collisions is more than seven times higher than that of the Tevatron [McG05] at Fermilab, being $\sqrt{s} = 1.96$ TeV. Until the start of the LHC, the Tevatron has been the accelerator reaching the world's highest energy. At the Tevatron protons collide with antiprotons, which is the main conceptual difference. Due to the limited production rate of antiprotons, the luminosity is limited. The choice of collisions between equally charged particles at the LHC made the design much more complex, for instance by demanding different magnetic fields in separate beam pipes. The peak luminosity of the LHC is increased by two orders of magnitude.

2.2 ATLAS Detector

The ATLAS detector [ATL08] is one of the two general purpose detectors at the LHC. It is located in a cavern in the LHC ring at point 1 (see fig. 2.1). The detector has a diameter of 25 m and an overall length of 44 m. It is larger than the CMS detector, although its weight of 7000 tonnes is less than that of CMS. A cut-away view of ATLAS is shown in fig 2.3. The detector is designed to meet the experimental challenges of the LHC, especially the unprecedented particle energy and the high interaction rate. The large acceptance in pseudorapidity η (defined as $\eta = \ln \tan \frac{\theta}{2}$, where θ denotes the angle of the particle track with respect to the proton beam axis) and the widely hermetic design assure a high particle detection efficiency.

The ATLAS detector consists of sub-detectors placed concentrically around the interaction point. These sub-detectors will be described in the following sections. ATLAS has two superconducting magnet systems to bend the tracks of charged particles, allowing for measurements of their momenta. A central solenoid provides a magnetic field of 2 T in the axial direction for the Inner Detector (ID). To minimise the material thickness in front of the calorimeter system, it is housed in the same vacuum vessel as the barrel liquid argon calorimeter. The muon detectors are supplied with a magnetic field produced by a barrel toroid and two end-cap toroids. In the central region the tangential magnetic field is 0.5 T, while it reaches 1 T in the end-cap regions. Multiple scattering is minimised by the usage of air-core loops for the barrel toroid.

2.2.1 Inner Detector

The ID [ATL97a, ATL97b] is located directly around the beam pipe and centred at the interaction point. It extends to a radius of 1.15 m. An overview is shown in fig. 2.4. Its main purposes are momentum measurements, pattern recognition and the identification of primary and secondary vertices for charged particles. The ID is designed to perform tracking for charged particles in the region $|\eta| < 2.5$. At design luminosity, each bunch crossing generates approximately 1000 particles in this region, resulting in a high track density inside the ID volume. Therefore, besides the required radiation hardness, a fine

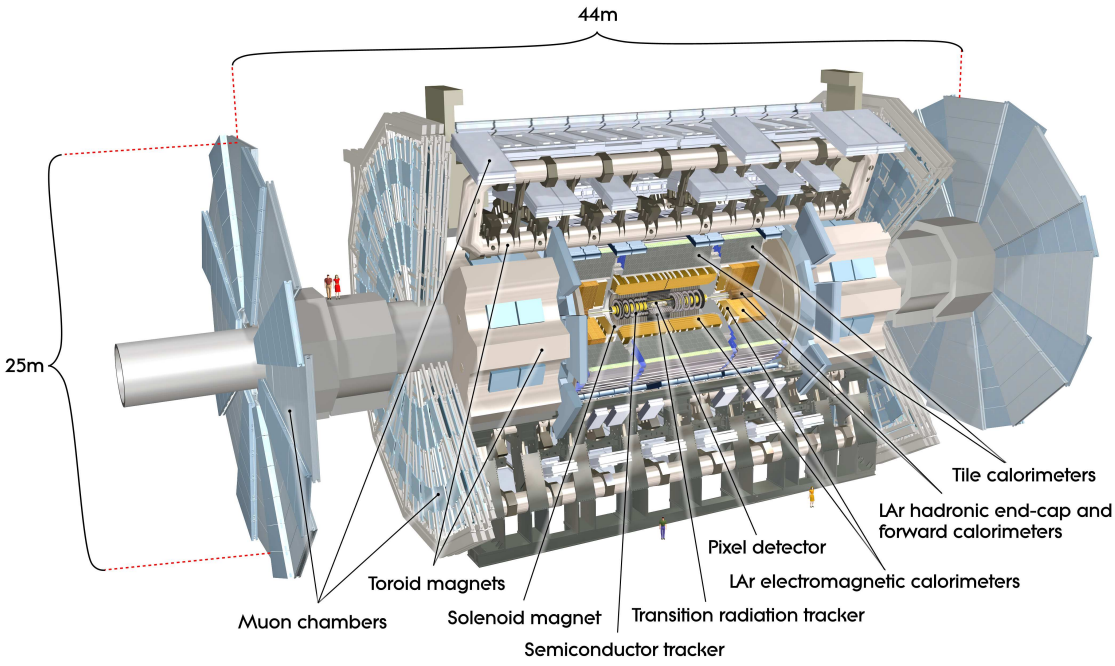

Figure 2.3: Layout of the ATLAS detector [ATL08].

granularity is important. The ID is divided into three sub-detectors (outwards from the interaction point): The Pixel Detector, the Semiconductor Tracker (SCT) and the Transition Radiation Tracker (TRT). The Pixel Detector is described in detail in chapter 5, the others are explained in the following.

The SCT [ATL97b, A$^+$07b] contributes to the tracking in the intermediate radial region. It has four barrel layers and nine end-cap discs per side, providing at least four measurement points per track. The sensors consist of 285 ± 15 μm thick silicon microstrip devices with single sided p-in-n technology. In the barrel region the detector utilises 2112 modules, each consisting of 4 sensors. On each side of the module two sensors are daisy-chained. The sensor pairs for both sides are glued back-to-back with a stereo angle of 40 mrad. This rotation allows two-dimensional tracking information to be obtained. The occurrence of so-called ghost hits in events with a high multiplicity is minimised by the use of small stereo angles rather than, for example, an orthogonal design. The problem of ghost hits is for example explained in [Dob07]. One sensor has 768 readout strips with a constant pitch of 80 μm and length of 6.4 cm. The modules in the end-cap region have tapered strips with a mean pitch of 80 μm, the number of strips, the stereo angle and their lengths being the same as for the barrel modules. In the end-cap region the 1976 modules are mounted in several rings on discs (inner, middle and outer rings). Due to the geometry for each disc, each of these types requires different layouts of the sensors. The modules for the inner ring consist of only one sensor per side while the other ones consist of two sensors per side. In total, the SCT utilises 4088 modules, each of which has 1536 readout channels. For the readout each module houses 12 identical 128-channel ASIC's, each channel containing a pre-amplifier, a shaper and a tunable threshold discriminator.

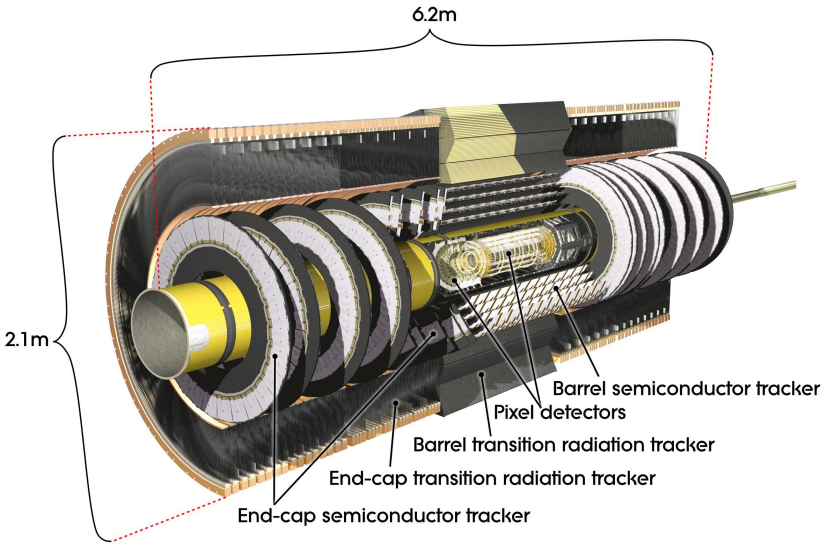

Figure 2.4: Layout of the Inner Detector of ATLAS [ATL08].

During testbeam measurements a spatial resolution of 16 μm in R-ϕ direction (concentric plane around the beam axis) and of 580 μm in z direction (along the beam axis) was obtained [Jac05].

The TRT [ATL97b, A$^+$08b] is the outermost sub-detector of the ID, providing tracking information at large radii in the pseudorapidity range $|\eta| < 2.0$. Charged particle tracks with transverse momenta of $p_T > 0.5$ GeV will give an average of 36 spacepoint measurements. Gaseous straw tubes, working as drift chambers, and transition radiation material are utilised. The polyimide straw tubes have a diameter of 4 mm and are filled with a gas mixture consisting of 70% Xe, 27% CO_2 and 3% O_2. The anodes inside the tubes consist of axial 31 μm diameter gold plated tungsten wires. Under normal working conditions, the maximum electron collection time is 48 ns, with a drift-time accuracy of 130 μm. The TRT is divided into a barrel section and one end-cap per side. In the barrel part the straw tubes have a length of 144 cm while it is 37 cm in the end-cap region. In total, the TRT has approximately 300,000 cylindrical drift tubes. The straw tubes are interleaved with transition radiation material, comprising polypropylene fibres in the barrel region and polypropylene foil in the end-cap region. Due to its mirror charge, a relativistic charged particle travelling through a medium can be considered as an electric dipole. In regions with a non-uniform dielectric constant the electric dipole field is hence time-dependent and thus transition radiation is emitted. These photons are also detected in the straw tubes, with a much larger signal compared to the signal generated by traversing charged particles. Applying two thresholds for the readout, one for a signal of traversing charged particles (threshold $\approx 250-300$ eV) and one for photons from transition radiation (threshold ≈ 7 keV), it is possible to distinguish these two particle types. Since particles with a higher Lorentz factor create more photons by transition radiation, it is possible to identify electrons, which are the lightest charged particles and have the highest Lorentz factor for a given energy.

2.2.2 Calorimeter System

The calorimeter system [ATL96a, ATL96b, ATL96c] of the ATLAS detector measures particle energies. A cut-away view of the calorimeter system is shown in fig. 2.5. In general, there are two different calorimeters: the electromagnetic (EM) calorimeter to measure energy from electromagnetically interacting particles and the hadronic calorimeter for all particles, that are not absorbed in the EM calorimeter – mainly those, that are subject to the strong interaction. Both parts utilise sampling technology: passive high density material, which creates particle cascades, alternates with active detector material.

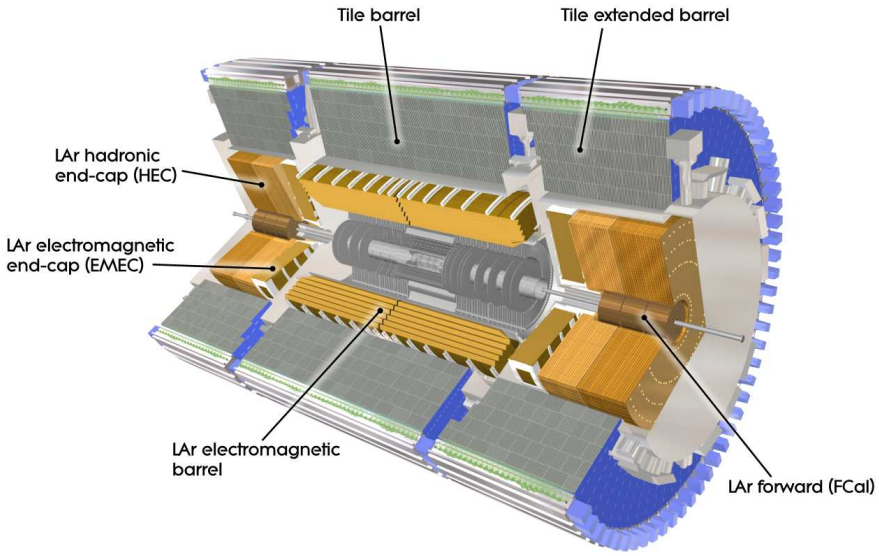

Figure 2.5: Layout of the calorimeter system of ATLAS [ATL08]. It has a length of 12.2 m and a diameter of 8.4 m.

The EM calorimeter consists of a barrel and two end-caps. Lead is used as the energy absorbing passive material and Liquid Argon (LAr) as the active sampling material. During testbeam measurements with electron beams an energy resolution of $\sigma(E)/E = 11.4\%/\sqrt{E/\mathrm{GeV}} \oplus 0.7\%$ has been obtained [A$^+$07a].

The hadronic calorimeter is composed of three parts: the Tile Calorimeter (TileCal), the LAr Hadronic End-Cap Calorimeter (HEC) and the LAr Forward Calorimeter (FCal). The TileCal, which is placed directly outside the EM calorimeter, utilises steel as the absorber material and scintillating tiles as the active material. It is the main part of the hadronic calorimeter and is subdivided into a barrel part and one extended barrel part per side. Testbeam measurements with pions showed an energy resolution of $\sigma(E)/E = 52\%/\sqrt{E/\mathrm{GeV}} \oplus 5\%$ [G$^+$05]. The HEC is located behind the end-cap parts of the EM calorimeter. As for the EM calorimeter, the HEC is a LAr detector, but it uses parallel plates of copper as the passive material. In testbeam measurements an energy resolution of $\sigma(E)/E = 70.6\%/\sqrt{E/\mathrm{GeV}} \oplus 5.8\%$ has been reached for pions [D$^+$01]. The FCal, integrated into the end-cap cryostat, covers the far-forward direction ($3.1 < |\eta| < 4.9$). It is

also a LAr detector with passive material being copper and tungsten. For pions, the energy resolution obtained in testbeam measurements was $\sigma(E)/E = 94.2\%/\sqrt{E/\mathrm{GeV}} \oplus 7.5\%$ [A$^+$08c].

2.2.3 Muon Spectrometer

The muon spectrometer [ATL97c], illustrated in fig. 2.6, is a crucial part of the ATLAS detector, since muons are a key element for many interesting physics signatures. Being located outside the calorimeters, the muon spectrometer detects mainly muons as only very few other particles pass through the calorimeters. By not measuring the muons in an event, the total particle energy of an event could be measured less efficiently and thus the estimation of so-called missing energy would be less precise. The purpose of the muon spectrometer is twofold: providing tracking information on muons and serving as a trigger source. The muon spectrometer uses four different technologies.

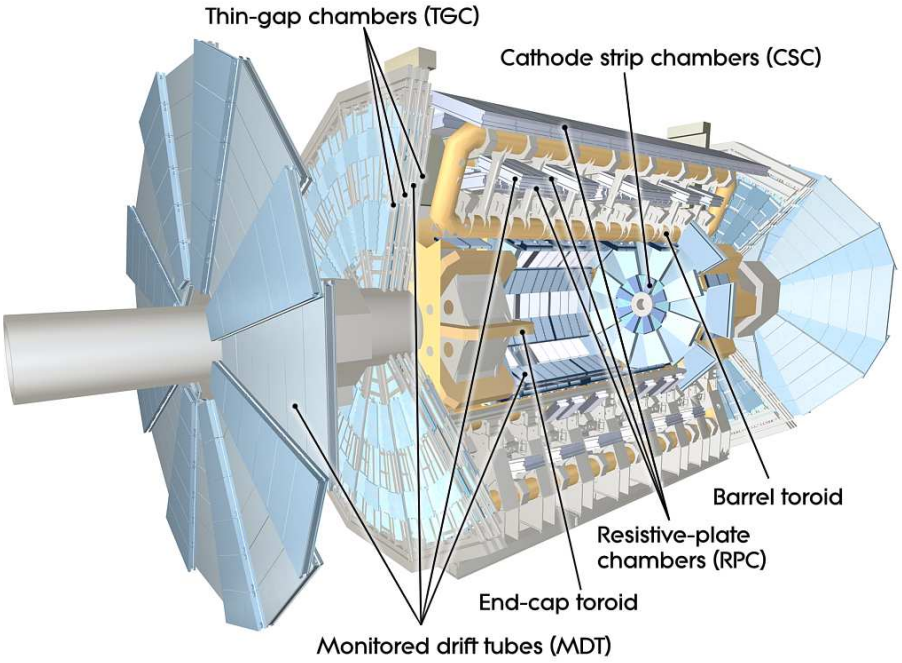

Figure 2.6: Layout of the ATLAS muon system [ATL08]. The overall length is 44 m, the diameter is 25 m.

Tracking information is obtained by Cathode Strip Chambers (CSC's) and Monitored Drift Tubes (MDT's). The barrel toroid and the end-cap toroid provide a magnetic field to bend the particle tracks and thus to enable measurements of the particle momenta. CSC's are multi-wire proportional chambers located in the innermost plane of the high radiation forward region ($2.0 < |\eta| < 2.7$). The design is driven by the high rate and background conditions in this region. MDT's, where the term "monitored" indicates that the position and deformations of the MDT chamber geometry are measured by an optical system, are drift tubes with an aluminium casing. These detectors are mounted both in the barrel section and in the end-cap section, constituting the largest part of the muon

tracking system. MDT's cover the region $|\eta| < 2.7$.

Signals for the trigger system in the region $|\eta| < 2.0$ are provided by Resistive Plate Chambers (RPC's) and Thin Gap Chambers (TGC's). Besides identification of the correct bunch crossing with a resolution of better than 25 ns, the muon trigger system has to provide well-defined transverse momentum (p_T) thresholds and measurements of the muon coordinate in the direction orthogonal to that determined by the tracking chambers. The RPC's, which are narrow gas chambers, give fast trigger signals in the barrel region ($|\eta| < 1.05$) while TGC's, multi-wire proportional chambers, provide fast trigger signals in the end-cap region ($1.05 < |\eta| < 2.4$).

2.2.4 Trigger and Data Acquisition System

The bunch crossing rate at the LHC is 40 MHz, with about 23 collisions per bunch crossing at the design luminosity of $10^{34}\text{cm}^{-2}s^{-1}$, leading to an interaction rate of approximately 10^9 Hz. Due to bandwidth limitations, an effective trigger is required, which selects only events with interesting physics and rejects the other ones as much as possible. ATLAS utilises a three level trigger system [ATL98a, ATL03, Hau04] (see fig. 2.7): The hardware based level one (LVL1) trigger, the software based level two (LVL2) trigger and the software based Event Filter (EF). LVL2 and EF are referred to as the High Level Trigger (HLT).

The LVL1 trigger reduces the event rate to less than 75 kHz (upgradable to 100 kHz). It is implemented in custom hardware and designed to reach a fast decision on whether an event should be read out. However, a decision can not be reached within the 25 ns between two bunch crossings, which necessitates that each sub-detector stores its events in pipeline memories until receipt of the LVL1 signal. The LVL1 signal has to arrive in less than 2.5 μs at the sub-detectors. When an event is selected, the data of all sub-detectors are transferred to their Readout Drivers (ROD). Since the input bandwidth of the ROD's may be exceeded by the instantanous high rate, derandomisers are used to average out high input data rate peaks. From the ROD's the data are sent to the Readout Buffers (ROB), where they are accessible to the LVL2 trigger. The LVL1 trigger uses information from the muon detectors and the calorimeters. Decisions are made by the Central Trigger Processor (CTP) and are based on various thresholds on transverse momentum of muons and energies deposited in the calorimeters. Via the Timing, Trigger and Control (TTC) system, the LVL1 signals are transmitted to the sub-detectors.

The online software based LVL2 trigger receives information on Regions of Interest (RoI's) and other trigger objects from the LVL1 trigger. RoI's are small regions in pseudorapidity-azimuth space ($\eta-\phi$) located around an object with interesting features found by the LVL1 trigger. Information on trigger candidates contain their positions, transverse momenta and energy sums. To make a further trigger decision, the LVL2 trigger could access the full event data stored in the ROB's, but due to the RoI mechanism it usually only requests about 2% of it. The candidate event is compared to various criteria and discarded if some of them are not met. In this way the rate of accepted events is reduced to below 3.5 kHz. Finally, data from accepted events are passed to the event builder. The average latency for a LVL2 decision on a certain event is about 40 ms.

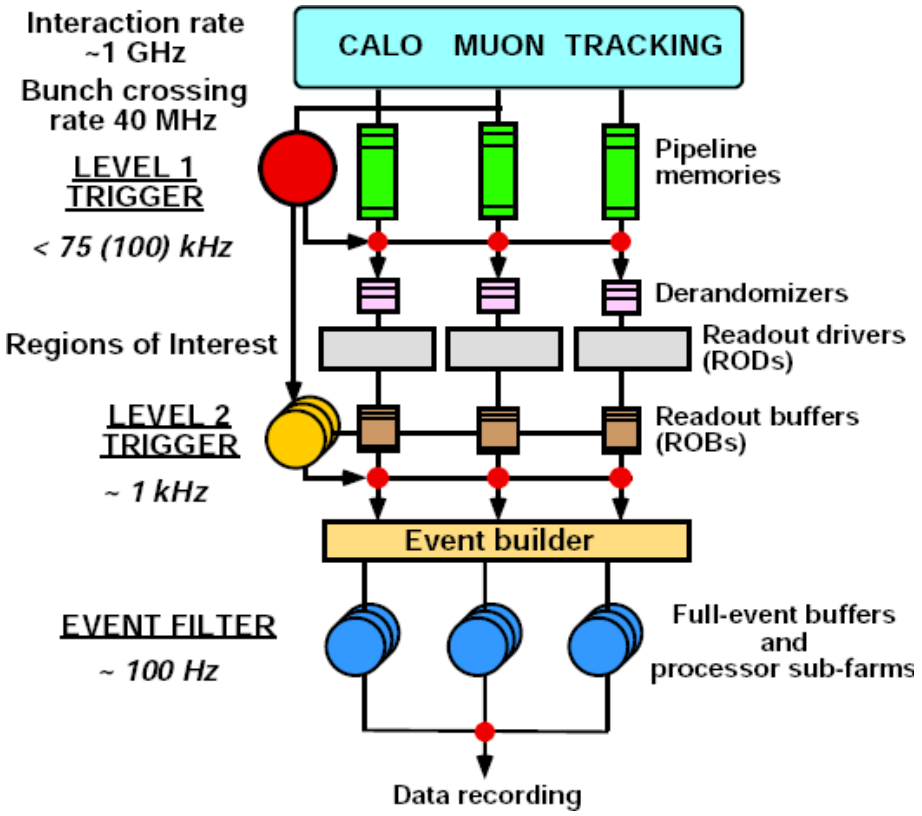

Figure 2.7: Principle of the ATLAS trigger system [ATL98c]. See the text for explanations.

The last step is the EF, working on the full event information delivered by the event builder. It functions similarly to the LVL2 trigger, but uses offline algorithms with full access to up-to-date calibration and alignment databases. Here, tighter thresholds can be applied and time-consuming algorithms, with e.g. vertex and track finding, can be executed. The output rate of accepted events is approximately 200 Hz and the average event processing time in the EF is about 4 s. Accepted events are sent to a sub farm output node and then transmitted to mass storage.

Chapter 3

Physics at the LHC

The LHC is designed to be a discovery machine. With its unprecedented centre of mass energy of $\sqrt{s} = 14$ TeV it is possible to investigate elementary particle physics up to the TeV-scale. In the coming years, measurements on physics described by the Standard Model (SM) of particle physics as well as searches for physics beyond the SM, such as supersymmetry or extra dimensions, will be performed. One of the most important projects is the search for the Higgs boson, which is expected to exist within the framework of the SM. In this chapter, the SM (see e.g. [PS95]) will be introduced and some aspects of the searches for the Higgs boson at the LHC will be described. All discussions assume the commonly used convention $\hbar = c = 1$.

3.1 Standard Model

	charge	1^{st} generation	2^{nd} generation	3^{rd} generation
Leptons	$-e$	electron (e) [0.511 MeV]	muon (μ) [105.7 MeV]	tau (τ) [1.777 GeV]
	0	electron neutrino (ν_e) [< 2 eV]	muon neutrino (ν_μ) [< 2 eV]	tau neutrino (ν_τ) [< 2 eV]
Quarks	$+2/3\ e$	up [$1.5 - 3.0$ MeV]	charm [1.25 GeV]	top [174.2 GeV]
	$-1/3\ e$	down [$3 - 7$ MeV]	strange [95 MeV]	bottom [4.2 GeV]

Table 3.1: The elementary fermions as described by the SM. Numbers in brackets specify mean values or upper limits of the particle masses. The masses of the up, down and strange quarks are "current-quark masses" in the $\overline{\text{MS}}$ scheme. For bottom and charm quarks, the masses are "running masses" in the $\overline{\text{MS}}$ scheme. The top mass is calculated using data from Tevatron Run-I and Run-II [Y+06].

	Electromagnetic Interaction	Weak Interaction		Strong Interaction
Gauge Bosons	Photon (γ) [$< 6 \times 10^{-14}$ eV]	$W^{\pm}$ [80.403 GeV]	Z^0 [91.1876 GeV]	8 gluons (g) [0 eV]

Table 3.2: Gauge bosons of the three interactions described by the SM. Numbers in brackets specify mean values or upper limits of the particle masses. The cited mass of the gluons is the theoretical value [Y+06].

The SM is a successful theory describing the existence of and the interactions between elementary particles. Tables 3.1 and 3.2 summarise the particles described by the SM: 12 fermions (spin $S = 1/2$, quarks and leptons) and 12 gauge bosons (integral spin). Additionally, each fermion has its own antiparticle, which is oppositely charged. The fermions are grouped into generations, each containing two quarks (one with $q = 2/3\ e$, one with $q = -1/3\ e$), one negatively charged lepton ($q = -e$) and one neutral lepton (neutrino), where e is the elementary charge. Neutrinos are described as massless within the SM, whereas they have been found to have an, albeit minuscule, nonzero mass [F+98]. Only upper limits for the masses are known. The arrangement in generations is primarily motivated by the mass scale: Particles in the first generation have the lowest mass, particles in the third generation have the highest mass. Since particles can decay to lighter ones (respecting several conservation laws), all stable matter is composed of electrons, up quarks and down quarks. Neutrinos are produced as elusive decay products and are found to oscillate between different types [F+98]. The unstable particles can be observed in experiments at particle accelerators or with air showers induced by cosmic rays.

The theory of the SM contains the formulation of three interactions between elementary particles:

- All particles, which carry electric charge, are subject to the electromagnetic interaction. It is transmitted by the massless and neutral photon, denoted as γ.
- Fermions interact via the weak interaction. It has three exchange particles: The W^+, the W^- (having charge $+e$ and $-e$ respectively) and the neutral Z^0.
- Quarks are subject to the strong interaction. Each quark carries one of three colours, antiquarks carry anticolour. The strong interaction is mediated by eight gluons, carrying combinations of colour and anticolour.

Furthermore, all massive particles are affected by gravity. This interaction is not described by the SM, however it can be neglected in elementary particle physics processes. The lack of inclusion of gravity is one of the most remarkable shortcomings of the SM. The electromagnetic and weak interactions are unified within the SM to the electroweak interaction, which is described by an $SU(2) \times U(1)$ gauge group. The strong interaction requires a formulation under the SU(3) gauge group. Thus, the Lagrangian of the SM has an $SU(3) \times SU(2) \times U(1)$ symmetry [Gla80].

However, the properties following from these symmetries do not explain the generation of elementary particles' masses. A solution has been introduced by assuming a scalar field

permeating the vacuum [Hig66]. In this so-called Higgs mechanism, named after one of its inventers Peter Higgs, the ground state of the vacuum acquires a non-zero expectation value. The original symmetry is spontaneously broken. A theoretical treatment shows that elementary particles can acquire their mass through interactions with the scalar Higgs field. As a further implication, this mechanism would lead to a massive scalar particle, the Higgs boson. This is the only particle described by the SM which is not yet discovered.

3.2 Higgs Searches at the LHC

The discovery of the massive scalar Higgs boson, H^0, is one important topic of research at the LHC and would complete the understanding of the electroweak symmetry breaking mechanism. The properties of the Higgs boson, such as the mass, decay width and branching ratios, are associated to free parameters within the SM and are not yet known. However, a lower limit on the Higgs mass was set by direct searches at LEP-2 at 114 GeV [Fer03]. Several production channels for the Higgs boson are considered at the LHC, the most important ones are gluon fusion via a top quark loop and vector boson fusion [Col08], see Fig. 3.1.

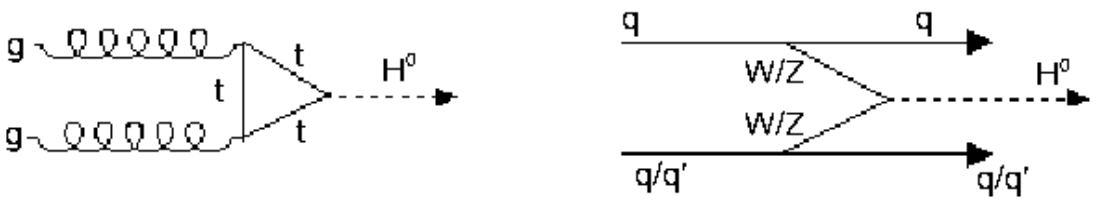

Figure 3.1: The highest rate production channels for the Higgs boson at the LHC: gluon fusion (left) and vector boson fusion (right).

The coupling of the Higgs to gauge bosons is proportional to the square of the gauge boson's mass and for fermions directly proportional to the fermion's mass. Hence the Higgs decays preferably to the heaviest particle that is kinematicelly allowed. The calculated branching ratios of the Higgs boson for the different decay channels are illustrated in Fig. 3.2.

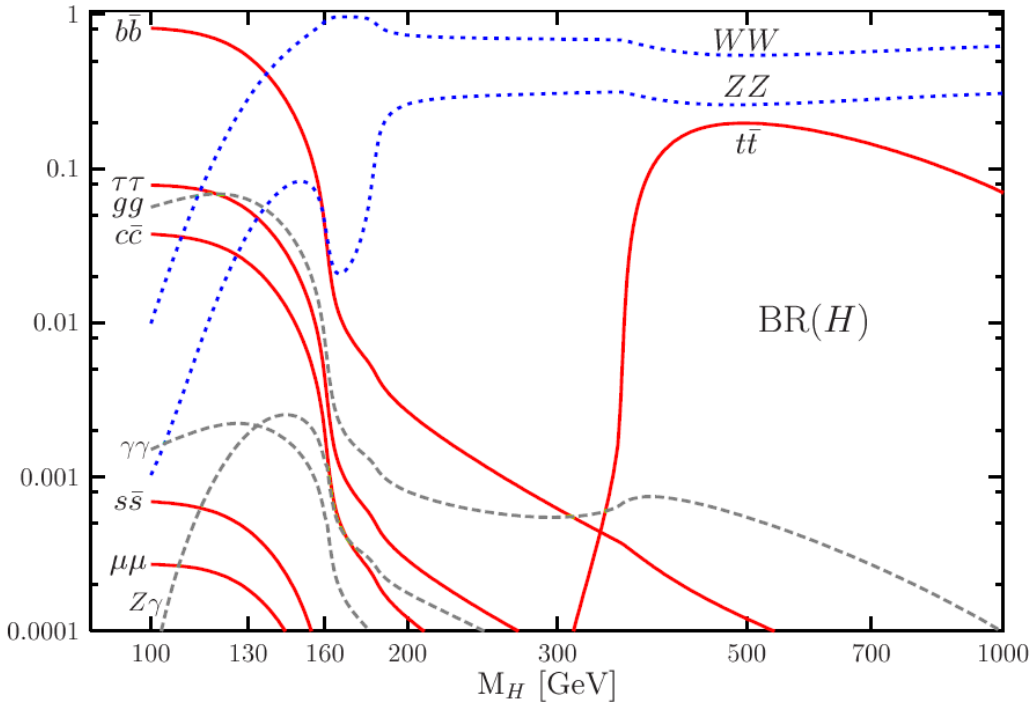

Figure 3.2: The calculated branching ratios of the SM Higgs boson as a function of the Higgs mass M_H [Djo05].

Due to the lack of knowledge of the Higgs mass, the LHC detectors have to prepare for a wide range of the possible decay channels and hence possible signatures. Therefore, each subdetector may give important contributions to this physics programme. For example, the ATLAS Pixel Detector is essential for b-tagging, which is an important task to detect the Higgs boson. It is crucial to tag decays containing b-jets, as in the decay mode $H^0 \rightarrow b\bar{b}$, which is the dominating decay channel for a low-mass Higgs boson. Furthermore, the Pixel Detector plays an important role to identify jets originating from top quarks, which decay preferably to bottom quarks. The identification of top-jets is required for background discrimination and for detection of the Higgs boson in the decay channel $H^0 \rightarrow t\bar{t}$.

Chapter 4

Semiconductor Detectors

Semiconductor detectors are widely used in high energy physics, mainly to measure the trajectories of charged particles after particle collisions. In recent decades, they have become the leading devices for tracking detectors, due to several advantages over other techniques such as wire chambers. The main advantage is the small spatial resolution in conjunction with a high readout speed. However, semiconductor detectors also have some drawbacks, for instance the high price and the need for sophisticated cooling techniques. This Chapter introduces some basic principles and outlines the functionality of semiconductor detectors. The Chapter focuses on silicon, since this material is used for almost all semiconductor detectors in high-energy physics.

4.1 Energy Transfer of Particles in Semiconductors

Charged particles traversing a material transfer a fraction of their energy to the material. The type of interaction depends on the kind of particle and the particle's energy. Charged heavy particles (other than electrons), which are moderately relativistic, lose their energy mainly by ionisation and excitation of atoms. The energy loss per traversed material length is described by the Bethe-Bloch formula, which can be found for instance in [Y+06]. Figure 4.1 illustrates the mean energy loss in different materials as calculated using the Bethe-Bloch formula. Particles, which have an energy around the minimum of the curve, are referred to as Minimum Ionising Particles (MIP's).

Electrons and positrons show a different energy loss behaviour. The predominant mechanism of energy loss of high energetic electrons (above approximately 10 MeV) is bremsstrahlung. However, electrons and positrons also lose part of their energy by ionisation and excitation, which prevails at low energies [Y+06].

Since energy loss is a statistical process, it is subject to fluctuations around the mean value as given, for example, by the Bethe-Bloch formula. These fluctuations follow approximately a Landau distribution and become Gaussian-like for thick materials. Figure 4.2 shows the energy loss probability distribution for 500 MeV pions in silicon for different thicknesses. The dependency of the skewness on the sensor thickness can be seen. For silicon, the most probable value of the energy deposited by a MIP in a layer of thickness

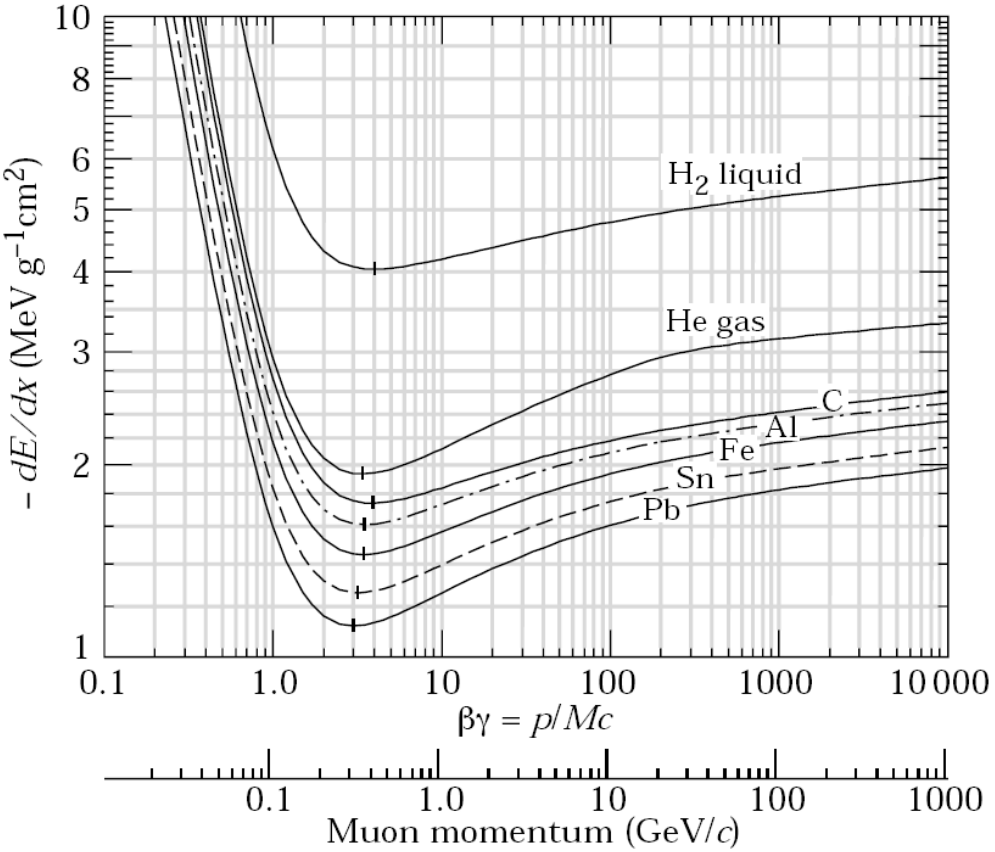

Figure 4.1: Mean energy loss rate $\mathrm{d}E/\mathrm{d}x$ for different materials. Radiative effects, which become important above 100 GeV for muons, are neglected [Y$^+$06].

t (in μm) is [Bic88]

$$E_{mp}[\mathrm{keV}] = t(0.1791 + 0.01782 \ln(t)). \tag{4.1}$$

For e.g. $t = 256$ μm, the thickness the ATLAS Pixel Detector sensor, $E_{mp} \approx 71$ keV is obtained.

The energy transfered to the semiconductor material is used to generate electron-hole pairs. Electrons are excited from the valence band to the conduction band and a free hole arises in the valence band. The average energy required for the generation of an electron-hole pair is 3.62 eV in silicon, whereas the band gap between valence band and conduction band is only 1.1 eV (both at 300 K [Leo94]). The excess energy excites lattice vibrations in the silicon. Given the deposited most probable energy of $E_{mp} = 71$ keV in a layer of $t = 256$ μm, approximately $71000/3.62 \approx 20000$ electron-hole pairs are generated. Compared to gas detectors, the average energy transfer is an order of magnitude lower. As a consequence, the number of free charge carriers is higher and the energy resolution in semiconductor detectors is increased, even though energy measurement is usually not the primary task for semiconductor detectors used in high-energy physics.

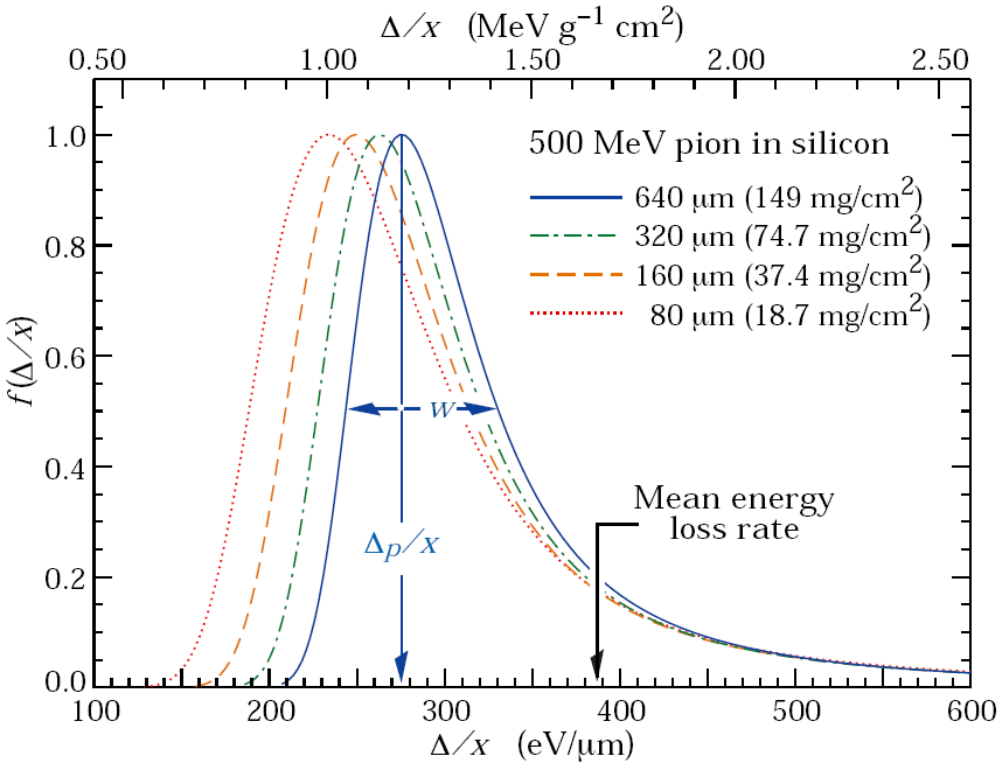

Figure 4.2: Distribution of the energy loss probability of 500 MeV pions in silicon layers with different thicknesses [Y+06].

In principle, it is also possible to detect photons with semiconductor detectors, but the detection probability for high energetic photons (as present after collisions at the LHC) is low. When passing a material of the thickness d, the intensity $I(d)$ of a photon beam with the initial intensity I_0 decreases according to

$$I(d) = I_0 e^{-\rho d/\lambda}, \tag{4.2}$$

where ρ is the density of the traversed matter and λ is the photon mass attenuation length. Figure 4.3 displays the photon mass attenuation length for different materials. For high energetic photons passing through silicon, λ is about 30 g/cm^2. Assuming an active layer of $d = 250$ μm in a silicon detector with density $\rho = 2.33$ g/cm^3 [Y+06], $I/I_0 = 99.8\%$ is obtained. That means, only 0.2% of high energetic photons undergo an interaction in the silicon sensor, which is negligible.

The neutron is not subject to the electromagnetic interaction. Its main interaction happens via the strong force with nuclei. For this interaction, the neutron has to approach the nucleus within $\approx 10^{-15}$ m, which is not very likely, since the distance between nuclei in a material is large. Thus, neutrons are very penetrating and their energy transfer in semiconductor detectors can be neglected [Leo94].

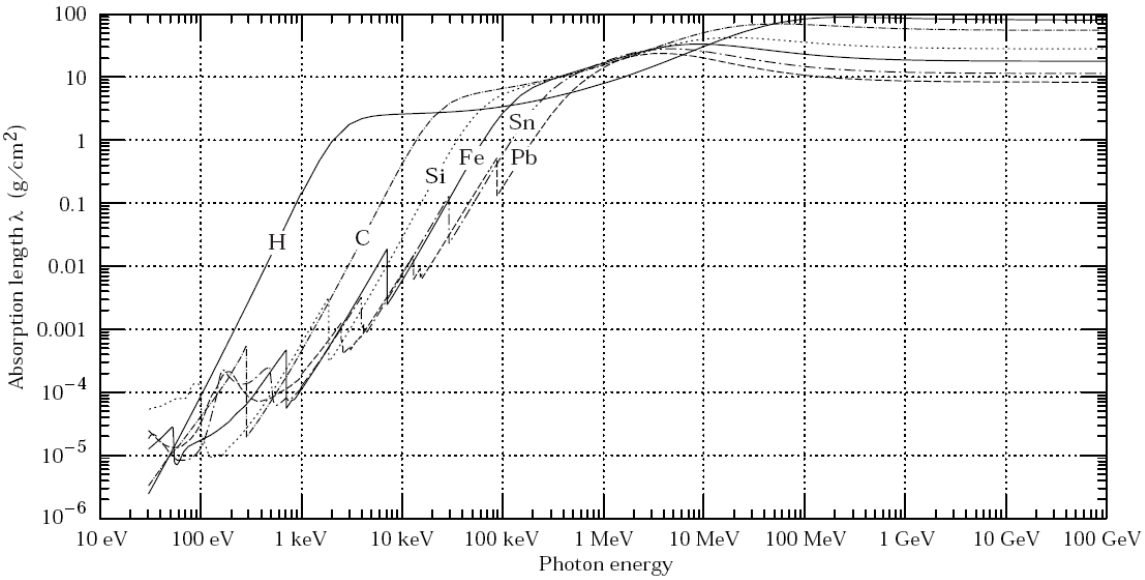

Figure 4.3: Photon mass attenuation length λ for different materials [Y+06].

4.2 Principles of Semiconductor Detectors

After the passage of a charged particle and transfer of energy to the semiconductor material, the liberated charge carriers must be collected and detected. However, in intrinsic (undoped) semiconductors, the number of free charge carriers due to thermal excitation is already high and thus electron-hole pairs generated by traversing particles are numerically negligible. To reduce the background of free charge carriers, extrinsic semiconductors are employed. An extrinsic semiconductor contains impurity atoms, which introduce energy states in the band gap and hence cause an excess of either free electrons in the conduction band (n-type) or free holes in the valence band (p-type). Regions with different doping types are brought into contact to obtain a p-n structure, as it is used in a diode. A p-n structure is operated under reverse bias to obtain a depletion zone, which should extend over the entire sensor layer. The voltage, required for full depletion of a layer of thickness d, is [Lut99]

$$V_{dep} = V_{bi} - \frac{eN_A N_D}{2\epsilon\epsilon_0(N_A + N_D)} d^2. \tag{4.3}$$

Therein, V_{bi} denotes the built-in voltage (which is normally small compared to the depletion voltage V_{dep}), N_A and N_D denote the acceptor and donator concentrations, ϵ_0 and ϵ denote the permittivity of free space and the sensor material, and e is the electron charge.

Operating the p-n structure with reverse bias results in a high resistivity of the sensor. Due to the lack of free charge carriers, the current between the electrodes is very low and increases significantly after generation of free charge carriers by traversing particles. In a semiconductor detector, this current is integrated and the resulting charge is usually amplified and then read out.

Figure 4.4 illustrates the principle design of a semiconductor detector. The p-n junction

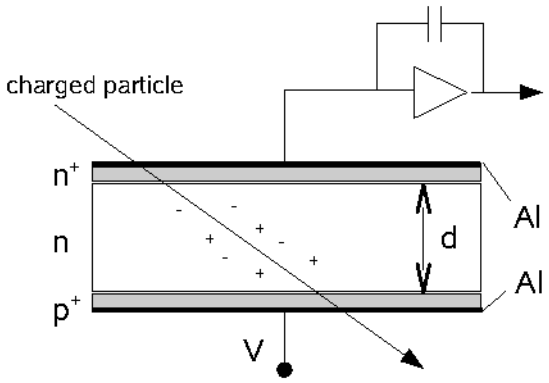

Figure 4.4: Principle of a semiconductor detector with n-type bulk. The bottom electrode is held on negative potential, whereas the top electrode is kept on ground potential. Thus, liberated holes are drawn to the bottom and liberated electrons are drawn to the top.

is present around the interface between the highly doped shallow p^+-layer at the bottom and the lowly doped n-substrate. Due to the difference of the doping concentrations, the depleted zone extends widely into (or fully over) the n-substrate and only shallowly into the p^+-layer. The highly doped n^+-layer on the top side allows operation with overdepletion and assures a good Ohmic contact between the metal contact (which is typically aluminium) and the substrate [Lut99]. Semiconductor detectors as used in particle detectors for position measurements employ a more elaborate design, with e.g. one anode segmented in strips or pixels. The design used for the ATLAS Pixel Detector is explained in Chapter 5.

4.3 Radiation Damage

Semiconductor tracking detectors at the LHC operate in an extremely high radiation environment. The radiation exposure causes defects in the silicon crystal lattice and leads to deterioration of macroscopic properties of the detector [Mol99]. The basic damage mechanism occurs when an incident particle knocks an atom out of its lattice place. A point defect is generated, the unbounded atom is hence denoted as an interstitial and the free latice place is referred to as a vacancy. The interstitial and the vacancy can migrate through the lattice and, if their energies are sufficiently high, knock out further atoms from their lattice positions. At the end of their path, after they have lost most of their energies by ionisation and displacement of further atoms, the interstitials and the vacancies can cause dense conglomerations of defects, referred to as clusters. Both point defects and clusters are responsible for the change of detector properties after irradiation. After irradiation the lattice defects remain mobile - especially at high temperatures - and cause further defects. This is one reason, why cooling of semiconductor detectors at particle colliders is necessary. Finally, interstitials and vacancies may be trapped by impurities and crystal defects. They can form bonds with, for instance, the doping atoms and affect their energy levels. Hence it is e.g. possible, that initial donors do not act as donors any more or that additional dopants are created.

The microscopic damage mechanisms, as sketched above, lead to deterioration of macroscopic properties. These are mainly the change of the depletion voltage (caused by alteration of the effective doping concentration), increase of the leakage current, degradation of charge collection efficiency and surface damage.

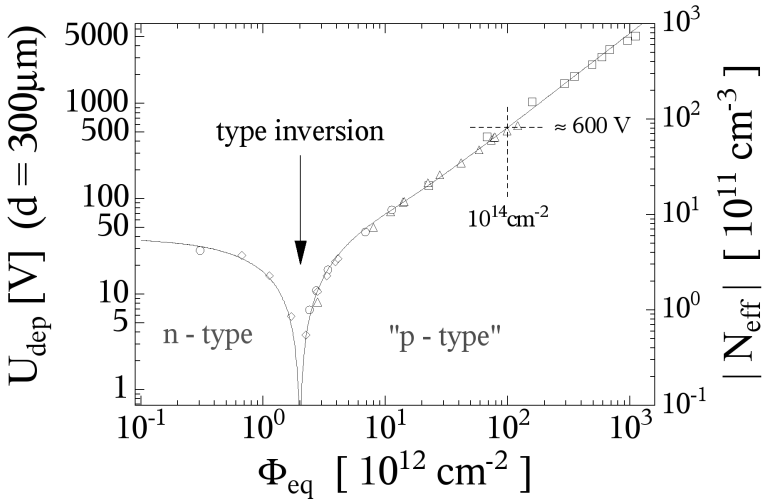

Figure 4.5: Depletion voltage V_{dep} and the absolute value of the effective doping concentration N_{eff} as a function of the received fluence, scaled down to 1 MeV neutrons [Wun92].

The change of the depletion voltage is probably the most detrimental macroscopic defect caused by radiation. As described by eq. 4.3, the depletion voltage is a function of the concentrations of acceptors and donors. Since the doping concentrations are affected by radiation induced defects, the depletion voltage changes. In n-type bulk, which is most commonly used in semiconductor detectors, this leads to donor removal and acceptor creation. With increasing radiation dose, the depletion voltage decreases and, after type inversion, it rises again. Type inversion denotes the effect, that the doping profile changes, for example from n-type to p-type. This behaviour is illustrated in Fig. 4.5. After a high radiation dose, a full depletion of the active detector layer may not be possible, which has an extremely detrimental effect on the detector performance.

The leakage current increases after irradiation, mainly due to creation-recombination centres close to the middle of the band gap, and leads to larger noise. The increase in current is proportional to the received fluence [Mol99]:

$$\Delta I = \alpha \Phi_{eq} V, \tag{4.4}$$

where α denotes the current related damage rate, Φ_{eq} denotes the received particle fluence scaled down to 1 MeV neutrons and V is the sensor volume. The leakage current decreases with decreasing temperature, so this is another reason for the cooling of the detector. The proportional dependency of the leakage current on the sensor volume is one reason for

employing in very high radiation environments pixel detectors rather than strip detectors.

The charge collection efficiency decreases with increasing radiation dose. This behaviour is caused by the generation of trapping centres in the band gap. Holes and electrons are trapped for a length of time and are lost for the signal but contribute to the noise when they are released.

The surface of a silicon sensor is mainly covered by SiO_2. Inside this layer, radiation causes an accumulation of positive charges and thus affects accumulation of negative image charge in the upper region of the sensor. This surface damage can have detrimental effects for structured silicon sensors as pixel or strip detectors.

Different techniques have been investigated to moderate the radiation damages. One of the most successful strategies is the enrichment of silicon with oxygen. Oxygen acts as a sink for radiation induced vacancies and prevents them from forming bonds with dopants. This results in a more moderate change of the effective doping concentration and the depletion voltage.

Chapter 5

The ATLAS Pixel Detector

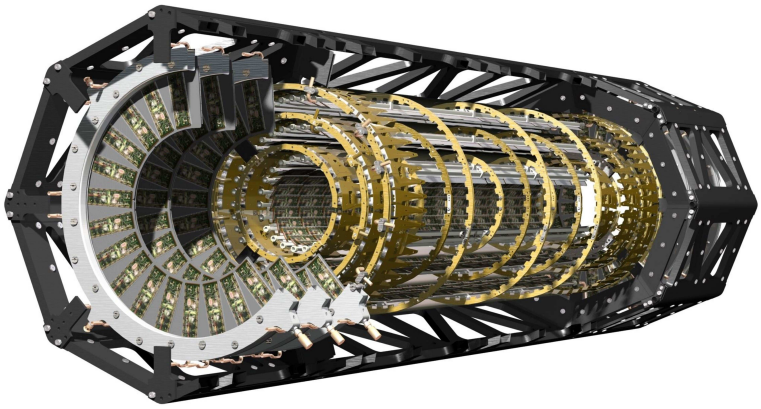

Figure 5.1: Cut-away view of the ATLAS Pixel Detector [ATL08].

The ATLAS Pixel Detector [ATL08, ATL97b, ATL98b], see Fig. 5.1, is the innermost tracking sub-detector of ATLAS. It is designed to provide three measurement points per track in the pseudorapidity region $|\eta| < 2.5$. The performance requirements are the optimisations of

- pattern recognition in high multiplicity environments,
- transverse impact parameter resolution and 3D-vertexing capability,
- b-tagging and b-triggering capabilities.

The usage of a detector with segmented pixels rather than a strip detector close to the interaction point is motivated by the high track density and the harsh radiation environment. Both the occupancy and the leakage current after irradiation – and thus the noise – would be too high in a strip detector. According to eq. 4.4, the increase of the leakage current after irradiation is proportional to the volume of the detector segments.

5.1 Overall Layout

The Pixel Detector has 1744 modules, arranged in three end-cap discs per side and three barrel layers. For a good b-tagging efficiency, the small radius inner barrel layer, referred

to as B-layer, is essential. The radius of the B-Layer is 5 cm due to limitations given by the beam pipe system. The radii of the outer layers are 9 cm and 12 cm. In the barrel, the 13 modules are arranged on 80 cm long staves with mechanical supports and cooling. The layout of each stave is identical for every layer, only the number of staves varies between 22 staves on the B-layer, 38 on layer 1 and 52 on layer 2. Each end-cap consists of three identical discs, each of which has eight sectors. A sector provides cooling and mechanical support and carries six modules. The discs are located at a distance of 50, 58 and 65 cm from the interaction point.

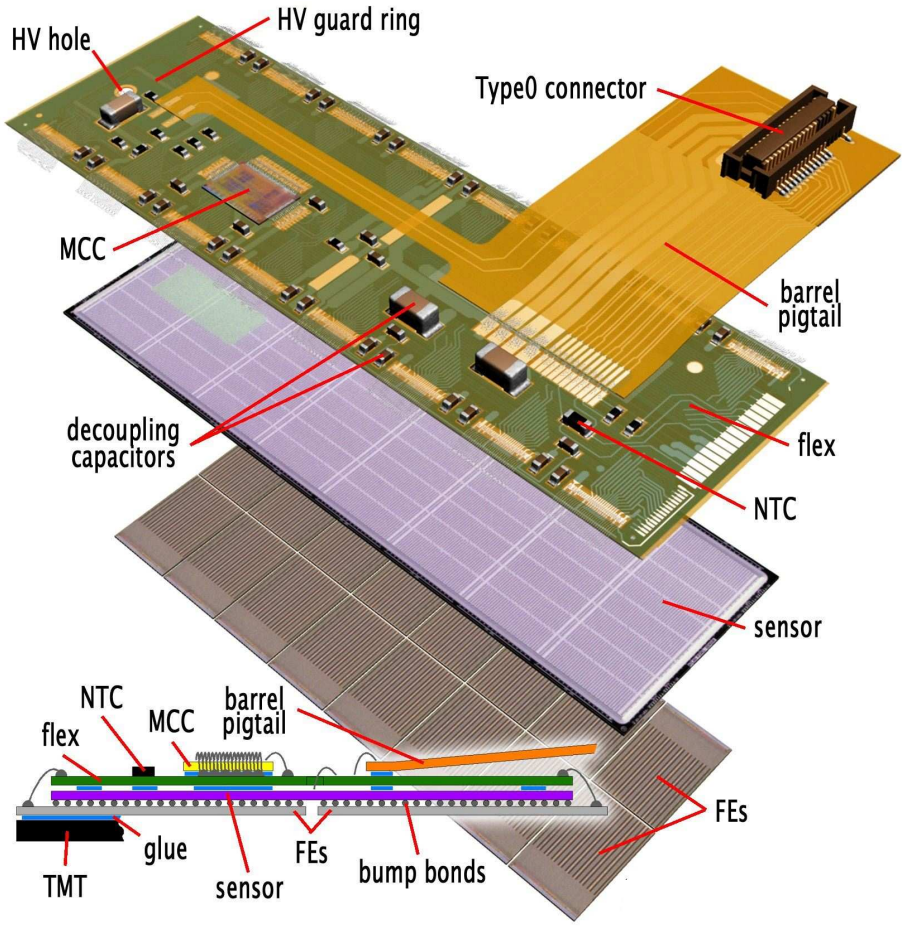

Figure 5.2: Schematic view of the different layers of an ATLAS Pixel Detector module [ATL08].

Each of the 1744 modules has an area of approximately 6×2 cm^2 and has 46080 readout channels. In total, this leads to approximately 80 million readout channels of the Pixel Detector, which is about half of the total number of ATLAS channels. The pixel size has to be as small as possible for optimal performance, but a lower limit is set by limitations of the electronic readout chips. Most of the pixels have a size of 50×400 μm^2. However, to cover the interchip regions, about 10% are longer pixels (see section 5.2 for details).

The intrinsic resolution of the pixel modules for single pixel hits can be calculated assuming a uniform probability distribution over one pixel. The standard deviation in one dimension for a hit in a pixel with pitch p is

$$\begin{aligned} \sigma &= \sqrt{< x^2 > - < x >^2} \\ &= \sqrt{\frac{1}{p}\int_0^p x^2 \, \mathrm{d}x - \left(\frac{1}{p}\int_0^p x \, \mathrm{d}x\right)^2} \\ &= \frac{p}{\sqrt{12}}. \end{aligned} \tag{5.1}$$

Thus, one obtains for the resolution of the pixel modules $\sigma = 14$ μm in R $-$ ϕ direction and $\sigma = 115$ μm in z direction. Due to charge sharing between neighbouring pixels, the resolution is improved. The magnitude of charge sharing and thus the resolution depends on the incident angle of traversing particles. This is dependent on the Lorentz angle, which changes with modified bias voltage as applied after irradiation. Detailed studies are reported in [A$^+$08a] and [G$^+$02].

A pixel module (see Fig. 5.2) consists of three layers: On top, the flex-hybrid carries the Module Controller Chip (MCC, described in section 5.4) and electronics for power and signal distribution. Below, the silicon sensor tile (see section 5.2) is located. The third layer from the top is composed of 16 Front-End (FE) chips (described in section 5.3), connected to the sensor by means of the bump-bonding technique. Wirebonds provide the connections for data and power channels between the FE chips and the flex-hybrid. The modules are glued on the Thermal Management Tile (TMT). It assures heat dissipation over the FE's and provides thermal contact between the cooling structure and the pixel module.

To minimise radiation damage (see section 4.3) and leakage current (and consequently the noise level), the pixel modules are operated at approximately -7°C. The Pixel Detector and the SCT use a joint evaporative cooling system with C_3F_8 (octafluoropropane) as coolant. Additionally, the Pixel Detector volume is flushed with dry nitrogen between -7°C and 0°C. Although this has no significant cooling effect, it avoids condensation on the cold surfaces.

5.2 The Sensor

The ATLAS Pixel Detector has a silicon sensor with n$^+$-in-n technology [H$^+$01, Wun01, A$^+$08a]. The n-type bulk has a thickness of $256 \pm 3\mu$m. A cross section of the sensor and the bump bond connection with the readout chip is shown in Fig. 5.3. The design of the pixel sensor had to meet two kinds of demands: performance requirements and module constraints on the one hand and requirements set by the high radiation environment on the other hand.

To meet the performance requirements, the pixel sensor must be highly granulated. However, the pixel size is limited by constraints given by the readout electronics, since each pixel should have its own readout cell. These constraints result in a pixel size of 50 $\times$

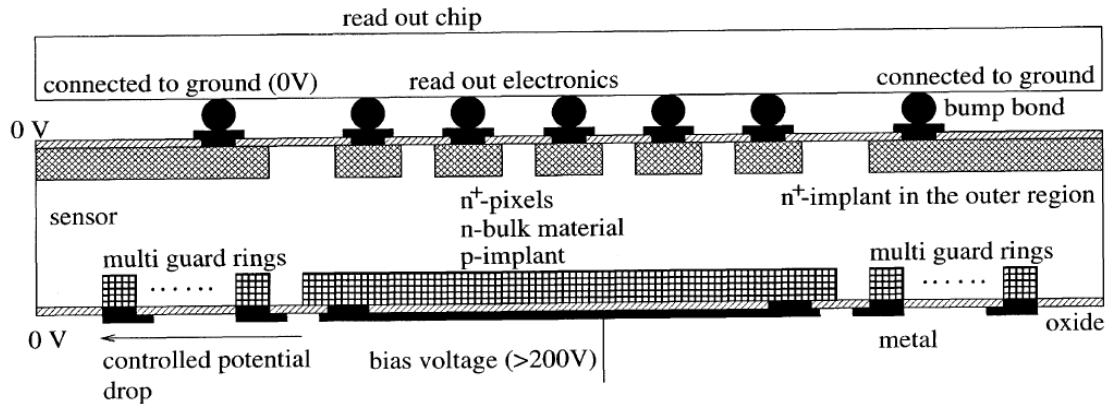

Figure 5.3: Cross section of the ATLAS Pixel Detector sensor and the connection with the readout chip [R+98].

400 μm^2 for about 90% of the pixels. Per module, 47232 pixels are arranged in 144 columns and 328 rows. To avoid a dead area between the FE chips, the pixels at the FE chip edges in the direction of the long pixel side are longer, measuring 50×600 μm^2. The dead area between the FE chips in the other direction is avoided by the use of ganged pixels. In each column, 8 pixel pairs are ganged to a common readout per pair. Thus, one module has 46080 readout channels.

The Pixel Detector has to operate in an extremely harsh radiation environment. The B-layer is expected to be exposed to a standard fluence of up to 3.5×10^{14} cm^{-2} per year, scaled down to 1 MeV neutrons [Wun01]. As illustrated in Chapter 4.3, a high radiation exposure leads to deterioration of several sensor properties. To reduce the alteration of the effective doping concentration and thus of the depletion voltage, the pixel sensors are made of diffusion oxygenated float zone silicon. The high oxygen content leads to a more moderate change of the effective doping concentration. Nevertheless, the initially n-doped bulk is expected to invert to p-type and the depletion zone will start to grow from the side where the pixels are implanted. This was the reason to apply n$^+$-in-n technology: it assures electrical isolation of the pixel implants even when full depletion of the bulk is not possible any more. The shallow n$^+$ and p$^+$ regions do not invert due to their high doping concentrations. The voltage needed for full depletion of the sensor will rise, therefore the bias voltage of the sensor has to be increased in the course of time. In the beginning of operation, the bias voltage is 150 V. The maximum applicable voltage is 600 V.

Another problem after irradiation is surface damage. After accumulation of positive charge in the surface layer and negative mirror charge in the top region of the bulk, low resistivity channels between the n$^+$ pixels can occur once the bulk is inverted to p-type. To avoid these channels, the pixel sensors employ a moderated p-spray isolation. I.e., areas with p-type doping between the pixel implantations neutralise the negative mirror charge and assure isolation of neighbouring pixels.

After operation of about three years at design luminosity, the sensors in the B-layer are

expected to be not operational any more due to high radiation damages. In contrast to that, the sensors in layer 1 and layer 2 are expected to survive the anticipated lifetime of the ATLAS experiment of ten years.

As mentioned in Section 4.1, a MIP generates approximately 20000 electron-hole pairs in the pixel sensor. After ten years of operation, the signal in a module of layer 1 is expected to degrade to 15000-19000 e^- due to radiation damages [A+08a].

5.3 The Front-End Chip

The understanding of the functionality of the Front-End (FE) chip [A+08a, Hue04, Per04] is of particular interest, when investigating the timing behaviour of the pixel detector. The FE chip receives the sensor signal through a bump bond connection and forms the first readout stage. It is designed to be radiation hard and Single Event Upset (SEU) tolerant. On one pixel module, 16 FE chips are arranged in two rows of eight chips. The chip is implemented in 0.25 μm CMOS technology, each chip has 2880 pixel cells arranged in 18 columns by 160 rows. Each pixel cell has an analogue block, supplied by the voltage $V_{dda} = 1.6$ V, and a digital block, supplied by the voltage $V_{dd} = 2.0$ V. The clock for the chip is provided by the 40 MHz LHC clock.

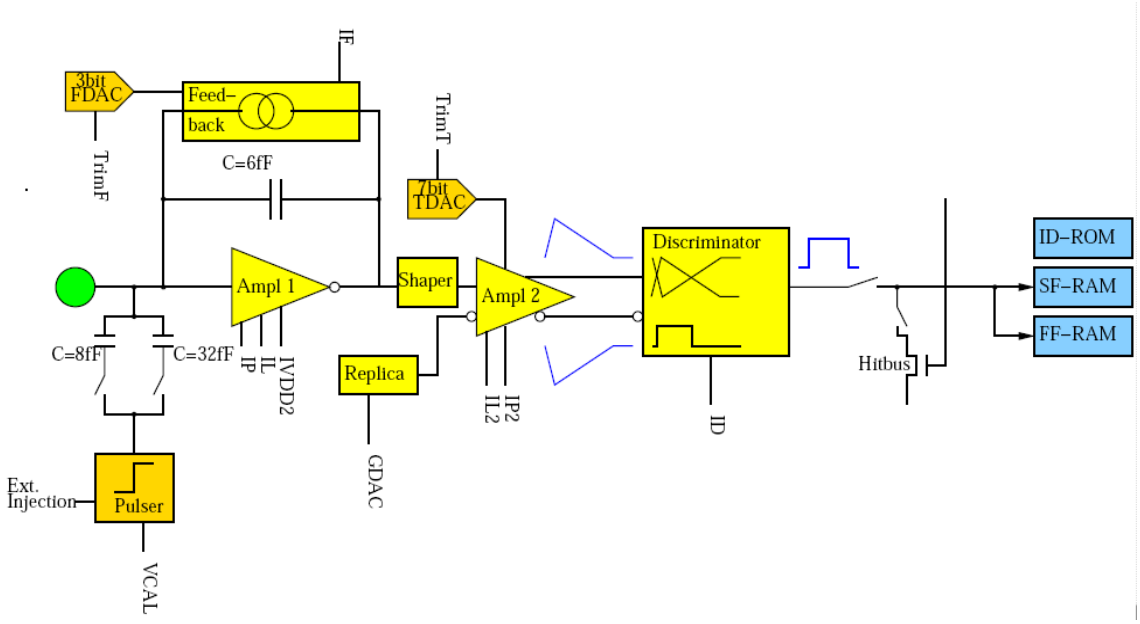

Figure 5.4: Block diagram of the analogue part in an FE pixel cell [Fli06].

Figure 5.4 shows a simplified block diagram of a pixel cell in the FE chip. On the left hand side the bump bond connection to the sensor cell is marked. The signal is fed into the charge sensitive preamplifier. It is then integrated on a feedback capacitor and discharged by the feedback circuit. Since the signal is DC-coupled to the readout section, the feedback circuit also has to avoid the leakage current being integrated on the feedback capacitor. This leakage current is expected to be up to 100 nA after irradiation [A+08a].

The leading edge of the signal delivered by the preamplifier can be regarded to be linear (see Section 6.1). The discharge of the feedback capacitor is performed by a constant current to obtain an approximately triangular signal. Two DAC's allow adjustment of the slope of the trailing edge of the signal: the eight-bit global IFDAC acts on all pixels of the FE chip, whereas the three-bit FDAC is adjustable for each pixel separately. Analogue preamplifier signals for different charges and different adjustments of the feedback current are displayed in Fig. 5.5.

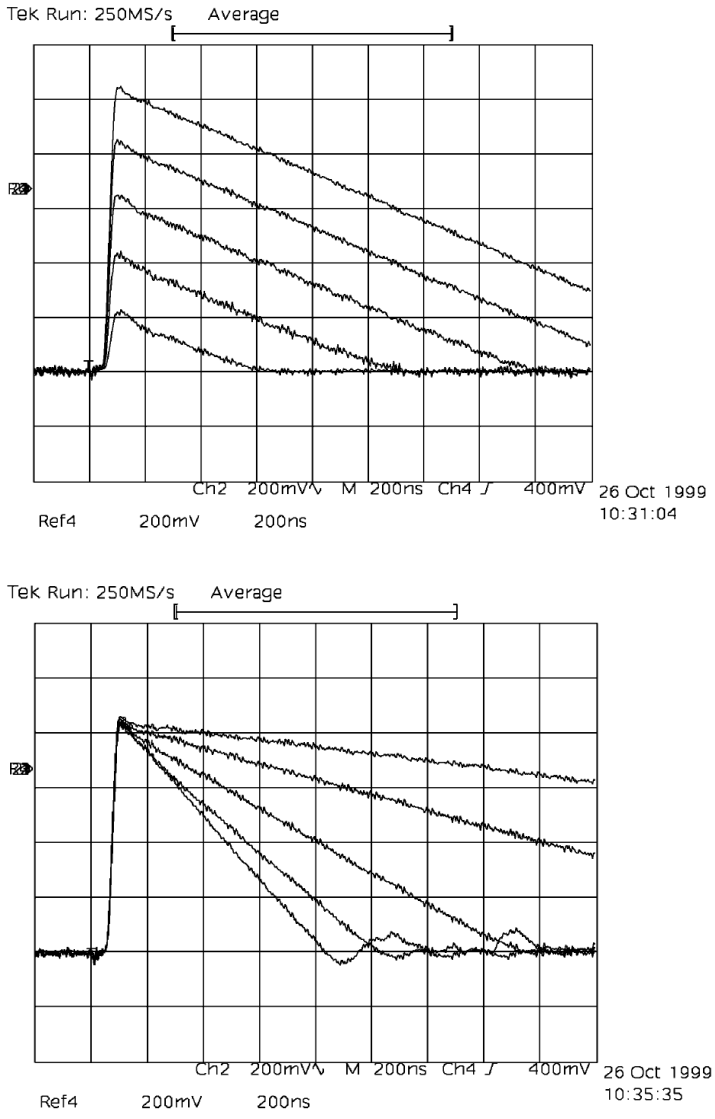

Figure 5.5: Analogue output signals of the preamplifier as measured with a prototype of the FE chip. The upper figure shows signals for different charges varied in steps of $\approx 5000\ e^-$. The lower figure shows the effect of different feedback current adjustments [Fis00].

The analogue signal of the preamplifier is digitised by the discriminator. The digital signal

starts when the analogue signal crosses a certain threshold and ends when the analogue signal falls below the threshold again. As will be described in Section 6.1, the time until the maximum of the analogue signal is independent of the pulse height. This leads to the fact that signals of low charge cross the threshold later than signals with high charge. This timewalk effect is discussed in detail in Section 6.1. The threshold can be adjusted on FE chip level by the global five-bit GDAC and, on pixel level, by the seven-bit TDAC. Usually, the threshold is adjusted to an equivalent input charge of 4000 e^-.

For calibration and test purposes, an injector chain can create either analogue or digital pulses. Analogue pulses are created by charging an injection capacitor C_{inj} with capacitance of either $C_{low} \approx 8$ fF or $C_{high} \approx 32$ fF. The capacitors C_{low} and C_{high} are present in each pixel. Each FE chip has copies of these capacitors, the capacitances of which were measured during module production. The resulting values are used for all capacitors in the respective FE chip, where the variations are assumed to be small. The ten-bit VCAL DAC, which exists once per FE chip, generates a well-defined potential V_{cal} and charges the injection capacity. The charge $Q = C_{inj} \cdot V_{cal}$ is injected into the preamplifier. The charge is chosen by specifying the VCAL DAC value. The conversion from VCAL DAC value into charge is made via the third order polynomial:

$$Q = C_{inj}(a\ Vcal + b\ Vcal^2 + c\ Vcal^3)/e, \tag{5.2}$$

where Q is the charge of the pulse measured in electrons, *Vcal* is the VCAL DAC value and e is the elementary charge. The values of the injection capacitance C_{inj} and the parameters a, b, c have been determined during module production for each FE chip. The injection is initiated by a strobe signal, generated by the MCC. This strobe signal can also be injected after the discriminator to generate a digital signal with defined length, without using the analogue electronics of the FE chip.

The digital part of the FE is illustrated in Fig. 5.6. Two neighbouring columns share a common readout logic. The End of Column (EoC) region contains an arbitration unit, several buffers and logic elements for readout of the pixel cells. All pixel cells in the column pair are connected by busses for the data transfer.

Each pixel cell has two RAM cells to store a time stamp for the leading edge and the trailing edge of the digitised signal. These RAM cells receive an eight-bit Gray coded counter which operates at the 40 MHz LHC clock frequency. Therefore, the timing information for the leading and the trailing edge is available in units of 25 ns. The time between the signal edges is approximately proportional to the charge deposited in the sensor or generated by a calibration pulse. This time corresponds to the time when the preamplifier signal is above the threshold. It is referred to as Time over Threshold (ToT). This coarse information on the charge of the signal is later read out for each hit. The ToT-charge relation depends on the adjustment of the feedback current of the preamplifier and is usually tuned to obtain ToT=30 clock cycles for a signal with charge $Q = 20000\ e^-$.

After the trailing edge of the digitised signal, a hit flag is set in the pixel cell. All hit flag latches in a column pair are then connected by an OR-circuit. As soon as at least one hit flag occurs, the pixel cells of the column are searched for hit information. The time

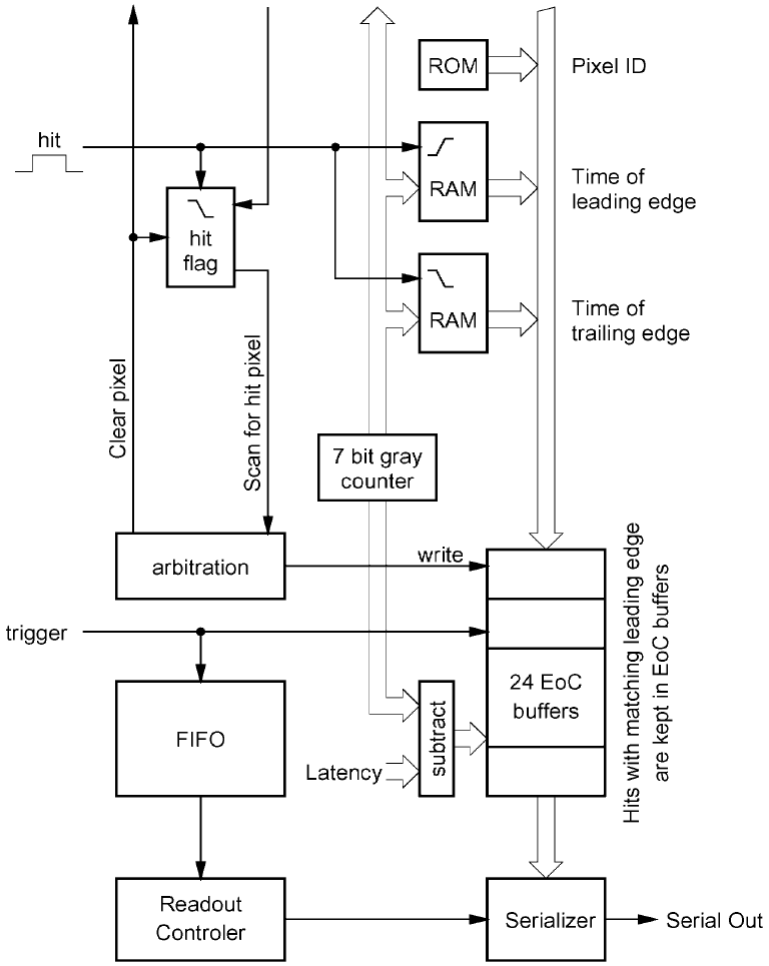

Figure 5.6: The digital part of the FE chip [Fis00].

stamps of the leading and trailing edge and a pixel cell identifier (i.e., row and column) are transferred to the EoC buffers. When the transfer is complete, the hit flag and the RAM cells for the time stamps are cleared. The EoC logic calculates the ToT value as the difference between the trailing edge and leading edge of the signal. Furthermore, the EoC logic can apply a timewalk correction: If a hit has a ToT value below a programmable threshold, the hit can be copied, but with the leading and trailing edge of the preceding bunch crossing. This hit doubling can compensate for the problem that hits with a very low charge are assigned to the wrong bunch crossing due to the timewalk effect (see Section 6.1).

A second Gray coded counter, which runs with the actual clock delayed by a programmable latency, is continuously compared to the time stamps of the leading edges for hits stored in the EoC buffers. When both time stamps coincide and no LVL1 trigger signal arrives in the current clock window, the hit information is discarded. Otherwise, the hit is kept and flagged with an identifier of the current trigger signal. The latency corresponds to the delay between an event and the arrival of the LVL1 trigger signal in the FE chip. It can

be up to 256 clock cycles. The latency acts as an upper limit for measurable ToT values. The identifiers of incoming LVL1 trigger signals are stored in a FIFO memory. The trigger identifiers are consecutively extracted from the FIFO and the EoC buffers are searched for hit information with corresponding trigger identifiers. Finally, the hit information is serialised and sent to the Module Controller Chip (MCC). The hit information contains the pixel row, the pixel column and the ToT value.

5.4 The Module Controller Chip

The Module Controller Chip (MCC) [B$^+$02, A$^+$08a] manages the communication between the FE chips and the Readout Driver (ROD). As with the FE chip, the MCC is designed to be radiation hard and is implemented in a 0.25 μm CMOS process. Figure 5.7 shows a simplified block diagram of the MCC internal architecture. The MCC has three main tasks: Storing configuration data and loading configuration data into the FE chips; distributing timing signals (such as bunch crossing clock and LVL1 trigger signals) to the FE chips; performing the readout of the FE data, event building and transmitting the events to the readout system. These tasks will be explained below, with an emphasis on timing related functions.

Before data taking, the FE chips and the MCC must be calibrated. For example, the values for the DAC settings, as determined during threshold or ToT tuning, must be transmitted to the FE registers. For configuration of the MCC, the registers in the register bank (see Fig. 5.7) have to be written. This comprises also settings for the calibration strobes when performing calibration scans (see Section 6.3).

The distribution of timing signals is mainly accomplished in the Timing, Trigger and Control (TTC) unit of the MCC. Upon receipt of a LVL1 trigger signal, the MCC determines the number of events not yet fully processed. If those are less than 16, the LVL1 trigger signal is transmitted to the FE chips. Otherwise the trigger signal is not forwarded. The MCC is able to repeat the incoming trigger signal up to 15 times. This feature is often used during calibration scans or test runs if several events are to be read out from consecutive clock cycles. Furthermore, the TTC unit houses a counter for the Bunch Crossing Identifier (BCID) and LVL1 Identifier (L1ID). The contents of both counters are stored in a FIFO memory, when the MCC sends a LVL1 trigger signal to the FE chips. Both counters, BCID and L1ID, are reset upon receipt of a Bunch Counter Reset (BCR) signal or an Event Counter Reset (ECR) signal, respectively. The BCR is issued at the end of each LHC cycle, whereas the ECR signal has no fixed frequency. The ECR is sent to cure module problems. It resets the whole event data in the MCC, which are not yet transmitted to the ROD.

The TTC unit is also responsible for sending strobe signals to the FE chips to be used for calibration scans. The strobe signal is used to initiate internal injections of charge accumulated on the injection capacitors as described in Section 5.3. For timing related calibration scans and test measurements, the TTC unit has a delay mechanism, which can delay the strobe signal with respect to the bunch crossing clock. This feature is also used during measurements for the timing studies reported in Chapter 8. To vary the delay of

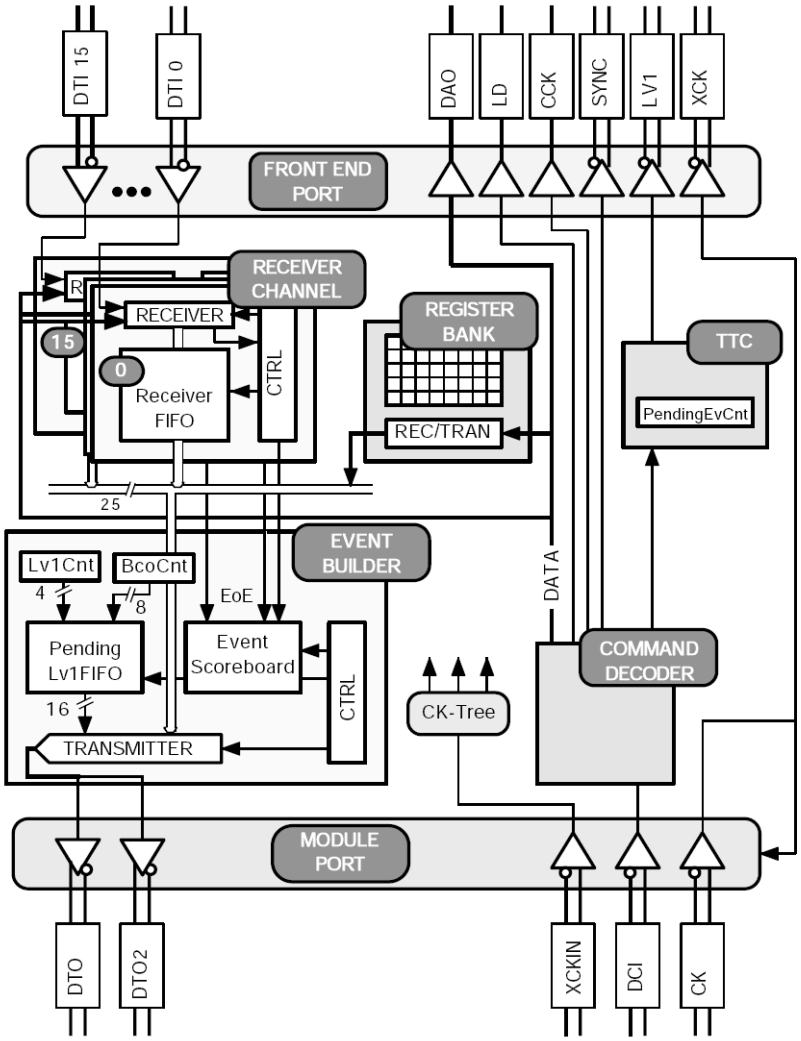

Figure 5.7: Block diagram of the internal architecture of the MCC [B+02].

a strobe signal, one of 15 different delay ranges and a number of up to 63 delay counts have to be chosen. The delays per delay count differ between ≈ 0.4 ns/count for delay range zero and ≈ 2.5 ns/count for delay range 15. The exact value of a certain delay range differs from MCC to MCC and is temperature-dependent (see Section 6.5). Additionally, the offset for the strobe injection is different for different delay ranges and MCC's. Both the offset value and the time per delay count are investigated with the analogue T0 scan (see Section 6.3.2). Usually, delay range five is used during timing related calibration scans, which corresponds to a delay of about 1 ns/count. The delay range and the number of delay counts has to be specified in the eleven-bit MCC register CAL [BD04]. Bit <10> enables the strobe mechanism, bits <9:6> specify the delay range and bits <5:0> specify the number of delay counts. The width of the strobe signal is set in the 16-bit MCC register CNT and specifies the width in units of 40 MHz clock cycles.

For the task of event building, received data from the FE chips are initially deserialised

and buffered in FIFO memories. When the data transfer for one event from the FE chips to the MCC is complete, the event building process starts. One event contains the address of hit pixels (FE number, pixel row and pixel column), the ToT value, BCID and L1ID for the corresponding event. The event data are sent via Low Voltage Differential Signals (LVDS) to the optoboards. Each pixel module has two output channels, the maximum transfer rate per channels is 80 Mb/s. It is foreseen to use both channels for B-layer modules due to the high expected rate and only one channel for the other modules.

5.5 Pixel Detector Readout

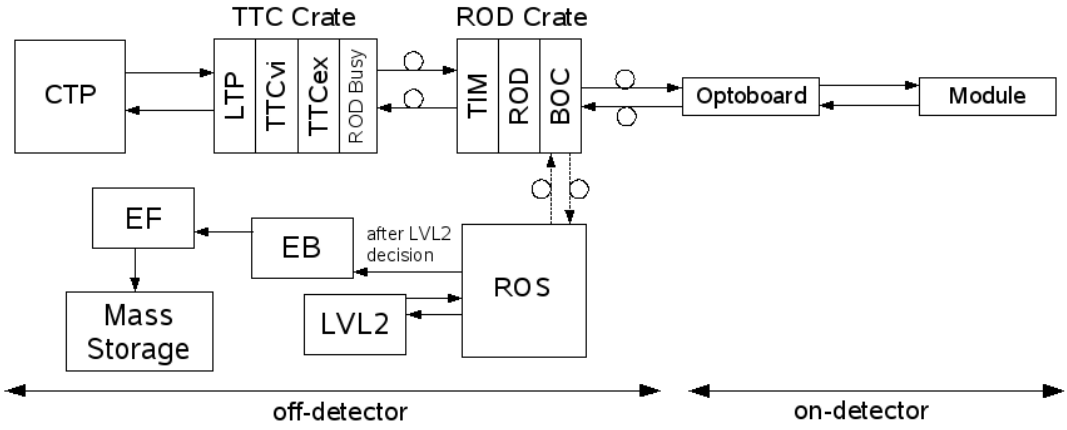

Figure 5.8: Block diagram of the Pixel Detector readout system and distribution of trigger signals. The off-detector part is located in the ATLAS counting rooms, the on-detector part is inside the detector volume.

The Pixel Detector readout system is illustrated in Fig. 5.8. The Central Trigger Processor (CTP), which exists once at ATLAS, sends trigger and timing signals to the TTC crate. The Pixel Detector has one TTC crate housing three partitions, each containing a Local Trigger Processor (LTP), a TTC VME interface (TTCvi), a TTC encoder and transmitter (TTCex) and a ROD busy module [A$^+$05a]. The partitions are Daisy chained and receive in total only one link from the CTP. The data sent by the CTP comprise the 40 MHz bunch crossing clock, LVL1 trigger accept signals, information on the trigger type, orbit signals (sent once per LHC cycle) and ECR signals. In the LTP, the data are received and transmitted to the TTCvi, which acts as an interface to the VME bus and forwards the data to the TTCex module. Here, the data are converted into optical signals and sent to the ROD crates via optical fibres. Additionally, the TTC crate contains a ROD busy module, which receives busy signals from the TTC Interface Module (TIM) and disables the transmission of trigger accept signals to the ROD crates.

5.5.1 The Readout Electronics Crate

The TIM, which exists once per ROD crate [A$^+$08a], receives the TTC data and distributes them to the ROD's and to the Back Of Crate (BOC) cards, which are housed in the same VME crate. The Pixel Detector readout system has 132 ROD's and BOC's distributed over 9 crates. The TIM can delay incoming LVL1 trigger signals and generate random triggers with a programmable rate for test purposes. Furthermore, it sends ROD busy signals to the TTC crate.

The ROD coordinates the communication with the detector modules and fulfils monitoring tasks. It contains essentially three sections: the control path, the data flow path and the Digital Signal Processor (DSP) farm. The control path controls calibration procedures and transmits configuration data to the modules. It further propagates trigger signals from the TIM to the modules. The data flow path receives module data and builds event fragments. These fragments are sent to the Readout System (ROS). The DSP farm monitors events from the modules and creates histograms with, for example, module occupancy. It checks for transmission errors and analyses event fragments during calibration.

Each ROD is connected to a BOC card through the back plane of the VME crate. The BOC card converts electrical signals (coming from the ROD) into optical signals (going to the modules) and vice versa. Optical data sent to the pixel modules are Biphase Mark (BPM) encoded [C$^+$04]. For data transmission to the ROS, it has a Simple- Link (S-LINK) implementation to convert electrical signals with ROD event fragments into optical signals for the ROS. Additionally, the BOC card houses the essential feature for fine timing adjustments of the pixel modules. As discussed in Section 6.2, the TTC signals sent to the modules can be delayed for each module separately, in order to assign a maximum number of hits to the correct bunch crossing.

5.5.2 Optical Data Transmission

The BPM encoded data are transmitted via optical fibres from the BOC cards to the optoboards and vice versa. One fibre per module transmits timing and trigger signals to the optoboards. In the other direction, the data are transmitted by two fibres per B-layer module and by one fibre for the other modules. The fibres are approximately 80 m long.

The optoboard [A$^+$05c] controls the communication for the six or seven modules from one sector or one halfstave. It provides the conversion between BPM coded optical signals and LVDS transmission. Optical BPM encoded signals are received by a PIN diode and decoded by a Digital Opto Receiver Integrated Circuit (DORIC). The DORIC extracts data and clock from the BPM data stream and sends them on so-called Type 0 cables of about 1 m length to the modules. In the Vertical Cavity Surface Emitting Laser (VCSEL) Driver Chip (VDC), LVDS data coming from the modules are converted into signals appropriate to drive a VCSEL. The VCSEL creates the optical BPM encoded signal and sends it via optical fibres to the BOC cards. The Pixel Detectors has 272 optoboards.

5.5.3 The Readout Subsystem

The ROD fragments are transmitted to the Readout System (ROS) via an S-LINK connection. The ROS consists of commercial high performance server PC's. It stores the event data and makes them available for the LVL2 trigger. As described in Section 2.2.4, data are discarded if not selected by the LVL2 trigger. Selected events are forwarded via the Event Builder (EB) to the Event Filter (EF), where a further selection happens. Finally, selected events are transmitted to mass storage.

Chapter 6

Timing Issues

This chapter introduces timing related characteristics of the ATLAS Pixel Detector. The timewalk effect, described in Section 6.1, is the underlying effect. It requires accurate timing adjustments for each pixel module, but the effect can also be exploited to determine the required adjustments. The methods to determine the required settings are described in Chapters 7 and 8. The results obtained from timing related calibration scans, described in Section 6.3, are needed as input for the methods to determine the timing settings.

6.1 Timewalk Effect

As described in Section 5.3, the sensor signal (or the signal from a charge injection) is amplified and digitised in the FE chip. The digitisation applies a simple threshold technique: As soon as the preamplifier signal crosses a certain threshold, the discriminator fires. Due to the timewalk effect, hits which deposit low charge in the sensor, are detected later than hits with high charge. This behaviour and implications on hit detection will be described in this section.

The charge sensitive preamplifier receives a signal with total charge Q either from the sensor or from the injection circuit. The preamplifier response can be approximated by [Per04]

$$v_{out}(t) \approx \frac{Q}{C_f} \frac{\tau_f}{\tau_f - \tau_r} \left(\exp\left(-\frac{t}{\tau_f}\right) - \exp\left(-\frac{t}{\tau_r}\right) \right), \tag{6.1}$$

where C_f is the feedback capacitance, τ_r is the rise time and τ_f is the feedback time. Figure 6.1 shows a plot of the pulse shape. The FE chip has a preamplifier with rise time $\tau_r \approx 15$ ns and feedback capacitance $C_f \approx 5$ fF [A$^+$08a]. The feedback time is variable and is adjusted by the ToT tuning. Typically, a signal with input charge $Q = 20000\ e^-$ is tuned to have ToT = 30 BC (Bunch Crossings). This corresponds to the feedback time $\tau_f \approx 500$ ns.

The pulse can, in a good approximation, be regarded as triangular. The amplitude of the output pulse is independent of the input pulse form, as long as the input pulse width is small compared to the feedback time [Per04]. Thus, pulses from internal injections can be regarded to exhibit the same timewalk behaviour as signals delivered by the sensor. The peaking time t_{peak}, which is the time when the output pulse has reached its maximum, is

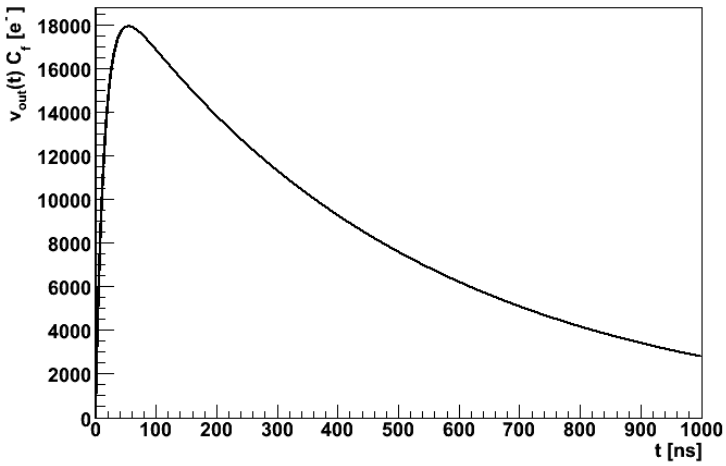

Figure 6.1: Output pulse of the preamplifier (according to eq. 6.1) with rise time $\tau_r = 15$ ns and feedback time $\tau_f = 500$ ns for an input charge $Q = 20000\ e^-$.

given by [Per04]

$$t_{peak} = \frac{\tau_r \tau_f}{\tau_f - \tau_r} \ln\left(\frac{\tau_f}{\tau_r}\right). \tag{6.2}$$

The peaking time is independent of the input charge Q. This leads to the timewalk effect: Signals with low input charge cross the threshold later than signals with high input charge. As described in Section 5.3, the readout is performed in bins of 25 ns. The Bunch Crossing Identifier (BCID) for the bin, in which the threshold is crossed, is assigned to the hit. The BCID numbers each bunch crossing of an LHC cycle consecutively and is reset after the end of an LHC cycle. Thus, hits with low charge, which cross the threshold later, can be assigned to a later bunch crossing. This behaviour is illustrated in Fig. 6.2, with the approximation of triangular pulse shapes.

Figure 6.2 shows the assignment of hits to readout windows for two modules with different clock phases. For module 1, both displayed signals are assigned to the same BCID. This is not the case for module 2: The hit with low input charge is assigned to a later BCID. In reality, such a hit would be lost, since only hits with a certain BCID are used for event reconstruction, when the LHC produces collisions every 25 ns. To assign as many hits as possible to the correct readout window, the clock phase must be optimised. It was agreed to adjust the clock phase such, that the fastest hits, which have high input charge, cross the threshold 5 ns after beginning of a readout window. The 5 ns were chosen as a safety margin and take into account differences in timing behaviour between individual pixels of a module.

For this adjustment and for a threshold of 4000 e^-, hits with a minimum charge of roughly 5400 e^- can be assigned to the correct bunch crossing. This charge is referred to as intime threshold. It differs between the pixels and is determined with the intime threshold scan (see Section 6.3.3) or can be extracted from the timewalk scan (see Section 6.3.4). The most probable charge deposited by a MIP of 20000 e^- is well above the intime threshold.

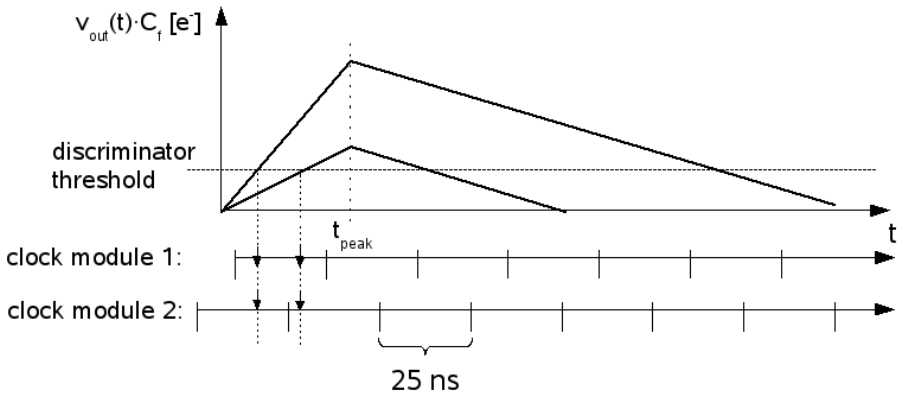

Figure 6.2: Principle of the timewalk effect, with the approximation of triangular pulse shapes for the preamplifier signal. The assignment of hits to readout windows of two modules with different clock phases is shown at the bottom.

However, to have a low intime threshold is important because the deposited charge of traversing particles can be shared between neighbouring pixels. The size of the resulting clusters has been studied with data from the cosmic test [ATL07]. If the charge deposited in one of the hit pixels is below the intime threshold, this pixel does not recognise the hit. This influences the determination of the position of the traversing particle and has an impact on track resolution. If the clock phase is not optimised and if the detection of the fastest hits happens later than 5 ns after the rising clock edge, the intime threshold is higher. Thus, it is of great importance to adjust the clock phase.

Two factors affect the phase between clock edge and arrival of hits: Tolerances in the propagation delays of the clock signals to the pixel modules and time of flight. The former ones include differences in cable lengths and differences in signal processing times at the BOC card, the optoboard and at the module itself. The dominating factors are differences in lengths of the optical fibres, which transmit the clock from the BOC card to the optoboard (see Section 5.5.2). Modules which are supplied by shorter optical fibres receive the clock earlier and therefore see the hits later. Due to differences in time of flight, hits occur later at modules with a larger distance to the interaction point. The time of flight to modules on the outer discs, which have a distance of 65 cm to the interaction point, is about 2 ns longer than the time of flight to modules in the middle of the B-layer.

6.2 Timing Adjustments

The Back Of Crate (BOC) card [Fli06] allows the fine timing adjustment on module level. The BOC card encodes the clock and the data for the modules into a Biphase Mark (BPM) [C$^+$04] data stream. This data stream is transmitted via optical fibres to the optoboards for each module separately.

The BPM encoded data stream can be delayed by a coarse delay (0 to 775 ns in steps of 25 ns) and a fine delay (0 to 35.56 ns in steps of 280 ps). Both delays can be set for

each module separately. The delay leads to a later arrival of the clock at the modules and facilitates to optimise the phase between clock and detection time of the hits. A priori, the phase between the clock and the fastest hits is not known. Methods to determine the delay and thus the necessary timing adjustments are presented in Chapters 7 and 8.

A regulation of the delays affects the Marks Space Ratio (MSR) of the BPM encoded signal [Fli06, Dop07]. This leads to the problem that some readout windows are longer and some are shorter. As a result, the intime threshold differs between the readout windows. This requires a tuning of the MSR to obtain a duty cycle of 50%. Since a regulation of the MSR in turn affects the delay, the timing adjustment should be done in an iterative way: MSR tuning, BPM delay adjustment, MSR tuning.

A further method to cope with timewalk problems is the hit doubling, as mentioned in Section 5.3. Hits below a programmable ToT threshold can be duplicated in the FE logic, where the copy obtains the BCID of the preceding event. This would avoid that hits with low ToT get lost. However, this method also increases the occupancy. Especially, the occupancy due to noise hits, which have primarily low ToT values, would be significantly increased. If this feature will be applied, and if so, with which ToT threshold, is not yet decided.

6.3 Timing Related Calibration Scans

This section presents the different scans to investigate the timing behaviour of the pixel modules. These scans were applied for characterisation of the pixel modules during the production phase. They provide an important input for the timing studies described in Chapters 7 and 8. For these studies, the timewalk behaviour of investigated pixels (or averaged over all pixels in one FE chip) must be known. This description concentrates on procedures implemented in the TurboDAQ software. TurboDAQ is the data acquisition software developed by the ATLAS Pixel Detector collaboration for the pixel module production tests. All calibration scans apply internal charge injection (see Section 5.3). The injected charge is adjusted by the ten-bit VCAL DAC.

6.3.1 Threshold Scan

The threshold scan is actually not a timing related scan, but it can be regarded as the basis of all timing scans described in the next sections. A fixed number of different charges is injected into the input of the preamplifier with the internal injection chain. For each charge, the number of detected hits is counted. To read out hits from several consecutive BCID's, the trigger signal is repeated several times in the Module Controller Chip (MCC). This assures that also hits with very low charge, which are detected in later readout windows than hits with high charge, will be read out. Ideally, only hits with charges above the threshold of the discriminator are detected. Thus, the charge detection efficiency would be a step function (dashed curve in Fig. 6.3). However, due to noise of the detector-preamplifier system, the discriminator fires already for some injections with charge below the threshold and does not fire for some injections above the threshold. The efficiency curve, which is ideally a step function, is smeared and shows an S-curve like profile (solid

curve in Fig. 6.3).

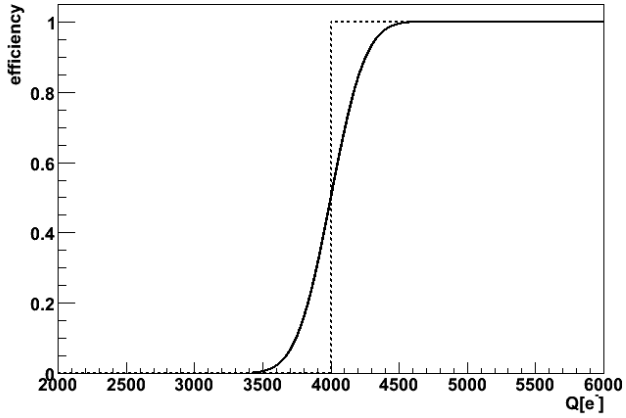

Figure 6.3: Efficiency curves of a threshold scan with a threshold of $Q = 4000\ e^-$ (simulation): The dashed curve shows an ideal step function, whereas the solid curve shows the efficiency smeared out by an equivalent noise charge of $\sigma = 200\ e^-$.

The threshold scan is applied to determine the threshold and the equivalent noise charge of each pixel. It can be repeated with different TDAC and GDAC settings (see Section 5.3) to find the required settings for the threshold aimed at. The threshold is the charge for an efficiency of 50%. This value can be extracted from a fit of an S-curve to the efficiency data points. The fit function is a convolution of a step function and a Gaussian:

$$E(Q) = \frac{1}{2}\left(1 - \mathrm{Erf}\left(\frac{Q_{thr} - Q}{\sqrt{2}\,\sigma}\right)\right), \tag{6.3}$$

where Q is the charge of the injected pulse, Q_{thr} is the charge corresponding to the discriminator threshold, σ is the equivalent noise charge and $\mathrm{Erf(x)} = \frac{2}{\sqrt{\pi}} \int_0^x \exp(-t^2)\,\mathrm{d}t$ is the error function.

6.3.2 Analogue T0 Scan

The analogue T0 scan has two goals: (1) determination of the delay between detection of the fastest hits of internal injections and beginning of a certain clock window and (2) calibration of the MCC strobe delay circuit. Pulses with high charges ($Q \approx 100000\ e^-$) are injected and the MCC delay counts are scanned from 0 to 63 (the maximum value) for a selected delay range.

Figure 6.4 illustrates the principle of the analogue T0 scan: the displayed output signal of the preamplifier originates from an injection pulse with high charge and zero MCC strobe delay counts. For a pulse with high charge, the rising edge of the output signal is approximately vertical and the discriminator threshold is crossed almost immediately. The next eight clock windows are read out. Thus, the displayed pulse is not detected. The MCC counts are increased stepwise to shift the rising edge of the analogue signal. For

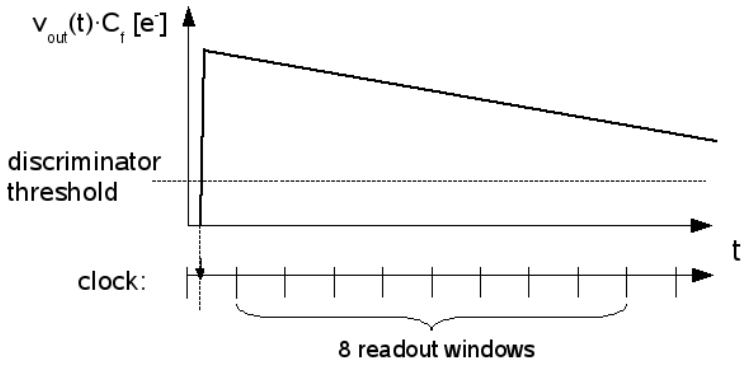

Figure 6.4: Preamplifier response to a high charge signal with zero MCC delay counts. The 8 clock windows, which are read out in the T0 scan, are marked.

each number of MCC counts, the efficiency of detected hits is registered. The obtained efficiency curve is similar to that from the threshold scan (see Fig. 6.3), but with the delay, specified in ns, on the horizontal axis. The conversion from MCC counts into delay time is obtained from two analogue T0 scans with different trigger delays (see below). The scan is repeated for each pixel and an S-curve fit to the efficiency is performed. From this fit, the delay t_0 for an efficiency of 50% is extracted. This delay specifies the required delay to detect 50% of high charge pulses at the beginning of the clock window aimed at. The average value of all pixels in one module is needed for the intime threshold scan (see Section 6.3.3). Figure 6.5 shows a histogram with the t_0 results for all pixels in one module. It has to be noted that ModuleAnalysis, the software which is used to visualise and evaluate the data from production scans, labels the results of the analogue T0 scan in units of MCC delay counts. However, the output given by TurboDAQ is in units of "real" ns (according to the source code of TurboDAQ). A conversion between ns and MCC delay counts is not implemented in ModuleAnalysis and hence the plotted results are also in units of ns, in contradiction to the label.

The calibration of the MCC strobe delay circuit is the second goal of the analogue T0 scan. For this task, the T0 scan is executed for two different trigger delays. Firstly, the scan is executed as illustrated in Fig. 6.4 and secondly with beginning of the readout one clock window later. The T0 results are extracted from an S-curve fit as described above. Two histograms as the one shown in Fig. 6.5 are obtained. Since the difference between the peaks is exactly 25 ns, the delay conversion factors can be determined as:

$$\frac{delay}{count} = \frac{25 \text{ ns}}{\overline{t_{02}} - \overline{t_{01}}}, \tag{6.4}$$

where $\overline{t_{01}}$ and $\overline{t_{02}}$ are the results (averaged over all pixels from one module) of the first and second T0 scan, measured in MCC strobe delay counts. The determination of the delay count conversion is initially done with delay range five (roughly 1 ns/count). If the delay per count falls below a threshold, the conversion is determined for delay range 6 (which has a slightly larger delay per count than range 5) and if necessary for range 7 and so on. Finally, the analogue T0 scan is executed as described above with the known delay range conversion. A detailed description of the delay line calibration with TurboDAQ is given

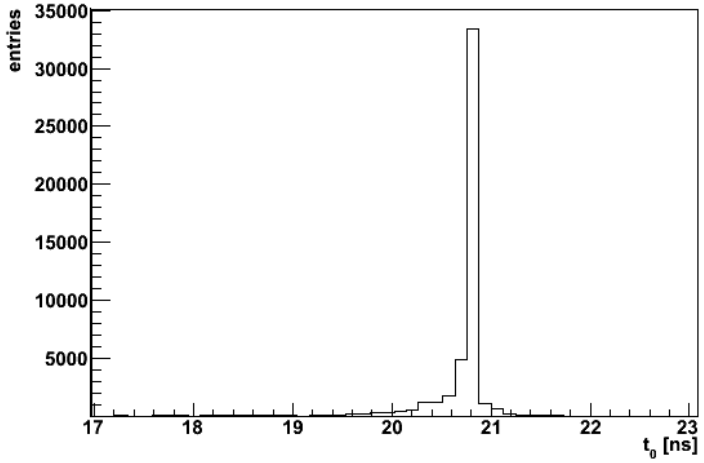

Figure 6.5: Distribution of the t_0 results for all pixels in one module.

in Appendix A.2. The delay conversion factor is used in the final T0 scan to perform the S-curve fit on the efficiency as a function of delay in units of ns.

6.3.3 Intime Threshold Scan

The intime threshold scan requires preadjustment of the MCC strobe delay line, which is set in the way that the fastest pulses cross the discriminator threshold 5 ns after beginning of the clock window:

$$CNT = \frac{t_0 + 5 \text{ ns}}{delay/count}, \tag{6.5}$$

where CNT is the number of counts for the setting, t_0 is the result of the analogue T0 scan (given in ns) and $delay/count$ is the conversion factor from MCC delay counts into ns, as determined with the analogue T0 scan. With this delay fixed, a threshold scan is executed with only one readout window. Only the clock window, in which pulses with high charges cross the threshold, is read out. The results are similar to the results obtained from the threshold scan, yet with a higher effective threshold, which is referred to as intime threshold. The difference between the discriminator threshold and the intime threshold is referred to as overdrive, which is roughly 1400 e^- for a discriminator threshold of 4000 e^-. The overdrive, either on pixel level or averaged over one FE chip, is used as input for the methods described in Chapters 7 and 8.

6.3.4 Timewalk Scan

In the timewalk scan, an analogue T0 scan is repeated for different input charges. For each of these charges, the MCC strobe delay, which is required to detect 50% of the pulses in a certain clock window, is measured. Typically, the readout begins one clock window later than in the analogue T0 scan. To exploit a wide range of charges, both injection capacitors C_{high} and C_{low} are used.

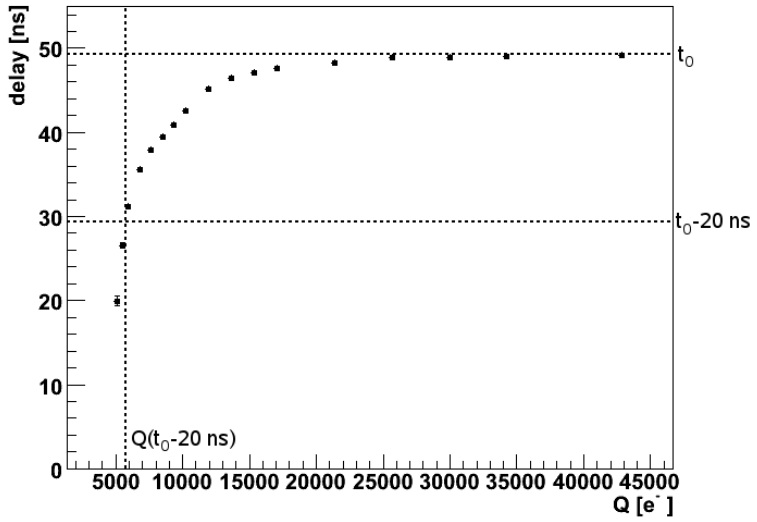

Figure 6.6: Results of the timewalk scan on one pixel for the injection capacitor C_{low}. The dashed lines indicate the extrapolated values (see explanation in the text): $t_0 = 49.3$ ns, $t_0 - 20$ ns $= 29.3$ ns and $Q(t_0 - 20 \text{ ns}) = 5737\ e^-$.

Figure 6.6 shows the results of the timewalk scan for one pixel, measured with the injection capacitor C_{low}. The errors given correspond to 10% of the parameter σ in the S-curve fit (see eq. 6.3). This is arbitrarily chosen to estimate the systematic uncertainty. Errors of the fit parameters from the S-curve fit are not available. In the plot, errors of the charge are not indicated. The plot shows the expected behaviour: Pulses with low charges must be delayed less to detect them in the clock window aimed at, whereas pulses with high charges need to be delayed more as they cross the discriminator threshold earlier. The indicated delay for high charges (t_0) corresponds to the delay obtained in the analogue T0 scan +25 ns, since the readout typically begins one clock window later than in the analogue T0 scan. In Section 6.4 parameterisations of the timewalk curve, which are used for the timing studies described in Chapters 7 and 8, are described.

The overdrive can also be extracted from the data obtained in the timewalk scan. This is automatically done for each pixel by the ModuleAnalysis software. Firstly, the value of t_0 is determined as the delay for a charge of 100000 e^-, using the measurements with injection capacitor C_{high}. Secondly, the charge for a delay $t_0 - 20$ ns is determined. The overdrive is the difference between the charge $Q(t_0 - 20$ ns) and the threshold, which is obtained in a separate threshold scan. For the extraction of t_0 and $Q(t_0 - 20$ ns) the delay between two adjacent data points is extrapolated as a straight line.

The timewalk scan exhibits a timewalk dependency on the pixel type. Since ganged pixels have twice as much load on their preamplifier input as normal pixels, they would show a more distinct timewalk effect. As a compensation, ganged pixels operate with an increased preamplifier bias, which diminishes the effect. Details can be found in [GK08].

6.4 Timewalk Parameterisation

A parameterisation of the timewalk data shown in Fig. 6.6 is required for the timing studies reported in Chapters 7 and 8. It can be obtained using the approximation of triangular pulses of the preamplifier response (see Section 6.1). Since $v_{out}(t) \approx Q(t)/C_f$, one can consider a similar behaviour for the input charge seen by the preamplifier, as shown in Fig. 6.7. The signal is considered to have an almost linearly rising edge and an almost linearly falling edge, the slope of which is given by the feedback constant k. The maximum of the signal, which occurs at the peaking time t_{peak}, is $Q_{sig} - k\ t_{peak}$, where Q_{sig} is the total charge deposited in the sensor or generated with a charge injection.

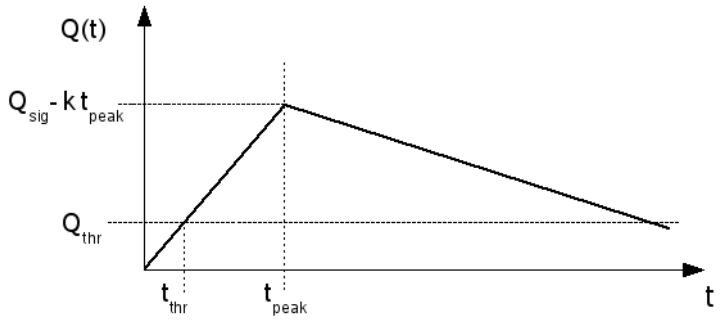

Figure 6.7: Simplified input signal seen by the preamplifier as a function of time. This model is used for the derivation of the timewalk parameterisation.

The time dependent charge of the rising signal edge is

$$Q(t) = \left(\frac{Q_{sig}}{t_{peak}} - k\right) t. \tag{6.6}$$

A hit or a pulse is detected as soon as the signal crosses the threshold ($t = t_{thr}$, $Q(t_{thr}) = Q_{thr}$). Hence, with eq. 6.6 follows:

$$\begin{aligned} Q_{thr} &= \left(\frac{Q_{sig}}{t_{peak}} - k\right) t_{thr} \\ \Rightarrow \quad t_{thr}(Q_{sig}) &= \frac{Q_{thr}\ t_{peak}}{Q_{sig} - k\ t_{peak}}. \end{aligned} \tag{6.7}$$

A higher discriminator threshold leads to a later detection of the pulse. Thus, the timewalk can be reduced by reducing the threshold. However, a lower threshold leads to a higher noise occupancy of the pixel modules.

The timewalk scan does not measure t_{thr} directly. Instead, it measures the necessary delay for a pulse to detect it in a certain clock window: $delay(Q_{sig}) = t_0 - t_{thr}$, where t_0 denotes the delay to apply for high charge pulses. Thus, it follows:

$$delay(Q_{sig}) = t_0 - \frac{Q_{thr}\ t_{peak}}{Q_{sig} - k\ t_{peak}}. \tag{6.8}$$

This parameterisation describes the timewalk behaviour shown in Fig. 6.6. A modified version of that model, described in [DL07], shows an improved agreement with the data:

$$delay(Q_{sig}) = t_0 - \frac{P_0}{(Q_{sig} - P_1)^{2.5}}, \tag{6.9}$$

where t_0, P_0 and P_1 are parameters. The exponential part of the second term leads to a better description especially of the saturation of the delay for high charges. A fit on the data from the timewalk scan on one pixel is shown in Fig. 6.8. The data points are the same as in Fig. 6.6. For the fit, the error of the charge is set to 10%. This takes into account the uncertainties in the conversion of VCAL settings into charge and the variation of the injection capacitance over an FE chip. The data points are below the fitted curve in some charge regions and above the curve in other regions. So far, it could be just statistical fluctuations. However, it turns out to be a systematic effect. Figure 6.9 shows the difference between the mean delay per FE chip per VCAL setting and the value of the fit according to eq. 6.9. The mean delay is calculated as the arithmetic mean of all pixels in an FE chip, omitting ganged and inter-ganged pixels. The curve has been fitted on the mean delays per FE chip. The data originate from 18 VCAL settings and 16 FE chips, altogether 288 data points (each FE chip has a different conversion between VCAL setting and charge). There are oscillations around zero. The behaviour is not completely understood, it could be caused by an insufficiency in the conversion of VCAL settings into charge.

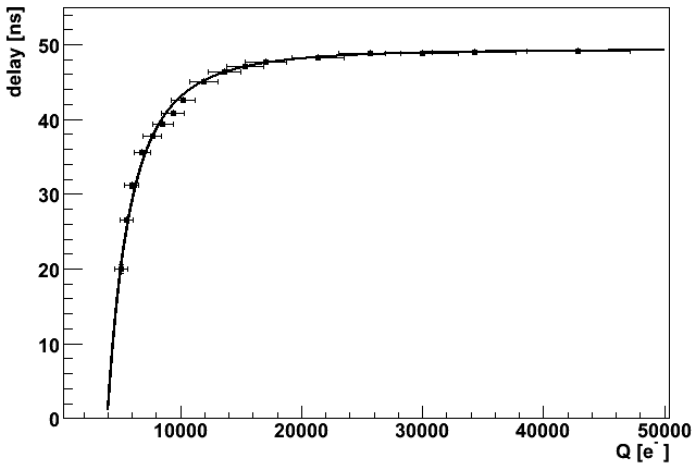

Figure 6.8: Results of the timewalk scan of one pixel for injection capacitor C_{low} with a fitted curve using the parameterisation given in eq. 6.9. The error of the charge is set to 10%. The error of the delay is 10% of the parameter σ of the S-curve fit. The results of the fit parameters are given in Table 6.1.

t_0 [ns]	P_0 [ns $(e^-)^{2.5}$]	P_1 [e^-]	cor (t_0, P_0)	cor (t_0, P_1)	cor (P_0, P_1)
49.4 ± 0.1	$(7.72 \pm 1.66) \times 10^{10}$	-801 ± 745	0.79	-0.70	-0.95

Table 6.1: Results of the timewalk parameters and the statistical correlations of the fit shown in Fig. 6.8

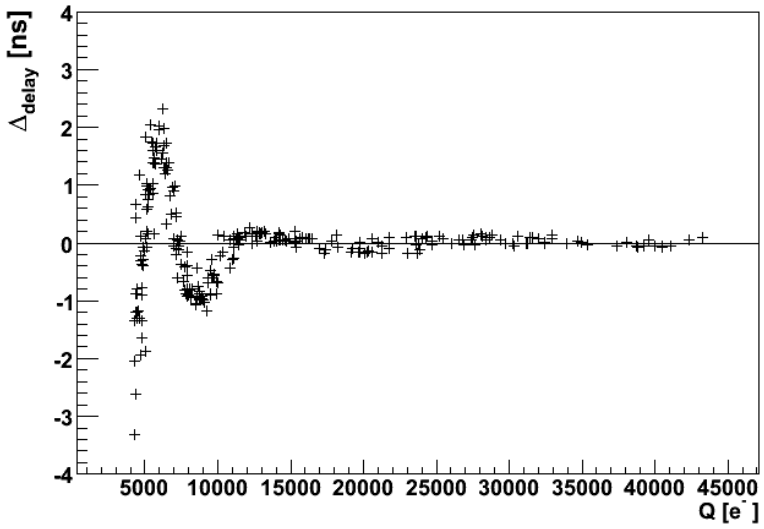

Figure 6.9: Difference between mean delay per FE chip and fit on the data of the timewalk scan from module M510810 at -9.9°C. Errors are not shown.

As shown in [DL07], the timewalk parameters P_0 and P_1 are correlated with the overdrive:

$$\begin{aligned} P_0 &= A_0 \cdot \mathit{overdrive} + B_0, \\ P_1 &= A_1 \cdot \mathit{overdrive} + B_1, \end{aligned} \tag{6.10}$$

$$\begin{aligned} \text{with} \quad & A_0 = 7.675 \times 10^{10}\ \text{ns}\,(e^-)^{1.5}, \quad & B_0 = -2.468 \times 10^{10}\ \text{ns}\,(e^-)^{2.5}, \\ & A_1 = -1.597, & B_1 = 943\ e^-. \end{aligned}$$

This parameterisation is used for the timing studies described in Chapters 7 and 8.

6.5 Temperature Dependency of Timing Scans

The timing studies described in Chapter 8 are based on measurements performed at room temperature ($T \approx 25$°C) at the Pixel Detector test setup at CERN ("ToothPix" [B$^+$08]). As mentioned above, the results of timing scans are needed as input for the data evaluation. However, it was only possible to use data from the intime threshold scan and timewalk scan performed during module production at cold temperature ($T \approx -10$°C). The timing measurements have not been part of the production measurements at room temperature and it was not possible to perform an intime threshold scan and a timewalk scan at ToothPix. Thus, the question arose, whether the timewalk behaviour of the pixel modules is temperature-dependent. To judge this question, measurements of timing scans

at temperatures between $T \approx -10°C$ and $T \approx +23°C$ have been performed at the TurboDAQ setup at the University of Siegen, which was also used for production measurements. The results of these measurements are reported in this section. A general description of a TurboDAQ setup is given in [GK08].

Module	Temperature					
M510667	−9.9°C	+1.5°C	+12.6°C	+16.4°C	+19.7°C	+23.4°C
M510810	−9.9°C	+1.1°C	+12.0°C	+15.8°C	+19.1°C	+22.7°C
M511455	−10.6°C			+16.2°C		+22.9°C
M513127	−10.5°C			+16.0°C		+22.7°C

Table 6.2: Temperatures of the analogue T0 scans performed with four different modules.

Complete module tests (so-called FLEX tests, for details see [A+05b]), as executed during module production, were carried out with four pixel modules. Two modules have been measured at six different temperatures, the other ones have been measured at three different temperatures (see Table 6.2). The indicated temperatures were measured during the analogue T0 scan. The deviation of the temperatures of the other timing scans is ±0.2°C.

6.5.1 Temperature Dependency of the Analogue T0 Scan

Figure 6.10 shows the resulting t_0 from analogue T0 scans at different temperatures. The data points are the arithmetic mean values of all pixels of one module. The mean errors (standard deviation divided by number of pixels) are too small to be visible in the plot. The measured values are listed in Appendix A.1, Table A.1. The modules shown in the upper plot (M510810 and M511455) exhibit a linear decrease of t_0 with increasing temperature. A straight line of the form

$$t_0(T) = A + B \cdot T, \tag{6.11}$$

where T indicates the temperature in centigrade, is fitted to these data points. The results of the fit parameters are listed in Table 6.3.

	M510810	M511455
A [ns]	20.1086 ± 0.0005	24.947 ± 0.001
B $[10^{-2}\frac{\text{ns}}{°\text{C}}]$	-4.853 ± 0.003	-5.342 ± 0.005

Table 6.3: Results of the fit parameters corresponding to eq. 6.11.

To obtain an average value of the temperature dependency of t_0, the weighted mean $\overline{B}$ of the slope of the fit function is calculated:

$$\overline{B} = \frac{\sum B/\sigma_B^2}{\sum 1/\sigma_B^2} \quad \text{with} \quad \sigma_{\overline{B}} = \sqrt{\frac{1}{\sum 1/\sigma_B^2}}, \tag{6.12}$$

resulting in $\overline{B} = (-4.982 \pm 0.003) \times 10^{-2}$ ns/°C.

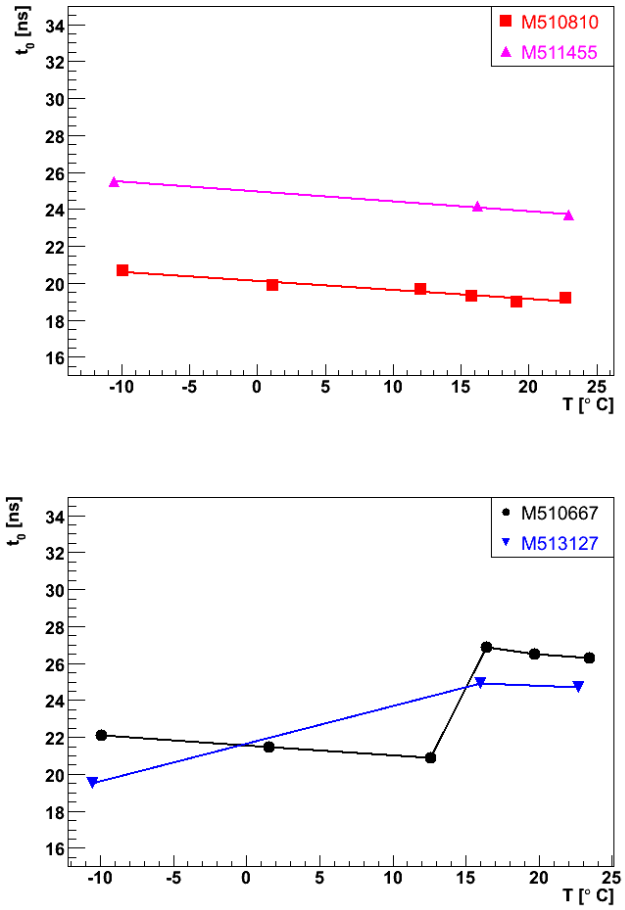

Figure 6.10: Resulting t_0 (arithmetic mean per module) from analogue T0 scans at different temperatures. The data points in the upper plot are fitted with a straight line. In the lower plot, a line between each data point of one module is drawn. The modules shown in the upper plot employ delay range five for all measurements, the modules shown in the lower plot employ delay range six below +13°C and delay range five above +13°C.

The modules M510667 and M513127, shown in the lower plot of Fig. 6.10, exhibit a different behaviour. The t_0 values of module M510667 decrease linearly until a certain temperature ($\approx$ 13°C), rise rapidly and decrease linearly again. Module M513127 seems to behave similarly, although only one data point is available below the jump. This behaviour is correlated with the utilisation of MCC delay range five and MCC delay range six (see Section 5.4). As described in Section 6.3.2, the delay line calibration is initially performed for delay range five. For the modules M510667 and M513127 in the temperatures range $T < 13$°C, the delay per count for delay range five was, however, too small. Thus, delay range six was calibrated and used for the final analogue T0 scans. From $T = 16$°C onwards, delay range five was sufficiently large and was therefore used. So far, the observed behaviour could be caused by different offsets of the strobe signal issued by the MCC for delay range five and six. However, the other timing related scans (intime threshold scan and timewalk scan, see below) exhibit a similar behaviour, which can not

be explained by different offsets. It is assumed that the results of measurements performed with delay range six are incorrect. The TurboDAQ procedure of the delay line calibration and possible failures therein are described in detail in Appendix A.2.

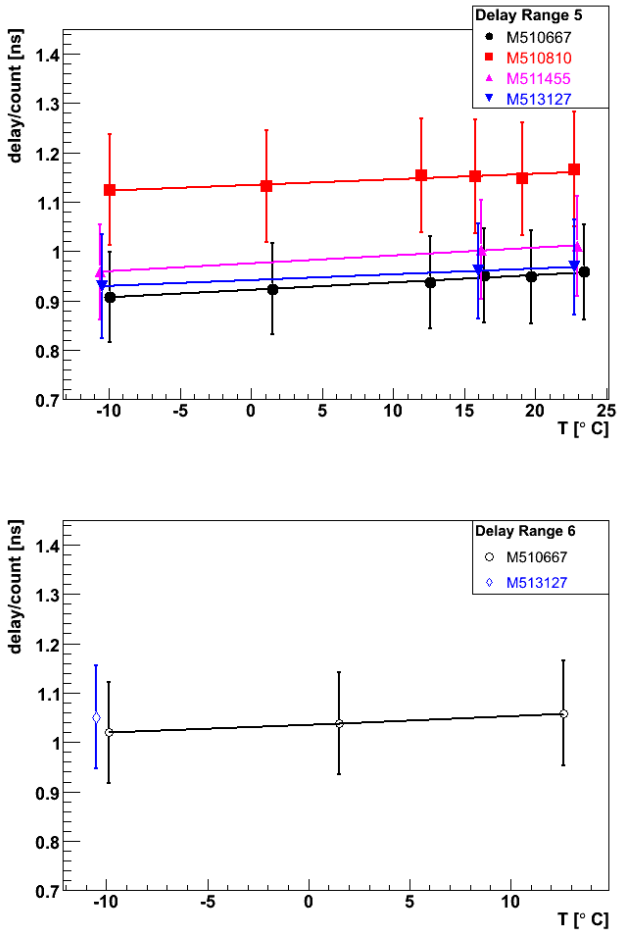

Figure 6.11: Results for the delay line calibration of delay range five (top) and delay range six (bottom) for different temperatures. A straight line was fitted on the data points of the upper plot, whereas the data points of module M510667 in the lower plot are connected by a line.

Figure 6.11 shows the results of the delay line calibration of the four modules. The values are listed in Table A.2 and Table A.3 in Appendix A.1. The results are delivered by TurboDAQ, but no errors are available. The errors shown in the plots correspond to 10% of the delay per count, which is a very conservative estimation. It was motivated by the variation of the delay per count over different modules. The real errors will be well below this value, but the exact value is not of great importance in this case.

Delay range five was calibrated in all measurements, the resulting values of the delay per count are shown in the upper plot of Fig. 6.11. Additionally, delay range six was calibrated for three measurements of module M510667 and for one measurement of module M513127.

Since delay range five was found to be too small in these scans, delay range six was also calibrated. A straight line of the form

$$delay/count\ (T) = A + B \cdot T \tag{6.13}$$

is fitted on the data of delay range five. The results of the fit parameters A and B are given in Table 6.4. The average value of the parameter B, calculated as the weighted mean of the results of the four modules, is $\overline{B} = (1.4 \pm 1.9) \times 10^{-3}$ ns/°C.

	M510667	M510810	M511455	M513127
A [ns]	0.92 ± 0.05	1.13 ± 0.06	0.98 ± 0.07	0.94 ± 0.07
B $[10^{-3}\frac{\text{ns}}{\text{°C}}]$	1.5 ± 3.3	1.1 ± 4.1	1.6 ± 3.9	1.2 ± 4.1

Table 6.4: Results of the fit parameters according to eq. 6.13.

The results show a temperature dependency of both t_0 and the delay conversion factors determined with the analogue T0 scan. With increasing temperature, t_0 decreases and the delay per delay count increases. This is important for the timing studies reported in Chapter 8, where a calculated delay is compared to an adjusted delay value. To determine the adjusted delay, it is of great importance to use the results of the analogue T0 scan performed at the same temperature as the test measurements.

The temperature dependencies of t_0 and the delay conversion factors imply that the MCC strobe delay mechanism is temperature-dependent. It does not imply a temperature dependency of the timewalk effect, which has its origin in the FE electronics. This is investigated in the following subsections.

6.5.2 Temperature Dependency of the Intime Threshold Scan

The overdrive, determined with the intime threshold scan at different temperatures, is shown in Fig. 6.12. The data points correspond to the arithmetic means of all pixels of one module. These values, as well as the adjusted delay counts for each measurement, are listed in Table A.4 in Appendix A.1. As it is the case for the t_0 values, two different behaviours are observed: Modules M510810 and M511455 show approximately temperature-independent overdrives, whereas the overdrives of the modules M510667 and M513127 rise rapidly at a certain temperature. This is again correlated with the employment of delay range five and delay range six. Modules M510810 and M511455 employ delay range five for all measurements. Modules M510667 and 513127 employ delay range six for low temperatures. From $T \approx 16$°C onwards, delay range five is employed. The observed behaviour can not be caused by different offsets for different delay ranges. This phenomenon led to the assumption that the results of measurements with delay range six are probably incorrect. Thus, all timing related scans executed during module production, which employed delay range six, are apparently not reliable.

The overdrive, as long as delay range five is used, does not show an obvious temperature dependency. The fluctuations visible in Fig. 6.12 are due to the fact that the MCC strobe

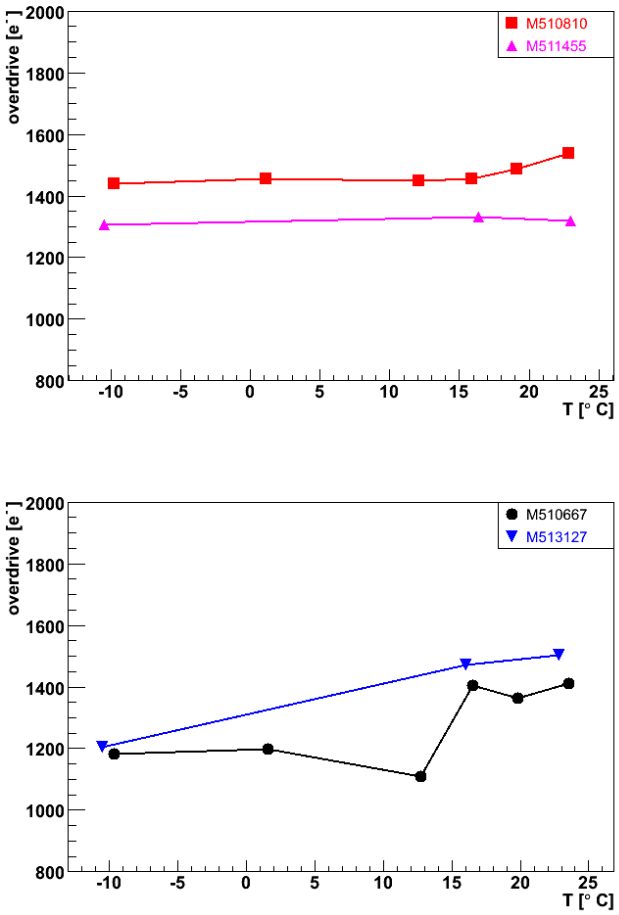

Figure 6.12: Overdrive (arithmetic mean per module) determined with the intime threshold scan at different temperatures. A straight line is drawn between each data point. The modules shown in the top employ delay range five for all measurements, the modules shown in the bottom employ delay range six below +13°C and delay range five above +13°C.

delay can only be adjusted in terms of delay counts, which corresponds to approximately one ns. Therefore, the detection time of the fastest hits is not always exactly 5 ns after the beginning of the clock window. It differs because of alteration of t_0 and of the delay conversion factor.

6.5.3 Temperature Dependency of the Timewalk Scan

Figure 6.13 shows the arithmetic means of $t_0 - 20$ ns, determined with the timewalk scan as a function of the temperature. The errors of the means are too small to be visible. The data are listed in Table A.5 in Appendix A.1. The measured values are expected to correspond to $t_0^{T0} + 5$ ns (see Section 6.3.4), where t_0^{T0} is determined with the analogue T0 scan. This is approximately the case only for all measurements done with delay range five, but not for those done with delay range six. The data of module M510667 below

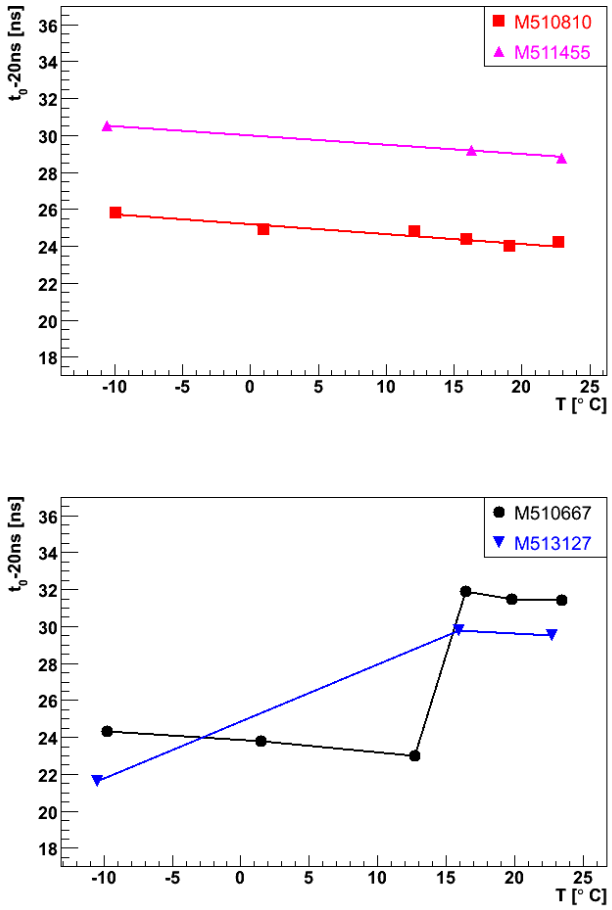

Figure 6.13: Values of $t_0 - 20$ ns (arithmetic mean per module) determined with the timewalk scan. A straight line is fitted on the data points in the upper plot, the data points in the lower plot are connected by a line. The modules shown in the top employ delay range five for all measurements, the modules shown in the bottom employ delay range six below +13°C and delay range five above +13°C.

$T = 16$°C and the data of module M513127 at $T = -10.5$°C are obtained with delay range six. This discrepancy is another indication that measurements with delay range six seem to be not reliable. A straight line of the form

$$t_0 - 20 \text{ ns } (T) = A + B \cdot T, \tag{6.14}$$

where T is the temperature, is fitted on the data of the upper plot. The results of the fit parameters are listed in Table 6.5. The weighted mean of the temperature dependency is $\overline{B} = (-5.207 \pm 0.004) \times 10^{-2}$ ns/°C. Compared to $\overline{B}$ obtained from the analogue T0 scan, this value is approximately 5% larger. However, it has to be noted that only statistical errors are used for the calculation. Systematic effects are not taken into account.
Figure 6.14 shows the overdrives of normal pixels determined with the timewalk scan. The values are listed in Table A.5 in Appendix A.1. The results of long, ganged and inter-ganged pixels do not contribute to the data points. Typically, long and ganged pixels

	M510810	M511455
A [ns]	25.1731 ± 0.0008	29.977 ± 0.001
B $[10^{-2}\frac{\text{ns}}{^\circ\text{C}}]$	-5.348 ± 0.005	-5.005 ± 0.006

Table 6.5: Results of the fit parameters according to eq. 6.14.

show a larger overdrive, whereas inter-ganged pixels show a smaller overdrive than normal pixels. Since the number of the first two pixel types is larger than that of inter-ganged pixels, the mean overdrive of normal pixels is smaller compared to the mean overdrive of all pixels. Therefore, the overdrives shown in Fig. 6.14 are smaller than the overdrives shown in Fig. 6.12, which are determined with the intime threshold scan and which are averaged over all pixels in a module. Apart from that, both plots indicate the same: As long as delay range five is employed, the overdrive is temperature-independent. This leads to the assumption that the timewalk effect is not temperature-dependent at all. However, the shape of the timewalk curve (see Fig. 6.6), for example in the region of medium charges, could exhibit a temperature dependency and not necessarily influence the overdrive.

Timewalk curves for different temperatures are displayed in Fig. 6.15. The data shown in the top are measured with delay range five at all temperatures. Curves measured at high temperatures show a slightly lower delay than curves measured at low temperatures. This is the same behaviour as observed with the analogue T0 scan and has its reason probably in the MCC delay line. It is only an offset and is meaningless for timewalk studies. The timewalk effect itself does not show an obvious temperature dependency in that plot. The lower plot of figure 6.15 shows two groups of curves. The lower group of curves was measured with delay range six, the upper one was measured with delay range five. The bending of the two groups of curves is different, it is therefore not just a simple offset which causes the different behaviours. It is again an indication that measurements with delay range six seem to be incorrect.

Equivalently to Fig. 6.9, the plot in Fig. 6.16 shows the deviation between the timewalk scan results and the fitted curve. A function given by eq. 6.9 is fitted to the arithmetic mean values of all pixels of an FE chip (omitting ganged and inter-ganged pixels). The deviation between the mean values and the fit function value is shown for $T = -9.9^\circ$C and $T = +22.7^\circ$C. In both cases, the reference fit is executed on timewalk data at $T = -9.9^\circ$C. This is of particular interest for the timing studies described in Chapter 8, since the test measurements are performed at warm temperature, whereas the timewalk data utilised originate from the production measurements performed at cold temperature. The deviations shown in figure 6.16 are comparable for both temperatures over a wide range of charges. However, the deviation at $T = +22.7^\circ$C in the range $8000\ e^- < Q < 15000\ e^-$ is approximately 0.5 ns larger. The other investigated modules show the same behaviour, which can be tolerated.

To conclude, a significant temperature dependency of the timewalk effect has not been discovered. Only the MCC delay line shows a temperature dependency. Therefore, it is appropriate to use timewalk data of the production measurements for the timing stud-

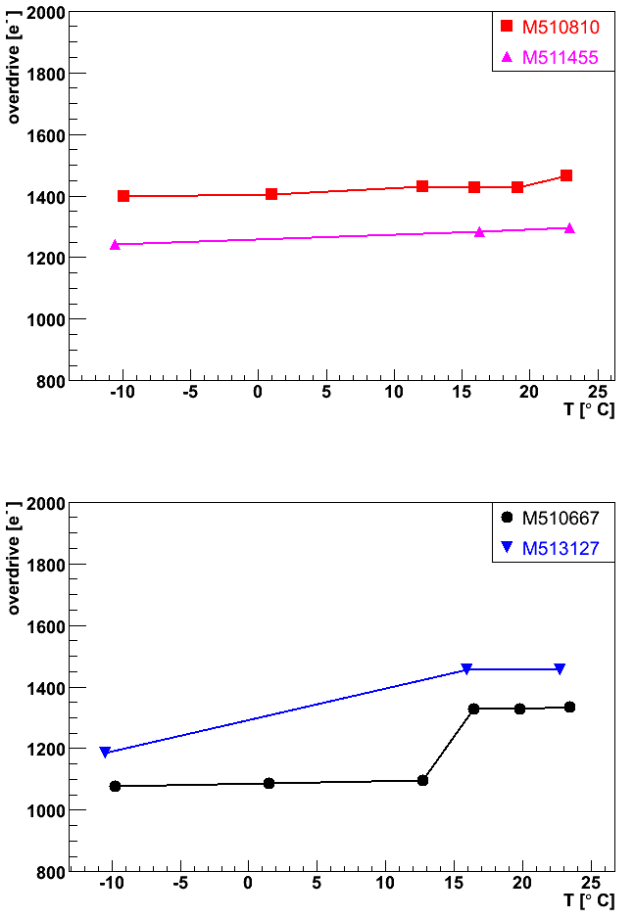

Figure 6.14: Overdrives (arithmetic mean per module) determined with the timewalk scan. A line between each point is drawn. The modules shown in the top employ delay range five for all measurements, the modules shown in the bottom employ delay range six below +13°C and delay range five above +13°C.

ies reported in Chapter 8, as long as delay range five was employed for the production measurements. Appendix A.2 goes into details of the delay line calibration of TurboDAQ and outlines possible reasons for the problem observed when delay range six is employed. Obviously, timing related production measurements performed with delay range six are not reliable.

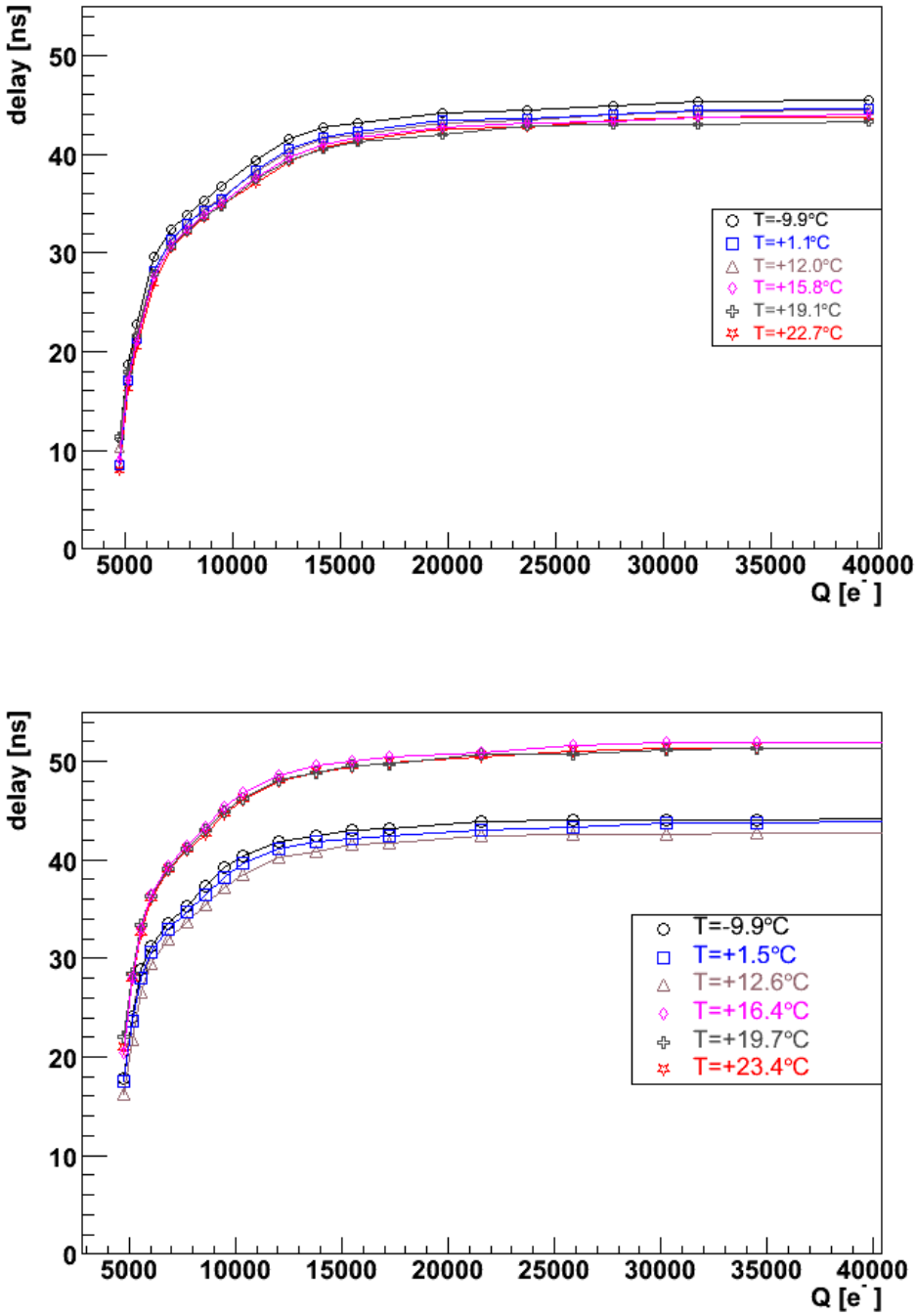

Figure 6.15: Timewalk curves measured with the timewalk scan. The data points reflect the values for a single pixel and are connected with a line, errors are not shown. The measurements shown in the top (module M510810) employ delay range five in the entire temperature range, whereas the measurements shown in the bottom (module M510667) employ delay range six for the lower group of curves and delay range five for the upper one.

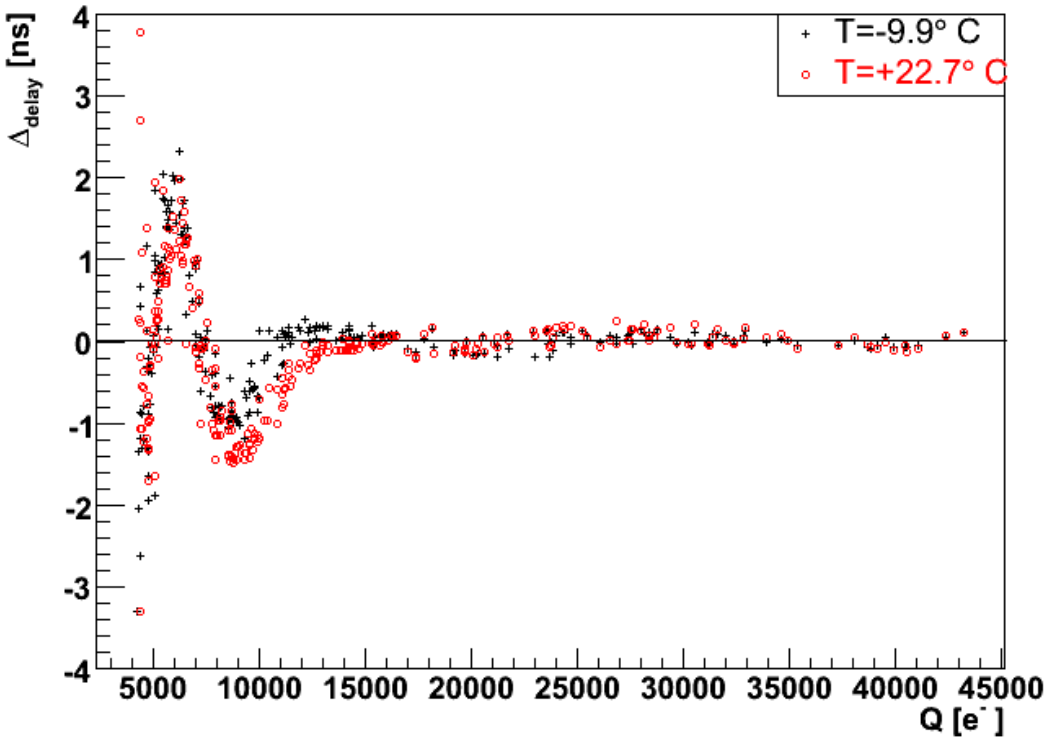

Figure 6.16: Difference between the mean delay per FE chip (for two different temperatures) and the result of the fit to the data of the timewalk scan ($T = -9.9°$C) from module M510810. Errors are not shown.

Chapter 7

Timing Studies with the Cosmics Test

The cosmics test [ATL07] was performed in December 2006 with an end-cap of the Pixel Detector. It was the first commissioning test of a part of the Pixel Detector equipped with realistic services and DAQ components. The cosmics test and its data analysis deliver useful information on the data taking, the offline reconstruction chain and the detector properties, one of which is the timing behaviour. This chapter gives an overview of the cosmics test setup and of the timing studies, which are described in [DL07] and [Pon]. These analyses motivated the timing studies with the ToothPix setup described in Chapter 8.

7.1 Cosmics Test Setup

The cosmics test was performed in the SR1 laboratory at CERN. The setup consisted of the end-cap A of the Pixel Detector with 144 modules, corresponding to approximately 8% of the full detector. The end-cap is subdivided into three discs, each of which has 24 modules per side. To avoid condensation, the end-cap was placed in a dry box. The axis of the end-cap was orientated vertically, to maximise the number of hits from a cosmic muon that passes through the detector volume.

Four scintillators served as a trigger for cosmic rays, see Fig. 7.1. One scintillator was located above the pixel end-cap and three scintillators were located below. The result of a logical *OR* of all the bottom scintillators is fed into a logical *AND* with the output of the top scintillator: the result of this gave the LVL1 trigger decision. The trigger logic was housed in a NIM crate outside the cleanroom. The LVL1 trigger signal was sent to the LTP crate and distributed to the TIM. The readout was managed by the components in the DAQ crate, as for the real Pixel Detector (see Section 5.5). The events selected by a LVL1 trigger decision were directly written to storage and are available for offline data analysis. No LVL2 trigger mechanism was used.

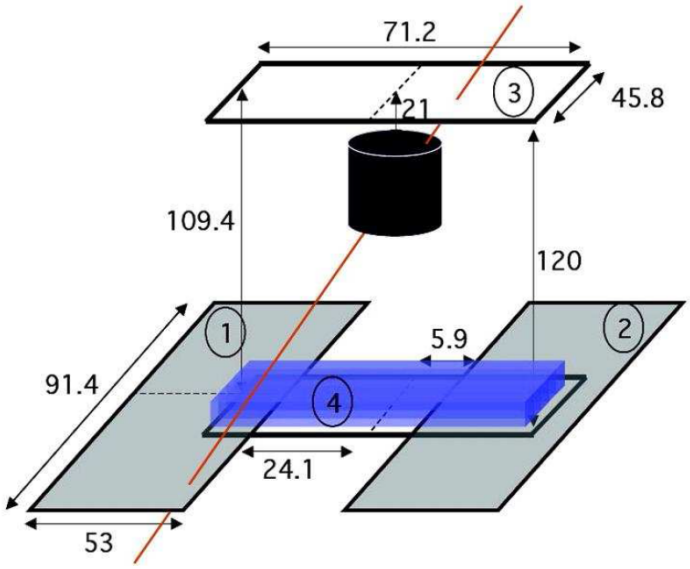

Figure 7.1: The setup of the cosmics test: The end-cap is orientated vertically, one scintillator at the top and three scintillators at the bottom serve as a trigger [ATL07].

7.2 Timing Studies

This section describes the basics of the timing studies described in [DL07] and [Pon]: details can be found in the references.

7.2.1 Analysis Method

For each event selected by a LVL1 trigger decision, 16 clock windows are read out. This is achieved by repeating each LVL1 trigger signal 15 times in the MCC. The LVL1A distributions, which show the number of detected hits as a function of the readout window, are displayed in Fig. 7.2 for two different modules. These distributions contain only hits originating from tracks, which are reconstructed using the ATLAS computing framework Athena. Noise hits, which are detected in all LVL1A bins without correlation with the trigger signal, are eliminated by the reconstruction.

The LVL1A distributions exhibit a distinct peak in bin 5. Some hits are detected in the neighbouring bins, due to the timewalk effect and also the fact that cosmic muons can arrive at any point in the 25 ns clock window. As can be seen in fig. 7.2, the shape of the LVL1A distribution is not the same for all modules: the distribution shown in the left plot has a larger fraction of hits in higher LVL1A bins than the distribution shown in the right plot. This is due to differences in the cable lengths, which influence the delay between the arrival time of cosmic particles and the clock. The effect of time of flight between the modules is limited, considering the length of the end-cap, which is 15 cm. The timing studies utilise the different shapes of the LVL1A distributions to determine the delay between the beginning of a clock window and the average detection time of the highest charge hits. Since cosmic particles arrive randomly with respect to the 40 MHz

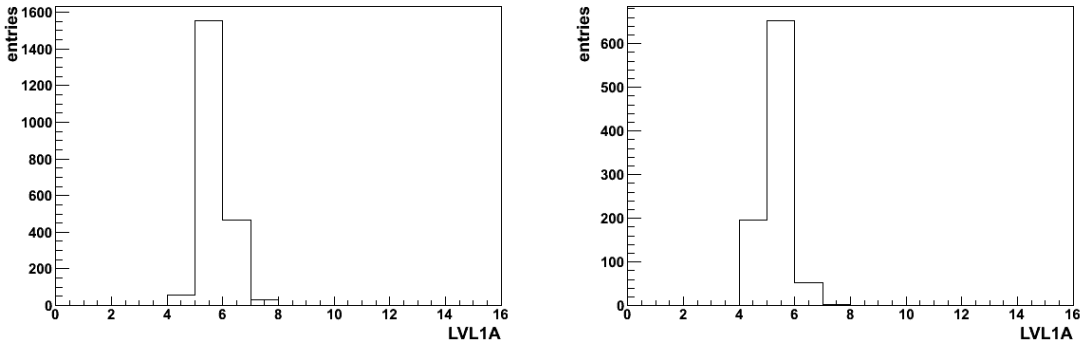

Figure 7.2: LVL1A distributions of module M510254 (left) and M510305 (right) obtained from the cosmics test. The distributions contain only hits from reconstructed tracks.

clock, the hits are detected with a jitter of 25 ns, but the average detection time is fixed.

For this analysis, a simulation is run of the spectrum of charge deposited in the pixel sensor by cosmic muons. The deposited charge of each simulated hit is converted into a delay using the timewalk parameters. Additionally, the delay distribution is smeared according to the jitter of 25 ns. The simulation is performed for each module separately, using the ATLAS computing framework Athena. To minimise the number of input parameters, the timewalk parameters are calculated from the mean overdrive per FE chip (see Section 6.4). The simulated delay distribution can be calculated in bins with a width well below 25 ns. This distribution is then binned into bins of 25 ns and fitted on the LVL1A distribution. The offset for the binning, which determines the shift of the fine distribution against the phase of the binning, is the fit parameter. This is the delay T_0 between the beginning of the readout and the average detection time of the highest charge hits.

7.2.2 Results

Figure 7.3 shows the T_0 results for the modules on disc 0. The results are spread around 130 ns, which corresponds to the delay between the beginning of LVL1A bin 0 and 5 ns after the beginning of bin 5. This is the desired setting: the highest charge hits are detected 5 ns after the beginning of a readout window. This setting ensures that the fastest hits are detected at the beginning of the readout window, so that the number of hits falling into the next window due to the timewalk is small. The additional 5 ns are chosen as a safety margin, in order not to lose hits to the previous readout window, taking into account timing differences between the pixels in a module.

The T_0 for modules in the region $30 \leq \phi \leq 41$ is visibly larger than the average delay. These modules were served by shorter optical fibres than the other modules [Ibr]. Consequently, the clock edges arrive earlier at the modules and the delay between the beginning of a clock window and detection of the hits is increased.

The results of such timing studies of data delivered by the ATLAS Pixel Detector will be used to determine the delay adjustments of the BOC card (see Section 6.2), in order to

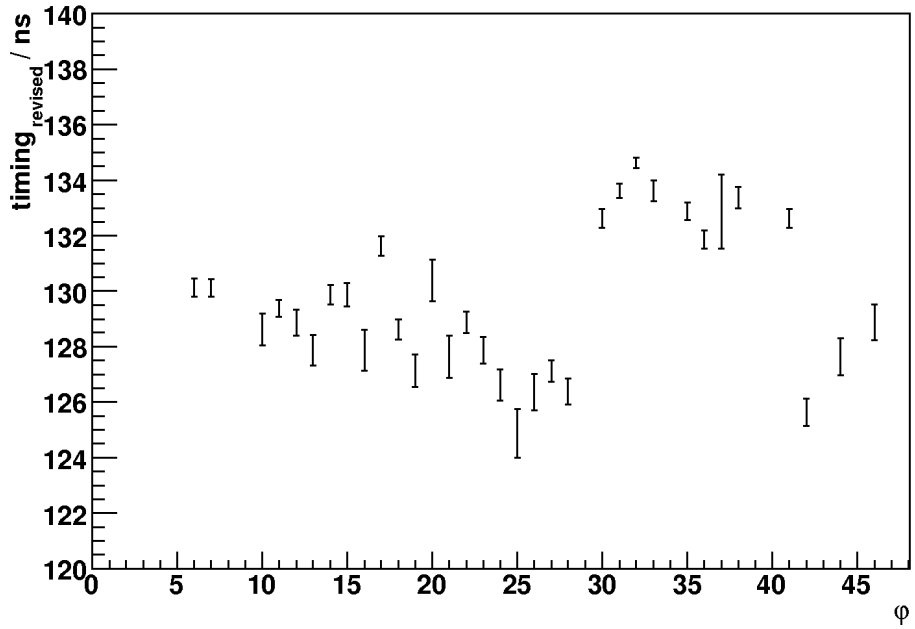

Figure 7.3: Delay T_0 between beginning of the readout and average detection time of the fastest hits for the modules of disc 0. The delay is shown as a function of the module position, which is numbered from 0 to 47 in direction of the angle φ. Some modules have been deactivated [Pon].

achieve an optimal timing for each module. However, the reliability of the analysis is not known. A way of investigating this is described in Chapter 8.

Chapter 8

Timing Studies with the ToothPix Setup

The timing studies performed with data of the cosmics test, as described in Chapter 7, deliver results for the delay between the beginning of a clock window and the detection of the hits which deposit the highest charge in the sensor. The knowledge of these delays, which are obtained on module level, is required to adjust the timing of the Pixel Detector for each module separately. However, it is not yet known what accuracy of the delays is achievable. One way of investigating the reliability of the analysis is to take data with a known delay. Then, the analysis is executed and the calculated delay is compared to the known delay.

The results of such studies are reported in this chapter. The ToothPix ("The Out Of The Hole Pixel Detector") setup [B+08], where the measurements were performed, as well as the measurement procedure and the analysis of the data are described.

8.1 The ToothPix Setup

The ToothPix setup is a Pixel Detector test stand at CERN. It is a small-scale replica of the ATLAS Pixel Detector and is located in the CERN SR1 laboratory. The main areas of application of the setup are the characterisation and development of hardware and software for the Pixel Detector. Especially, the test stand is used for the development and validation of software for the Detector Control System (DCS), Data Acquisition (DAQ) and calibration. Furthermore, it provides the possibility to perform test measurements to study the detector behaviour in a realistic environment.

ToothPix consists essentially of the same components as the real ATLAS Pixel Detector installed in the pit (see Chapter 5). It reproduces realistically the electrical supply and the readout of the Pixel Detector. ToothPix consists of 90 pixel modules, which is approximately 5% of the number of modules present in the real detector. The modules are mounted on three bistaves (containing 26 modules each) and two sectors (containing six modules each). The geometry was designed to allow for cosmics data taking. To maximise the number of hits and to simulate a geometry similar to that of the real detector, two bistaves and the two sectors are arranged in a vertical slice with three layers, see Fig. 8.1.

The third bistave is mounted to one side of the prototype Service Quarter Panel (pSQP), since it has pre-production cooling pipes with a higher danger of corrosion. Therefore, it is connected to a different cooling circuit and separated from the other bistaves.

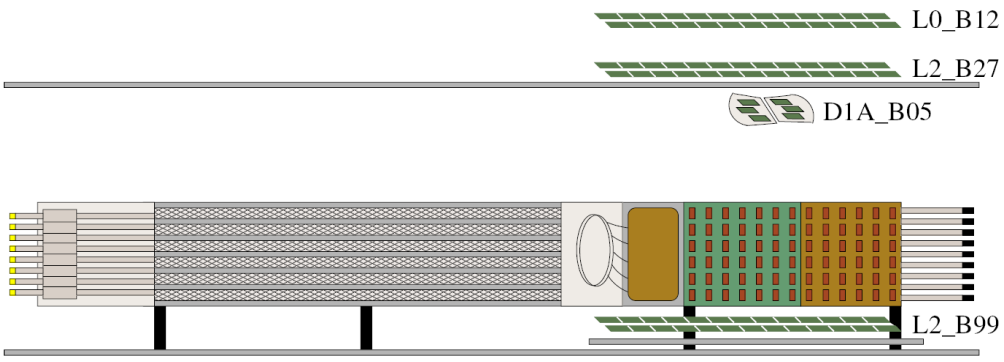

Figure 8.1: The geometry of ToothPix. The pSQP is located inside a coldbox with the bistave L2_B99 at one side. Above the pSQP, the remaining bistaves and the sectors are arranged [B+08].

The pSQP carries the optoboards and connects the supply and readout cables to the pixel modules. There are minor differences compared to the SQP's used in the real Pixel Detector. The cooling of ToothPix is achieved by a monophase cooling system with C_6F_{14} as coolant. In contrast to the real detector, no evaporative cooling is applied, due to the higher effort necessary for the operation of an evaporative cooling system. The temperature of the coolant is set to $\approx 16°C$, which leads to a module temperature of $\approx 25°C$ during data taking. The ToothPix setup is enclosed within a dry box, which is flushed with dry air to prevent condensation.

The readout of ToothPix is essentially the same as for the real Pixel Detector. Optical signals are transmitted between the 24 optoboards and the two readout crates via optical fibres. One readout crate contains three and the other one contains five ROD-BOC card pairs. Each crate also contains one TIM for synchronous data taking and forwarding trigger signals issued by the TTC crate. Data sent from the ROD's are arriving to the ROS, which is replaced by a commercial PC. All events are built and written to disc with the trigger frequency, since there is no high level trigger filtering as for the real detector.

8.2 Measurement Procedure

The timing measurements described in this chapter were performed on one halfstave of the ToothPix setup. The halfstave used is specified as L0_B12_S2_A7. It contains seven modules. However, only four modules are used for the data analysis. Three modules are excluded from the analysis due to different reasons. One module, M510039, was disabled during the tuning and data taking due to problems in the DCS. For a further module, M511395, the MCC strobe delay line was not calibrated for the timewalk scan in the production measurements and hence the timewalk data are not utilisable, which makes

the analysis useless. A third module, M510194, was disabled during the analogue T0 scan at ToothPix (see below). Therefore, the calculated delay can not be compared to the adjusted delay. Table 8.1 lists the modules of the halfstave used. The given stave ID's identify the position on the stave, while the production ID's were assigned to each module during the production phase.

Stave ID	Production ID	Comment
L0_B12_S2_A7_M0	M512906	
L0_B12_S2_A7_M1A	M510194	excluded from analysis
L0_B12_S2_A7_M2A	M511395	excluded from analysis
L0_B12_S2_A7_M3A	M512936	
L0_B12_S2_A7_M4A	M510571	
L0_B12_S2_A7_M5A	M512555	
L0_B12_S2_A7_M6A	M510039	excluded from analysis

Table 8.1: Stave identifiers and production identifiers of the modules on halfstave L0_B12_S2_A7, which is used for the timing measurements.

8.2.1 Tuning

All pixels should have a uniform discriminator threshold. This is of particular importance for timing studies, since the timewalk effect depends on the actual threshold (see Section 6.4). For this reason, a threshold tuning was performed prior to the data taking. As described in Section 5.3, two DAC's are used to adjust the threshold: the GDAC (on FE chip level) and the TDAC (on pixel level). During the threshold tuning, a threshold scan (see Section 6.3.1) is executed for different settings of both GDAC and TDAC. Then, the DAC settings, which result in a threshold close to 4000 e^-, are determined. The threshold tuning is performed with STControl, the calibration software of the Pixel Detector.

Figure 8.2 shows the threshold distribution of module M512555 obtained after tuning with STControl at the ToothPix setup. For comparison, Fig. B.1 in Appendix B shows the threshold distribution of the same module obtained after threshold tuning with TurboDAQ in the production test. The desired threshold was set to 4000 e^- in both tunings. The threshold distribution obtained with TurboDAQ (4175 ± 71, which are the arithmetic mean and the standard deviation) has a larger mean and a larger dispersion than the distribution obtained with STControl (4001 ± 55). Both observations are assigned to different tuning algorithms used in TurboDAQ and STControl.

To obtain a uniform relationship between measured ToT and injected charge, a ToT tuning was performed before the data taking. The feedback current is adjusted by the global IFDAC (on FE chip level) and the FDAC (on pixel level), see Section 5.3. Pulses with charge $Q \approx 20000\ e^-$ are injected and the DAC values are chosen to obtain $ToT = 30$ BC (Bunch Crossings). Since the adjustment of the feedback current affects the discriminator threshold and vice versa, the following tuning sequence was applied: GDAC, TDAC, IFDAC, FDAC, TDAC. The relationship between ToT and injected charge is discussed in Section 8.4.1.

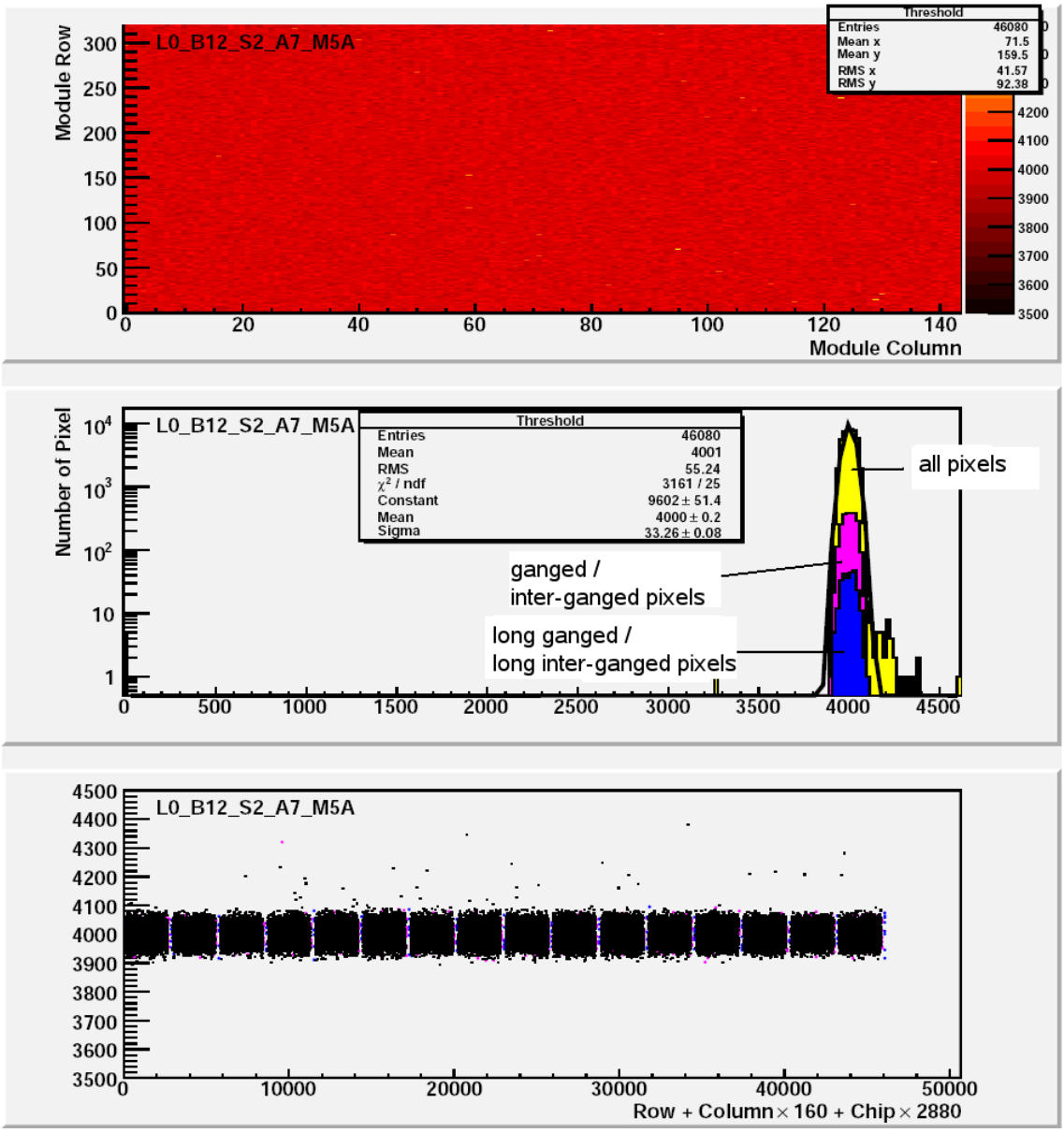

Figure 8.2: Threshold scan performed with STControl at the ToothPix setup: Threshold mean of module M512555 after the threshold tuning. In the upper plot, a two-dimensional map of the threshold for each pixel is shown. The middle plot shows a stacked histogram of the same values, the three different colours correspond to different pixel types. The lower plot shows the threshold as a function of the pixel number.

8.2.2 Data Taking

The measurements were performed with test pulses of internal injection, using the injection capacitor C_{low}. Delay range five was used for the MCC strobe delay, the number of delay counts was set to five different values: 0, 7, 10, 15, 20. The width of the MCC strobe signal was set to 100 clock cycles. For each delay setting, data runs with 29 VCAL DAC values, varied between 75 and 465, were taken. The resulting ToT values reach from about 3 to approximately 30, depending on the pixel. The charge was injected into 32 pixels per module, two pixels per FE chip: column 0 and 8, row 128. The pixels in column 0 are long pixels, while the pixels in column 8 are normal pixels. For the discussion of the results, the investigated pixels are numbered from 0 to 32: pixel 0 corresponds to column 0 in FE chip 0, pixel 1 corresponds to column 8 in FE chip 0, pixel 2 corresponds to column 0 in FE chip 1 and so on.

The TIM delivered the external calibration strobe signal and the LVL1 trigger signal. Both signals were generated with a frequency of 1 kHz. The calibration strobe signal triggers the MCC to send a strobe signal to the FE chip. The LVL1 trigger signal, which was sent 134 clock cycles later, starts the readout. The latency in the FE chips was set to 128. To read out seven consecutive clock windows, the trigger signal was repeated six times in the MCC.

The data taking was controlled with the ATLAS data acquisition software TDAQ. Each run was stopped after about 50 s, to obtain roughly 50000 events. The measurements of all, approximately 150, runs were carried out on six successive days, while the tuning was only performed once in the beginning. Before each data taking run, the modules were configured with the configuration data of the tuning.

The output data are available in bytestream format, for details see [JJF06, B$^+$06]. For the data analysis described in the following sections, the bytestream data are converted into root-files.

8.3 Determination of the True Delay

The true delay T_0^{true} between the beginning of a clock window and the detection of the fastest hits must be known exactly for the validation of the timing analysis methods. As described in Section 6.3.2, the analogue T0 scan calibrates the delay line and determines the delay between the fastest hits and the end of a certain clock window. Both values are necessary for the determination of the true delay. The true delay can be calculated according to Fig. 8.3. The beginning of the readout of the test measurements and the detection time of the fastest hits for zero MCC delay counts is shown (hits with low charge are detected later due to the timewalk effect). A measurement with CNT delay counts has the true delay

$$T_0^{true} = 50 \text{ ns} + CNT \, \frac{delay}{count} - t_0, \tag{8.1}$$

where $\frac{delay}{count}$ and t_0 (in ns) are determined with the analogue T0 scan. The error of T_0^{true} is given by

$$\sigma_{T_0^{true}} = \sqrt{\left(CNT \, \sigma_{\frac{delay}{count}} \right)^2 + \sigma_{t_0}^2}. \tag{8.2}$$

It is important, that in the determination of t_0 with the analogue T0 scan and in the test measurement the same delay range has to be chosen, since otherwise there may be a different offset and hence a different t_0. As described in Section 6.5.1, the results of the analogue T0 scan are temperature-dependent. To minimise the uncertainty of T_0^{true}, the results of an analogue T0 scan executed at ToothPix (with STControl) at the same temperature as the test measurements are used for the analysis.

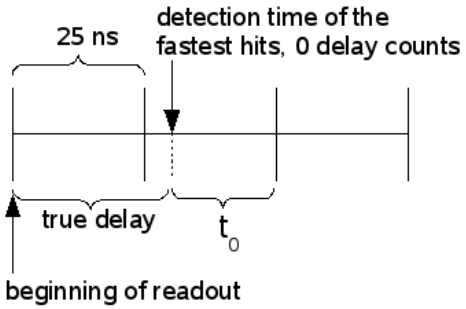

Figure 8.3: Determination of the true delay: beginning of the readout and the detection time of the fastest hits, as determined with the analogue T0 scan.

Table 8.2 summarises the delay conversion factors and the resulting t_0 obtained with the analogue T0 scan for the four investigated modules. Here, also errors of the delay conversion factors are available. The values delivered by STControl for t_0 are given in units of delay counts, the conversion into ns is given by

$$t_0 = t_0^{CNT} \frac{delay}{count}, \tag{8.3}$$

where t_0^{CNT} is the result of the analogue T0 scan in units of delay counts. The error of t_0 is given by

$$\sigma_{t_0} = \sqrt{\left(\frac{delay}{count}\,\sigma_{t_0^{CNT}}\right)^2 + \left(t_0^{CNT}\,\sigma_{\frac{delay}{count}}\right)^2}. \tag{8.4}$$

The error on $delay/count$ includes the errors of the fit parameters from the S-curve fit, in which the delay conversion factor is determined (for each pixel separately). The error of t_0^{CNT} is the mean error of the distribution of all pixels in a module.

Module	$\frac{delay}{count}$ [ns]	t_0 [ns]
M510571	1.0322 ± 0.0001	21.666 ± 0.002
M512555	1.0062 ± 0.0001	23.716 ± 0.003
M512906	1.0009 ± 0.0001	23.992 ± 0.003
M512936	1.1200 ± 0.0001	20.418 ± 0.003

Table 8.2: Delay conversion factors and t_0 for the modules used for the analysis, determined at the ToothPix setup.

8.4 Calibration Parameters

8.4.1 ToT Calibration

The information on the charge of the test pulses is delivered by the detector as Time over Threshold (ToT) in units of Bunch Crossings (BC). Since the timewalk is available as a function of charge, a precise knowledge of the relationship between ToT and injected charge is required for the analysis. Even though the measured ToT for a given charge has been adjusted to be relatively uniform over all pixels by means of the ToT tuning, there are still variations. Therefore, a calibration of the relationship between ToT and injected charge is performed for each pixel separately. In principle, also a relationship determined with the production measurements could be used. However, the relationship depends on the results of the ToT tuning. To avoid uncertainties, the relationship is determined using the ToothPix measurements directly. For the data of the real ATLAS Pixel Detector, a calibration per FE chip and pixel type will be used.

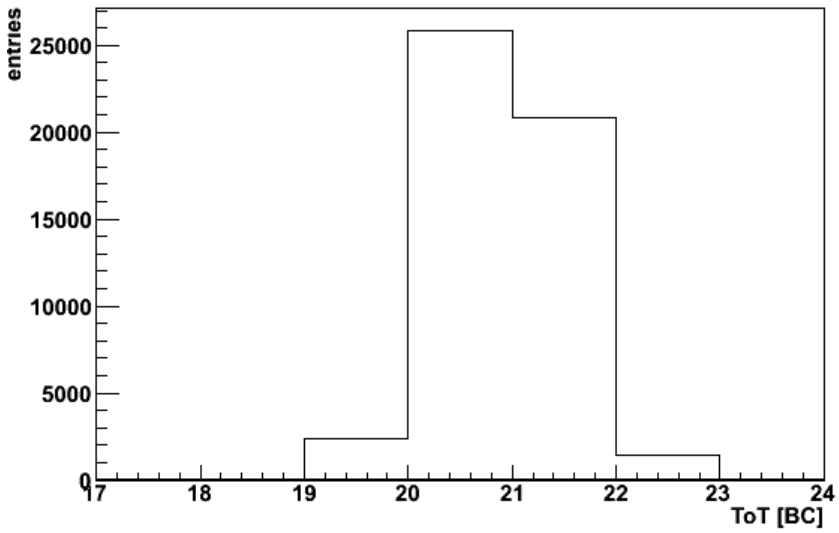

Figure 8.4: Distribution of measured ToT of a single pixel for $Vcal = 300$.

The resulting ToT values for a single pixel for a VCAL DAC setting $Vcal = 300$ are shown in Fig. 8.4. In this example, a distribution with entries in 6 ToT bins is obtained. The ideal distribution would have entries in only one ToT bin. However, the distribution is broadened. The mean ToT of each VCAL DAC setting is calculated for a single pixel and plotted as a function of the injected charge in Fig. 8.5. The VCAL DAC setting is converted into charge using the relationship

$$Q = C_{low}(a\ Vcal + b\ Vcal^2 + c\ Vcal^3)/e, \tag{8.5}$$

as discussed in Section 5.3. The capacitance of C_{low} and the values of the parameters are taken from the production data on FE chip level. The ToT calibration function

$$ToT(Q) = A\left(\frac{Q+E}{Q+C}\right) \tag{8.6}$$

is fitted to the data, where A, C, and E are fit parameters. Accordingly, the charge as a function of ToT is

$$Q\,(ToT) = \frac{A\,E - ToT\,C}{ToT - A}. \tag{8.7}$$

The parameters and the elements of the covariance matrix (the parameters are strongly correlated) for each pixel are used for the analysis. The results of the fit shown in Fig. 8.5 are listed in Table 8.3. For the fit, the error of the ToT is the mean error of the ToT distribution for one VCAL DAC setting and the error of the charge is set to 10%. This error seems to be justified, taking into account the expected variations of the injection capacitance over one FE chip and the errors of the parameters a, b and c in eq. 8.5 [Wei]. The exact errors of the parameters are not available. However, it has to be taken into account that the injection capacitor is present in each pixel, while the determination of its capacitance was performed using copies of that capacitor in one corner of the FE chip. In contrast to that, there is only one VCAL DAC per FE chip. Therefore, the parameters a, b and c of eq. 8.5 are measured directly [Hue].

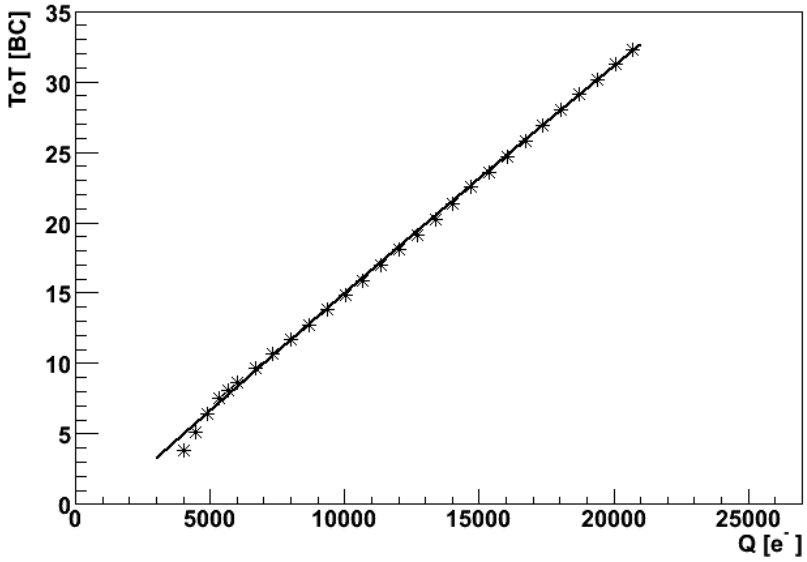

Figure 8.5: ToT against injected charge for a single pixel and fit of the function given in eq. 8.6. Errors are not shown.

Another method, applied in strategy 3 (see Section 8.4.3), is using the average ToT calibration parameters per FE chip for the analysis. The parameters are given by

$$A = \frac{1}{2}(A_1 + A_2) \tag{8.8}$$

with the errors and covariances

$$\begin{aligned} \sigma_A^2 &= \frac{1}{4}(\sigma_{A_1}^2 + \sigma_{A_2}^2), \\ \mathrm{cov}(A, C) &= \frac{1}{4}\left(\mathrm{cov}(A_1, C_1) + \mathrm{cov}(A_2, C_2)\right), \end{aligned} \tag{8.9}$$

where A_i and C_i are the calibration parameters of the two investigated pixels per FE chip. The errors and covariances of the other parameters are calculated in the same way.

A [BC]	C [e^-]	E [e^-]	cor (A, C)	cor (A, E)	cor (C, E)
207 ± 168	$(1.06 \pm 1.03) \times 10^5$	-1800 ± 510	1.00	0.83	0.85

Table 8.3: Results of the fit parameters and statistical correlations of the fit shown in Fig. 8.5.

ToT Dependency on Delay Setting

The measured ToT for a given charge depends slightly on the delay between the clock edge and the crossing of the discriminator threshold (see Fig. 8.6). Pulses crossing the discriminator threshold in the beginning of a clock window show on average a smaller ToT than pulses crossing the threshold at the end of a clock window.

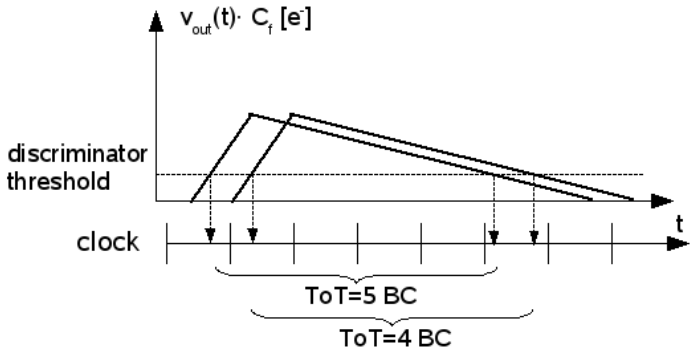

Figure 8.6: Simplified signals of the preamplifier for two pulses with equal charge but different delays. In this example, the pulse with the larger delay shows a smaller ToT.

This behaviour can be investigated with the data taken at ToothPix with different delays. Figure 8.7 displays the measured ToT for selected charges of measurements with different delay settings. The indicated values are the mean ToT of one pixel for a certain VCAL DAC setting, errors are not shown. In the high charge region, shown in the lower plot, the measurements with smaller delay show a smaller ToT. This is the region where signals with high charge and zero delay counts are detected shortly after the beginning of the clock window. The observations are different in the low charge region (shown in the upper plot of Fig. 8.7): for $Q \approx 4700\ e^-$, the measurement with zero delay counts has the smallest ToT, since those pulses are detected at the beginning of the clock window. In contrast to that, the measurement with zero delay counts has the largest ToT at $Q \approx 5100\ e^-$. This happens because those pulses are now detected at the end of the previous clock window – the intime threshold is crossed. The variations of the ToT value due to different delays are below one BC, given the periodicity of the clock.

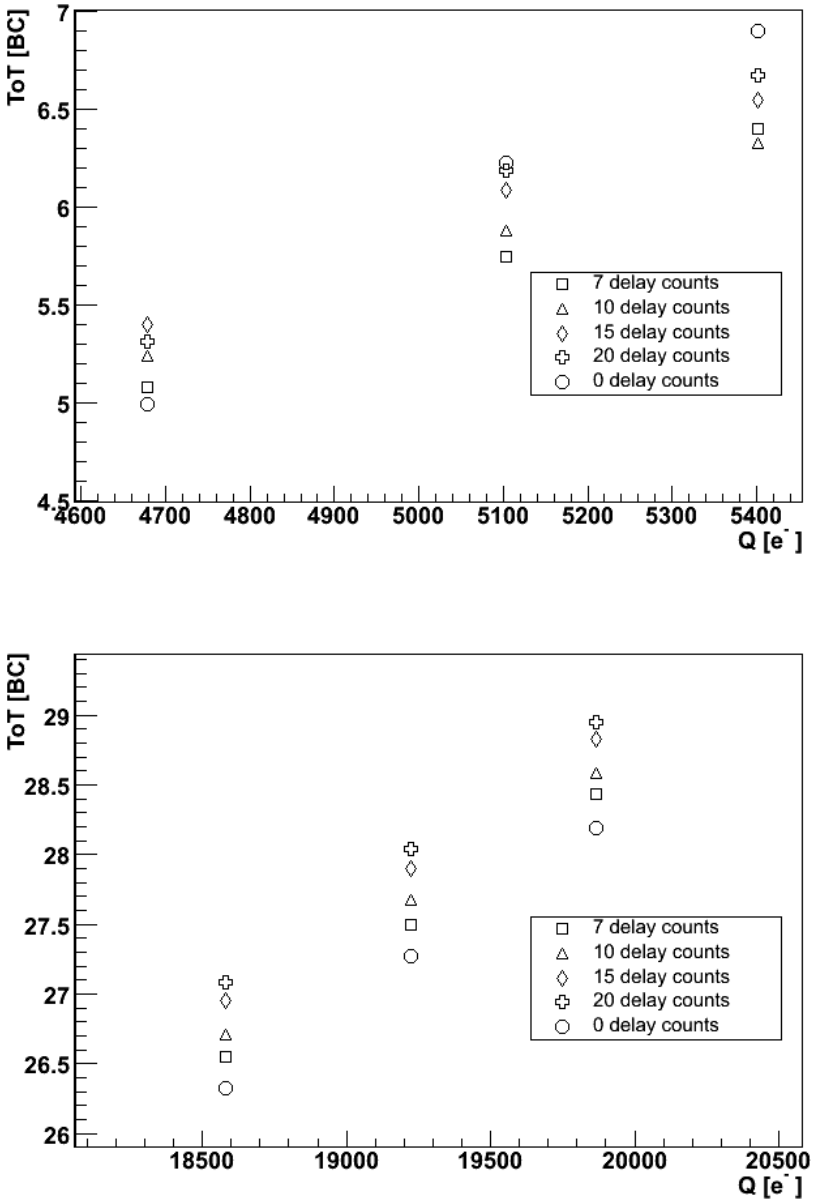

Figure 8.7: Measured ToT for low charges (top) and high charges (bottom) for different delay settings.

As discussed in [GK08], this explains the kink at low charges visible in the plot of ToT versus charge in Fig. 8.5. With increasing charge from below to above the intime threshold, the detection time of pulses moves from the beginning of clock window x to the end of clock window $x - 1$. Consequently, the relationship between measured ToT and injected charge shows a steeper slope in this region compared to the rest of the spectrum.

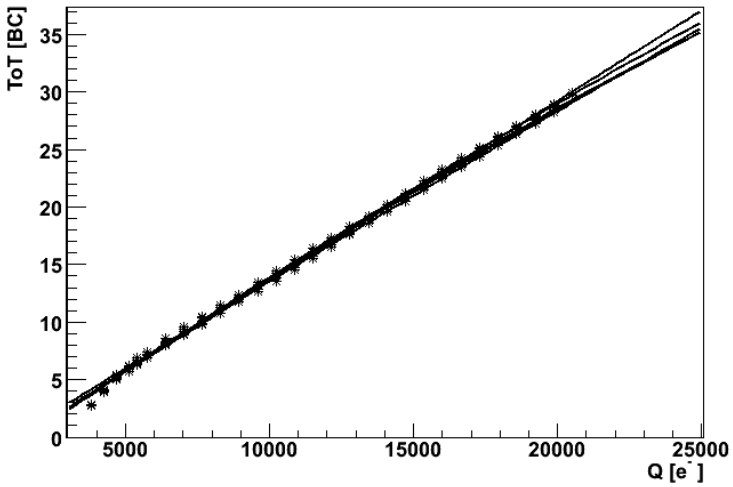

Figure 8.8: ToT against injected charge for a single pixel and fit of the function given in eq. 8.6 for different delay settings (0, 7, 10, 15 and 20 delay counts). Errors are not shown.

The influence of different delay settings on the ToT calibration is depicted in Fig. 8.8. The measured ToT as a function of the injected charge and a fit of the calibration function is shown for the five different delay settings, which are used for the timing measurements. In the region where data points are available, considerable differences are hardly visible. The curves only diverge in the high charge region, where no data points are available. However, the effect on the evaluation of data of the real ATLAS Pixel Detector is probably insignificant, since the variation of the ToT over the pixels in one FE chip is larger. The ToT calibration will be performed on FE chip level and also data points with higher charge will be used for the calibration.

However, if systematic uncertainties of the ToT calibration induced by different delay settings should be avoided, the delay settings used for the ToT calibration and the delay of physical hits must coincide. After the correct timing of the pixel modules is achieved, the hits with high charge will be detected 5 ns after beginning of a clock window. Therefore, the delay of the pulses with high charge, which are used for the ToT calibration, has to be adjusted to 5 ns after beginning of the clock window, too. This is the same setting as used for the intime threshold scan: $t_0 + 5$ ns, where t_0 is determined with the analogue T0 scan.

8.4.2 Timewalk Parameters

The analysis requires timewalk parameters as input. Since the timewalk scan could not be executed at the ToothPix setup, the timewalk fit, as described in Section 6.4, is performed on data from the production measurements. A function given by

$$delay^{TW}(Q) = t_0 - \frac{P_0}{(Q - P_1)^{2.5}} \tag{8.10}$$

is fitted to the timewalk data of each pixel, which is used for the measurements. The timewalk scan measures the delay, which has to be applied to detect injections of a given charge in a certain readout window (see Section 6.3.4). The injections of higher charge require a larger delay than injections of a lower charge. This delay is reflected by the second term in eq. 8.10. The parameter t_0, which can be regarded as an offset, is not important for the analysis, only the values of the fit parameters P_0 and P_1 and the covariance matrix are used. The delay of a charge Q is given by

$$delay(Q) = \frac{P_0}{(Q - P_1)^{2.5}}. \tag{8.11}$$

As mentioned in Section 6.4, the error of the delay measured in the timewalk fit is set to 10% of the parameter σ of the S-curve fit. The error of the charge is set to 10%, which is motivated in Section 8.4.1. Inserting eq. 8.7 into eq. 8.11, the delay as a function of ToT is given by

$$delay\,(ToT) = \frac{P_0}{(\frac{A\ E - ToT\ C}{ToT - A} - P_1)^{2.5}}. \tag{8.12}$$

If the timewalk data are not available, the parameters P_0 and P_1 can be calculated using the overdrive, as described in Section 6.4:

$$\begin{aligned} P_0 &= A_0 \cdot overdrive + B_0, \\ P_1 &= A_1 \cdot overdrive + B_1, \end{aligned} \tag{8.13}$$

$$\begin{aligned} \text{with} \quad & A_0 = 7.675 \times 10^{10}\ \text{ns}\,(e^-)^{1.5}, \qquad B_0 = -2.468 \times 10^{10}\ \text{ns}\,(e^-)^{2.5}, \\ & A_1 = -1.597, \qquad\qquad\qquad\ B_1 = 943\ e^-. \end{aligned}$$

The overdrive is measured by the intime threshold scan. Here again data from the production measurements are used. The values of the parameters A_i and B_i are taken from [DL07], errors are not available. The error of the overdrive of a single pixel, which is the difference between the intime threshold and the discriminator threshold, is

$$\sigma^2_{overdrive} = \sigma^2_{thr} + \sigma^2_{int}. \tag{8.14}$$

However, the errors of the intime threshold, σ_{int}, and of the threshold, σ_{thr}, are not available. As an estimate, 10% of the parameter σ from the S-curve fits, used to determine the intime threshold and the discriminator threshold, is taken. For a parameterisation on FE chip level, the mean overdrive of all pixels in an FE chip can be used. Then, the error of the overdrive is the mean error of the distribution.

If the timewalk parameters are calculated using the overdrive, the errors of P_0 and P_1 and the covariance are given by

$$\begin{aligned} \sigma_{P_0} &= A_0\,\sigma_{overdrive}, \\ \sigma_{P_1} &= A_1\,\sigma_{overdrive}, \\ \mathrm{cov}(P_0, P_1) &= A_0\,A_1\,\sigma^2_{overdrive}. \end{aligned} \tag{8.15}$$

All investigated modules were measured using delay range five during production. Thus, the problems with delay range six (see Section 6.5) are not an issue. As an example, Table 8.4 shows the fit results of the timewalk parameters P_0 and P_1, the statistical correlation and the overdrive of a single pixel.

P_0 [ns $(e^-)^{2.5}$]	P_1 [e^-]	cor (P_0,P_1)	*overdrive* [e^-]
$(7.72 \pm 1.66) \times 10^{10}$	-801 ± 745	-0.95	1550 ± 40

Table 8.4: Example of the timewalk parameters P_0 and P_1, the statistical correlation and the overdrive of a single pixel.

8.4.3 Strategies for Calibration Parameters

The parameters for the ToT calibration and timewalk, used for the analysis methods described in Sections 8.5 and 8.6, are obtained with different strategies:

1. timewalk parameters determined from the timewalk scan on pixel level, ToT calibration parameters calculated on pixel level,

2. timewalk parameters calculated from the overdrive on pixel level, ToT calibration parameters calculated on pixel level,

3. timewalk parameters calculated from the mean overdrive per FE chip, ToT calibration parameters averaged over the two investigated pixels per FE chip.

The analyses are executed for each of these strategies. Although the analyses are performed for each investigated pixel separately, strategy 3 estimates how the results differ, if the parameters are used on FE chip basis. At least, the variation of the results can be investigated, if not the exact parameters for the respective pixel are used. Since the measurements at the ToothPix setup are performed injecting pulses in only two pixels per FE chip, a "real" analysis on FE chip level is not possible.

8.5 LVL1A Fit Method

The LVL1 trigger accept (LVL1A) fit method is one of the methods to determine the delay T_0 between the beginning of a clock window and the detection of the fastest hits. It can be applied, when for each LVL1 trigger signal several consecutive clock windows are read out. This was the case for the cosmics test, as reported in Chapter 7. In this section, the systematic error of the LVL1A fit method is investigated.

The LVL1A distribution shows the number of detected hits as a function of readout clock windows. It is recorded by repeating the LVL1 trigger signal in the MCC, which allows to read out up to 16 consecutive clock windows. Due to the timewalk effect, detected hits are spread over several bunch crossings, depending on the deposited or injected charge. The shape of the LVL1A distribution depends on where exactly in the 25 ns long readout window the fastest hits cross the threshold. Therefore, it can be used to determine the detection time of the fastest hits with a resolution much finer than the readout bin size of 25 ns. Figure 8.9 shows the LVL1A distribution of a single pixel for a measurement with 0 delay counts (top) and 15 delay counts (bottom). A number of hits has moved from the LVL1A bin 1 into the bin 2 in the distribution with the larger delay.

The detection times of hits with the same charge distribution as used to obtain the LVL1A distribution are simulated with fine resolution. The delay T_0 between the beginning of LVL1A bin 0 and the detection of the fastest hits is extracted from a fit of the simulated spectrum to the LVL1A distribution.

8.5.1 Input Data

The LVL1A distributions used for the analysis described in this section are generated using hits following a uniformly distributed ToT spectrum. In the range ToT = 6 ... 27 BC, 400 hits per ToT value are selected. The choice of the kind of the distribution is in principle arbitrary. However, due to the vast number of recorded hits, only a selection can be used for the analysis and, for the sake of simplicity, it is restricted to a uniform ToT distribution. ToT = 6 BC is chosen as a lower limit of the spectrum, since the parameterisations of both the timewalk and the ToT calibration do not work well for lower ToT values. The upper limit of the ToT distribution was chosen to obtain a range where each investigated pixel has at least 400 hits. This procedure differs somewhat from that used for the timing studies with data from the cosmics test, where due to the low statistics all recorded hits were used for the analysis and the simulated ToT spectrum did not match the real ToT spectrum exactly [Pon].

8.5.2 Simulation

The goal of the simulation is to simulate a distribution of the delay times of the injected pulses with fine resolution. Later, this distribution is fitted to the measured LVL1A distribution. The simulation is performed for each pixel separately.

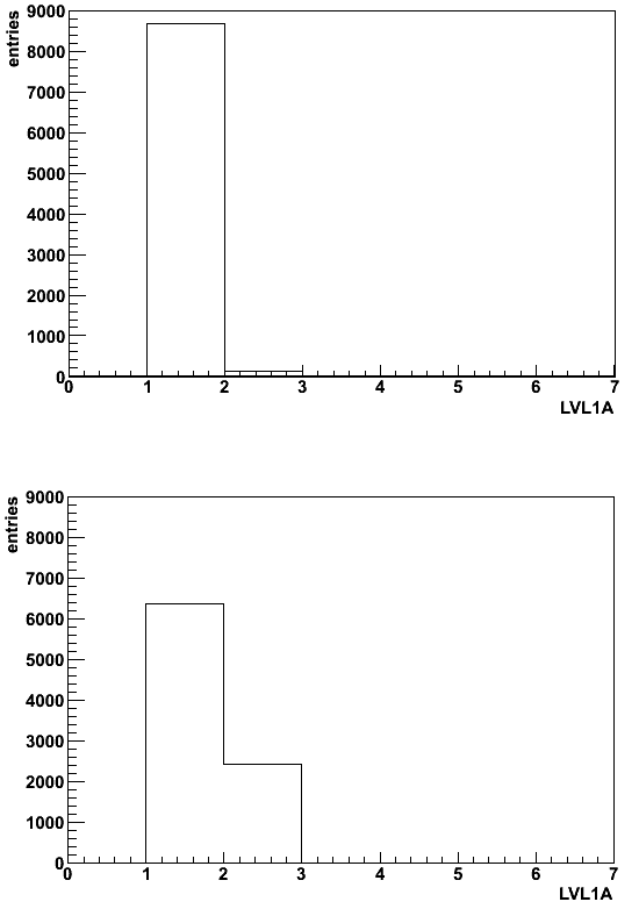

Figure 8.9: LVL1A distributions for a single pixel, recorded with 0 MCC strobe delay counts (top) and 15 delay counts (bottom). The distributions are generated using a spectrum of ToT = 6 . . . 27 BC with 400 hits per ToT.

First, a uniformly distributed ToT spectrum is simulated in the range ToT = 5.5 . . . 27.5 BC. The simulation is performed generating random ToT values in the given range, which follow a uniform distribution. The limits are chosen assuming that typically hits with true values ToT = $x \pm 0.5$ are assigned to ToT = x by the pixel electronics. To obtain a smoother spectrum, 50 times as many hits as contained in the LVL1A distributions are simulated. Then, the simulated spectrum is scaled down to obatin effectively the same number of hits as contained in the LVL1A distributions. The simulated ToT spectrum is shown in Fig. 8.10. The visible variations are due to the fact that the number of simulated ToT values is finite.

For each simulated hit, the ToT is converted into a delay according to eq. 8.12. As described in Section 8.4.3, the calibration parameters are used according to three different strategies. The simulated delay spectrum for a single pixel is shown in Fig. 8.11. The delay distribution is divided into bins of 0.1 ns.

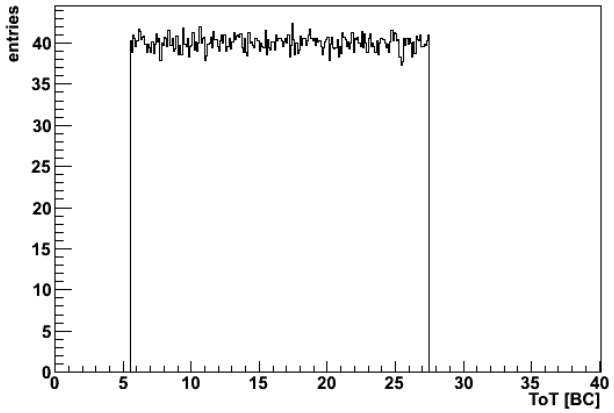

Figure 8.10: Simulated uniformly distributed ToT spectrum (ToT = 5.5 . . . 27.5 BC, scaled down to 8800 hits).

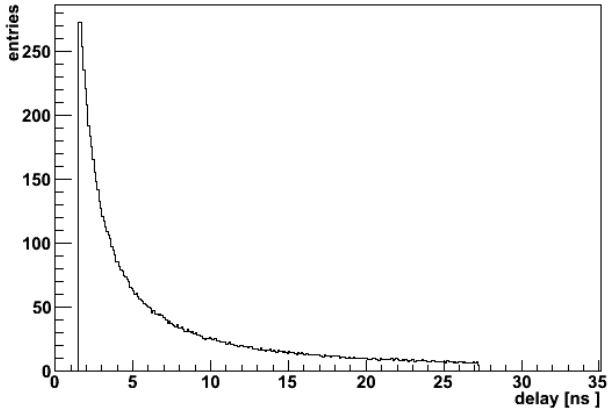

Figure 8.11: Delay distribution for the ToT spectrum shown in Fig. 8.10. The parameters for the timewalk and the ToT calibration are used according to strategy 1.

8.5.3 Fit

The delay distribution, as shown in Fig. 8.11, shows the detection times of the simulated hits. Hits with infinite charge would be detected with a delay of 0 ns. Information about the detection times is also contained in the LVL1A distribution, but in bins with a width of 25 ns (see Fig. 8.9). The delay between the beginning of a clock window and the detection of the fastest hits is determined with a fit of the simulated delay distribution to the LVL1A distribution. For the fit, the simulated delay distribution is divided into bins of 25 ns. The offset T_0 for the binning, which specifies the shift of the fine distribution against the beginning, is the fit parameter. Since the simulated delay distribution is given as a histogram and not as a smooth curve, T_0 is scanned in steps of 0.1 ns (corresponding to the bin width of the finely binned delay distribution) in a range of interest. No minimisation

algorithm is applied. The value of T_0 which has the minimum χ^2, where

$$\chi^2 = \sum_i \frac{(x_i - y_i)^2}{\sigma_{y_i}^2}, \tag{8.16}$$

is the final result. The sum is executed over all seven bins of the LVL1A distribution, x_i denotes the number of entries in bin i of the LVL1A distribution, y_i is the number of entries in bin i of the coarsely binned simulated delay distribution and σ_i^2 is the statistical error of y_i. Since the total number of entries n in the simulated spectrum is fixed ($n = 8800$) and the values of n and y_i are correlated, Poissonian errors are not appropriate. As it is used for efficiency calculations, the error of y_i is given by [UX07]

$$\sigma_{y_i}^2 = \left(\frac{(y_i + 1)\,(y_i + 2)}{(n + 2)\,(n + 3)} - \frac{(y_i + 1)^2}{(n + 2)^2} \right) n^2. \tag{8.17}$$

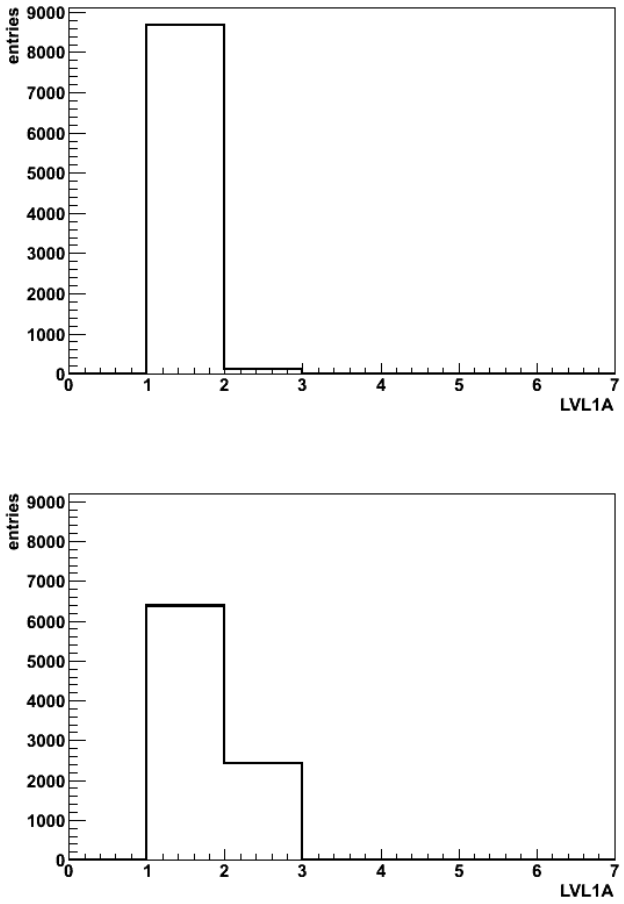

Figure 8.12: LVL1A distributions of a single pixel as shown in Fig. 8.9, with the fit of the simulated delay spectrum. The upper plot shows a measurement with 0 delay counts, while the lower plot shows a measurement with 15 delay counts. The simulated distribution fits well the LVL1A distribution, differences are not visible.

Figure 8.12 shows the LVL1A distributions of a single pixel of module M512555 for measurements with 0 and 15 delay counts (as shown in Fig. 8.9) with the fit of the simulated delay distribution. The χ^2 curves, which are minimised for the fit shown in Fig. 8.12, are shown in Fig. 8.13. The minimum χ^2 is low (almost zero) and thus the fit and the real LVL1A distribution can not be distinguished. This is in general the case for LVL1A distributions having entries in only two bins. In contrast to that, some LVL1A distributions have entries in three bins. For those histrograms, some fits deliver higher χ^2 values. An example is shown in Fig. 8.14, which depicts the LVL1A distribution and the χ^2 curve of a single pixel of module M512555 for a measurement with 20 delay counts. The reason for the failing of the fit is not completely understood. One reason might be that the parameterisation of timewalk and ToT calibration does not work well for low charges and hence the simulated delay distribution does not agree with the realistic spectrum exactly. The results of fits with $\chi^2_{min} \geq 1000$ are discarded and not considered for the further analysis.

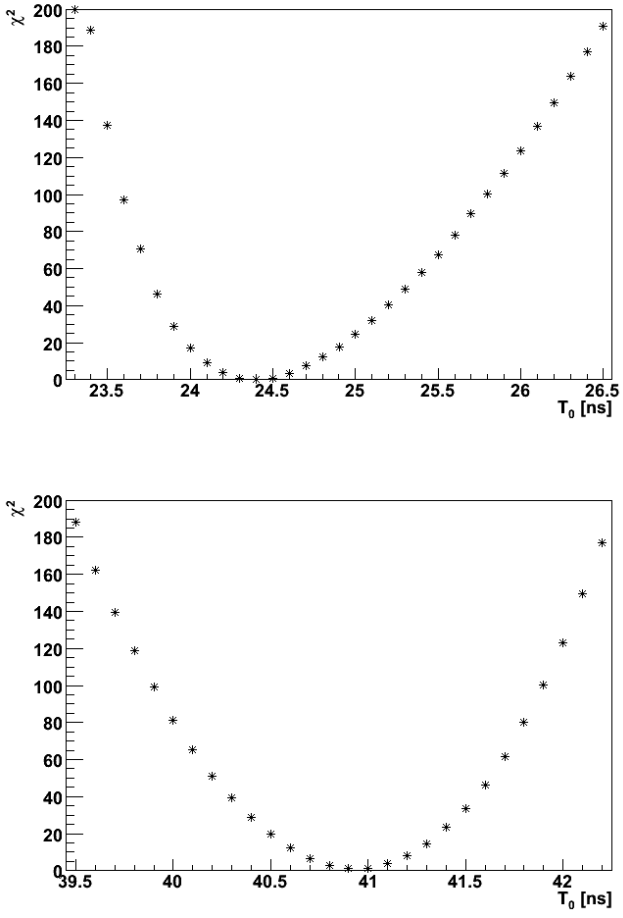

Figure 8.13: χ^2 curves of the fits shown in Fig. 8.12. The upper plot belongs to the measurement with 0 delay counts, the lower plot belongs to the measurement with 15 delay counts.

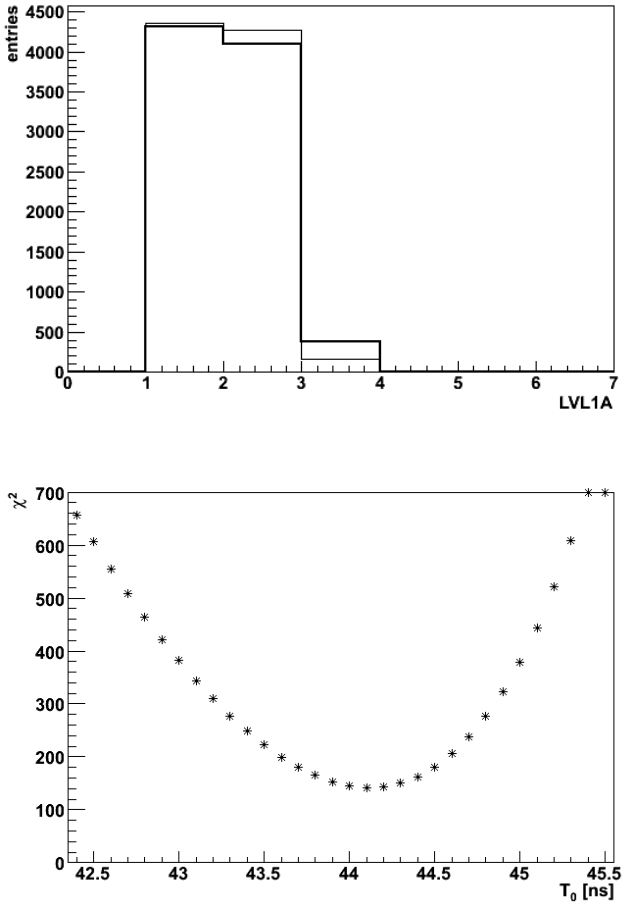

Figure 8.14: LVL1A distribution with the fit of the simulated delay distribution (top) and χ^2-curve (bottom) for a single pixel. The data are taken from a measurement with 20 delay counts and show significant deviations between the fit and the LVL1A distribution.

8.5.4 Error Analysis

The error of T_0 consists of three contributions:

- a systematic uncertainty σ_{sys}, induced by the parameterisations of the ToT calibration and the timewalk,
- a statistical error σ_{fit}, calculated from the width of the χ^2 curve of the fit,
- an error σ_{res}, given by the finite resolution of the simulated delay distribution.

The total error $\sigma^{\pm}_{T_0}$, which is asymmetric, is given by

$$\begin{aligned} (\sigma^{-}_{T_0})^2 &= (\sigma^{-}_{sys})^2 + (\sigma^{-}_{fit})^2 + \sigma^2_{res}, \\ (\sigma^{+}_{T_0})^2 &= (\sigma^{+}_{sys})^2 + (\sigma^{+}_{fit})^2 + \sigma^2_{res}. \end{aligned} \tag{8.18}$$

The determination of each of the three contributions is explained below. The quadratic addition of the asymmetric errors is actually not correct, as discussed in [Bar04], where

also an approach for a correct combination of asymmetric errors is described. However, this effort lies beyond the scope of this thesis and the variations of the results are expected to be negligible. To estimate the effect, the complete analysis was executed once by using the smallest contribution of $\sigma^-_{T_0}$ and $\sigma^+_{T_0}$ and once by using the largest contribution of $\sigma^-_{T_0}$ and $\sigma^+_{T_0}$ for the errors in both directions. The final result, the systematic error of the LVL1A fit method, did not show significant deviations. Thus, it is restricted to the combination of the asymmtetric errors given in eq. 8.18.

Systematic Uncertainties

The systematic uncertainties σ_{sys} are the dominating contributions to the total error. For their determination, the simulated delay distribution, as shown in Fig. 8.11, is generated two more times: one sample is filled with $delay - \sigma_{delay}$, while the other one is filled with $delay + \sigma_{delay}$. As described above, the value of *delay* is calculated for each simulated hit. The error of *delay*, σ_{delay}, is given by the error propagation of the errors of the ToT value and the parameters for the ToT calibration and the timewalk parameterisation. The value of *delay* is given by eq. 8.12 as a function of the simulated ToT value, the ToT calibration parameters A, C, E and the timewalk parameters P_0 and P_1:

$$delay = delay\ (ToT, A, C, E, P_0, P_1). \tag{8.19}$$

The error of *delay* is calculated considering the covariance matrices obtained from the ToT calibration and from the timewalk fit [Bra99]:

$$\sigma^2_{delay} = TCT^T. \tag{8.20}$$

T is the transformation vector containing the partial derivatives of the delay with respect to the parameters and C is the covariance matrix:

$$T = \left(\frac{\partial\, delay}{\partial\, ToT}, \frac{\partial\, delay}{\partial\, A}, \frac{\partial\, delay}{\partial\, C}, \frac{\partial\, delay}{\partial\, E}, \frac{\partial\, delay}{\partial\, P_0}, \frac{\partial\, delay}{\partial\, P_1} \right), \tag{8.21}$$

$$C = \begin{pmatrix} \sigma^2_{ToT} & 0 & 0 & 0 & 0 & 0 \\ 0 & \sigma^2_A & \mathrm{cov}(A,C) & \mathrm{cov}(A,E) & 0 & 0 \\ 0 & \mathrm{cov}(A,C) & \sigma^2_C & \mathrm{cov}(C,E) & 0 & 0 \\ 0 & \mathrm{cov}(A,E) & \mathrm{cov}(C,E) & \sigma^2_E & 0 & 0 \\ 0 & 0 & 0 & 0 & \sigma^2_{P_0} & \mathrm{cov}(P_0,P_1) \\ 0 & 0 & 0 & 0 & \mathrm{cov}(P_0,P_1) & \sigma^2_{P_1} \end{pmatrix}. \tag{8.22}$$

Since the parameters of the ToT calibration are not correlated with the parameters of the timewalk parameterisation, many entries of the covariance matrix C are zero. Furthermore, the ToT value is not correlated with any of the other variables. Since the ToT value is given by the simulation, the error σ_{ToT} is set to zero. The errors of the parameters are assumed to be Gaussian distributed.

For each simulated hit, σ_{delay} is calculated according to eq. 8.20 and the two histograms for $delay \pm \sigma_{delay}$ are filled. Then, the LVL1A fit as described above is executed with

each of these delay distributions, giving the results $T_0^{+\sigma_{delay}}$ and $T_0^{-\sigma_{delay}}$. The differences between them and T_0 give the systematic uncertainty:

$$\begin{aligned} \sigma_{sys}^{-} &= T_0 - T_0^{+\sigma_{delay}}, \\ \sigma_{sys}^{+} &= T_0^{-\sigma_{delay}} - T_0. \end{aligned} \tag{8.23}$$

Figure 8.15 shows the delay distributions obtained for $delay+\sigma_{delay}$ (top) and $delay-\sigma_{delay}$ (bottom). The errors σ_{sys}^{+} and σ_{sys}^{-} are in general asymmetric.

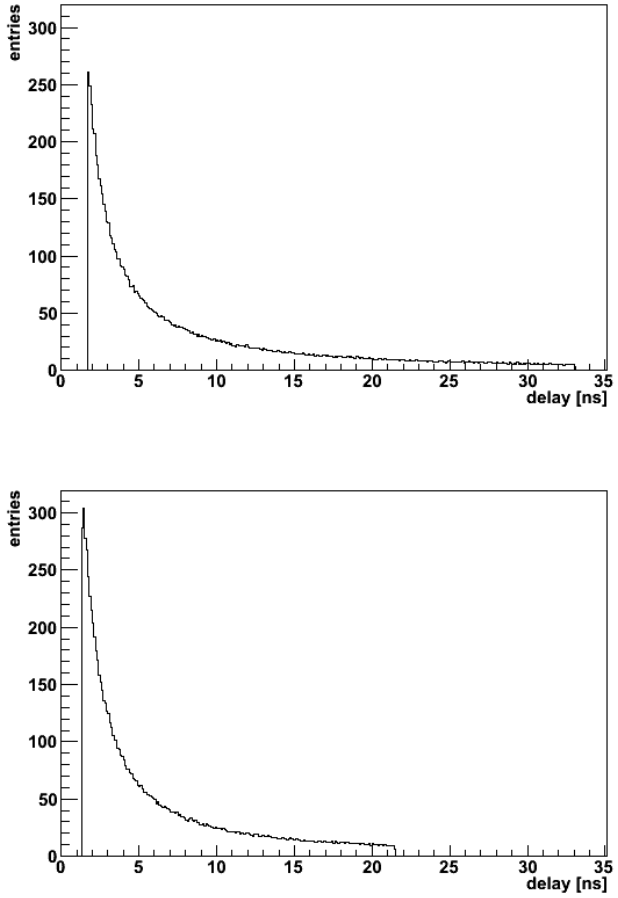

Figure 8.15: Simulated delay spectra of a single pixel for the determination of the systematic uncertainties: the upper plot shows the distribution of $delay + \sigma_{delay}$, the lower plot shows the distribution of $delay - \sigma_{delay}$. The distributions are generated using strategy 1 for the calibration parameters.

Fit Error

The limits for the statistical error induced by the fit, $\sigma_{fit}^{\pm}$, are given by the points where χ^2_{min} rises by 1. Since the simulation of the delay distribution is performed in bins of 0.1 ns, the T_0 for $\chi^2_{min} + 1$ can never be determined exactly (the χ^2 curve is a step function).

The bin which shows a χ^2 closest to $\chi^2_{min} + 1$ is selected as the lower bound T_0^- for the low error and (in the other direction) as the upper bound T_0^+ for the high error. The asymmetric fit error is given by

$$\begin{aligned} \sigma_{fit}^- &= T_0 - T_0^-, \\ \sigma_{fit}^+ &= T_0^+ - T_0. \end{aligned} \tag{8.24}$$

The error is given with a resolution of 0.1 ns. The values of $\sigma_{fit}^{\pm}$ for all investigated pixels vary between 0.0 ns and 0.4 ns.

Resolution Error

The third contribution to the error comes from the resolution of the simulated delay distribution. Assuming a uniform probability distribution of T_0 in a bin of 0.1 ns width, the error is given by

$$\sigma_{res} = \frac{0.1}{\sqrt{12}} \text{ ns} = 0.03 \text{ ns}. \tag{8.25}$$

Figure 8.16 shows the distributions of the errors $\sigma_{T_0}^{\pm}$ for the three different simulation strategies. The errors for strategy 1 (timewalk from timewalk scan, ToT parameters on pixel level) are larger than the errors for the other strategies. This has several reasons. Firstly, the parameters for the conversion of the overdrive into the timewalk parameters, used in strategies 2 and 3, are regarded to be errorless, since errors are not available. Secondly, the error of the charge (10%) for the timewalk fit and the ToT calibration is a rough estimation and may be too high. The errors for strategy 1 are reduced considerably, if a smaller error of the charge is used for the timewalk fit and for the ToT calibration. This affects less strategies 2 and 3, since they do not use the parameters from the timewalk fit.

8.5.5 Results

Figure 8.17 shows the T_0 results as a function of the pixel number (see Section 8.2.2) for all investigated pixels of module M512906. Pixels with even numbers (filled squares) are long pixels, pixels with odd numbers (unfilled squares) are normal pixels. The plot contains the results of the measurements with different delay settings (0, 7, 10, 15, 20 delay counts from the bottom to the top). For the simulation, the calibration parameters are calculated according to strategy 2. For a few data points, the LVL1A fit did not work ($\chi^2_{min} \geq 1000$). These points are not shown in Fig. 8.17. A straight line is fitted to the data points of each delay setting. The T_0 results show a good agreement with the horizontal fits.

The asymmetric structure of the errors is visible. The low errors of some results of the measurement with zero delay counts are very small compared to the high errors. One reason is the asymmetric shape of the χ^2 curve of the LVL1A fit. Lower values of T_0 would lead to entries in LVL1A bin 0 of the coarsely binned simulated delay distribution. Since the simulated delay distribution (see Fig. 8.11) has a peak at low delays, the number of entries in LVL1A bin 0 of the simulated spectrum would increase rapidly, even for a small variation of T_0. Since the measured LVL1A distribution has no entries in bin 0, the χ^2

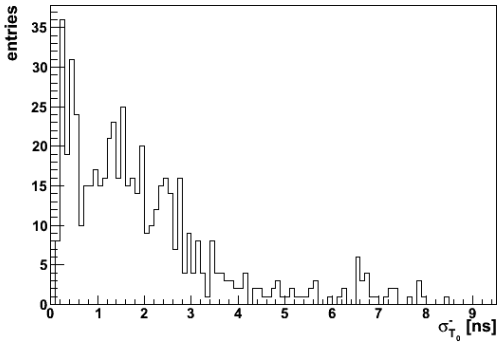

(a) $\sigma^-_{T_0}$, strategy 1

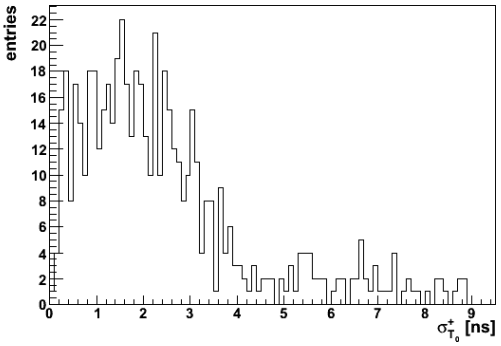

(b) $\sigma^+_{T_0}$, strategy 1

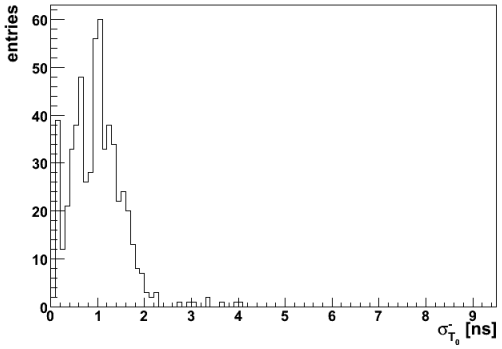

(c) $\sigma^-_{T_0}$, strategy 2

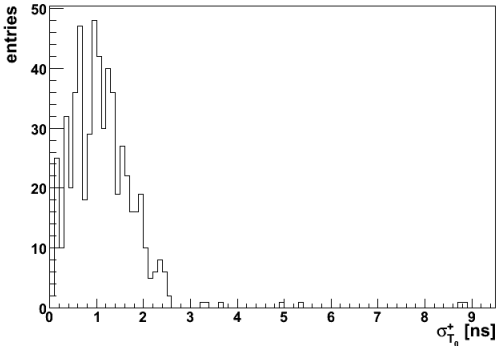

(d) $\sigma^+_{T_0}$, strategy 2

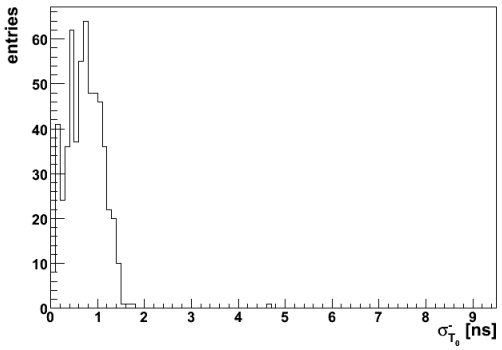

(e) $\sigma^-_{T_0}$, strategy 3

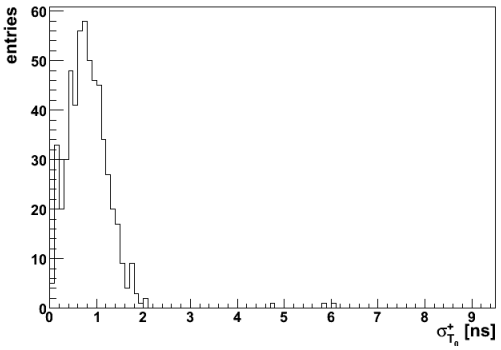

(f) $\sigma^+_{T_0}$, strategy 3

Figure 8.16: Distributions of the total errors $\sigma^-_{T_0}$ and $\sigma^+_{T_0}$ determined with the LVL1A fit method for three different strategies. The distributions contain the measurements from all pixels with all investigated delay adjustments, which have passed the cut $\chi^2 < 1000$.

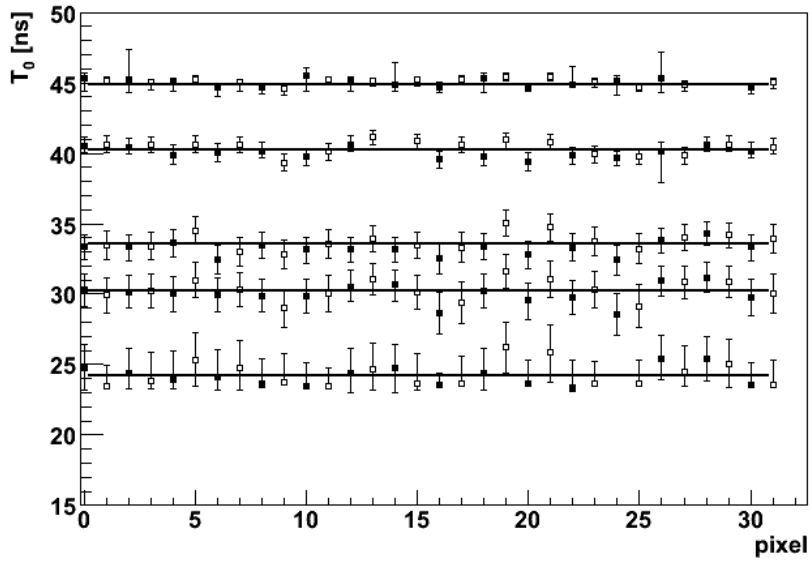

Figure 8.17: T_0 results as a function of the pixel number of module M512906 for all delay adjustments, determined with the LVL1A fit method. Filled squares indicate long pixels, unfilled squares indicate normal pixels. The horizontal lines show a fit on the data points corresponding to the same delay setting: 0, 7, 10, 15, 20 delay counts from the bottom to the top.

curve has a steep slope left to the minimum.

Also, the contribution of the systematic uncertainties to the low error of those pixels is small. The simulated delay spectrum of $delay + \sigma_{delay}$ (see Fig. 8.15), which is relevant for the determination of the low error, is broader than the distribution of the mean delay. The fit of this broader spectrum would normally cause a lower T_0 in order to obtain the same number of hits in LVL1A bin 1. Since the position of the left edge of the simulated delay distribution does not change markedly, a lower T_0 would lead to entries in LVL1A bin 0. In contrast to that, the distribution of $delay - \sigma_{delay}$, which is relevant for the high error, is more narrow. The LVL1A fit of this distribution results in a higher T_0.

In general, the errors decrease with increasing T_0, because the LVL1A distributions measured with larger delays have more entries in bin 2. Thus, when dividing the finely binned simulated delay distribution into coarse bins, the edge between bin 1 and bin 2 moves to the steeper part of the simulated delay spectrum. This reduces the width of the χ^2 curve and the systematic uncertainties, since a small variation of T_0 results in a large variation of the entries in the bins of the coarse delay distribution. However, the errors of some pixels (numbers 2, 26 and 14) are markedly large for the measurements with 15 or 20 delay counts. The LVL1A fit of these pixels, executed for the determination of the systematic uncertainties, shows an abnormally high χ^2.

To investigate the systematic error of the LVL1A fit method, the weighted means of T_0,

Module	Delay Counts	T_0^{true} [ns]	T_0 [ns]		
			Strategy 1	Strategy 2	Strategy 3
M510571	0	28.334 ± 0.002	27.9 ± 0.5	28.4 ± 0.3	27.8 ± 0.2
	7	35.560 ± 0.002	32.7 ± 0.3	33.3 ± 0.2	33.3 ± 0.1
	10	38.656 ± 0.003	37.2 ± 0.2	37.5 ± 0.2	37.2 ± 0.1
	15	43.817 ± 0.003	43.55 ± 0.09	43.5 ± 0.1	43.4 ± 0.1
	20	48.978 ± 0.003	47.73 ± 0.04	47.70 ± 0.02	47.77 ± 0.01
M512555	0	26.284 ± 0.003	23.6 ± 0.1	25.3 ± 0.3	25.8 ± 0.2
	7	33.327 ± 0.003	30.4 ± 0.5	31.5 ± 0.2	31.8 ± 0.2
	10	36.346 ± 0.003	33.4 ± 0.4	34.2 ± 0.2	34.4 ± 0.2
	15	41.377 ± 0.003	40.9 ± 0.2	41.1 ± 0.1	41.62 ± 0.07
	20	46.408 ± 0.003	44.9 ± 0.1	45.08 ± 0.07	44.77 ± 0.07
M512906	0	26.008 ± 0.003	23.78 ± 0.06	24.2 ± 0.3	23.7 ± 0.1
	7	33.015 ± 0.003	30.0 ± 0.7	30.3 ± 0.2	30.3 ± 0.2
	10	36.017 ± 0.003	33.7 ± 0.5	33.5 ± 0.2	33.6 ± 0.1
	15	41.022 ± 0.003	40.7 ± 0.3	40.3 ± 0.1	40.27 ± 0.08
	20	46.026 ± 0.004	45.4 ± 0.1	44.88 ± 0.06	44.73 ± 0.04
M512936	0	29.582 ± 0.003	28.5 ± 0.4	28.8 ± 0.2	29.1 ± 0.2
	7	37.422 ± 0.003	35.0 ± 0.3	35.1 ± 0.2	35.1 ± 0.1
	10	40.782 ± 0.003	40.0 ± 0.2	40.1 ± 0.1	39.7 ± 0.1
	15	46.382 ± 0.003	44.9 ± 0.1	44.62 ± 0.09	44.46 ± 0.06
	20	51.982 ± 0.004	51.3 ± 0.5	51.9 ± 0.3	51.9 ± 0.2

Table 8.5: Results of the LVL1A fit method: adjusted delays T_0^{true}, given by eq. 8.1, and calculated delays T_0, which are the weighted means of the T_0 results of all investigated pixels in a module. The errors of T_0^{true} are given by eq. 8.2, the errors of T_0 are the errors of the weighted means.

determined with the horizontal fits as shown in figure 8.17, are compared to the adjusted delays T_0^{true}, given by eq. 8.1. Table 8.5 summarises the adjusted delays and the calculated delays. Figure 8.18 shows the deviation between T_0^{true} and T_0, given by

$$deviation = T_0^{true} - T_0, \tag{8.26}$$

as a function of the adjusted delay for the three different strategies. Each plot shows the calculated deviations for the four investigated modules, measured with the five different delay adjustments. The indicated errors are delivered by horizontal fits to T_0 per module for one delay adjustment. The errors of T_0^{true} are neglected, since they are small compared to the errors of T_0 (see Table 8.5). The systematic error of the LVL1A fit method is given by the weighted mean of the deviation:

$$\overline{x} = \frac{\sum_i x_i/\sigma_i^2}{\sum_i 1/\sigma_i^2}. \tag{8.27}$$

A measure of the dispersion of the systematic error is the standard deviation, given by the square root of the weighted sample variance. An unbiased estimator for the variance

is given by

$$\sigma_x^2 = \frac{\sum_i 1/\sigma_i^2}{\left(\sum_i 1/\sigma_i^2\right)^2 - \sum_i 1/\sigma_i^4} \sum_i \frac{(x_i - \overline{x})^2}{\sigma_i^2}. \tag{8.28}$$

Table 8.6 summarises the results. The determined accuracies for the three strategies agree within the one sigma confidence interval. Using averaged calibration parameters (strategy 3) has a non-detrimental effect on the results.

Calibration Strategy	Systematic Error [ns]
Strategy 1	1.5 ± 0.8
Strategy 2	1.3 ± 0.5
Strategy 3	1.2 ± 0.6

Table 8.6: LVL1A fit method: systematic error and standard deviation for the three strategies used to determine the calibration parameters.

As can be seen in Fig. 8.18, the deviations show oscillations and a systematic shift to positive values. Apparently, the oscillations have the same origin as the oscillations of the difference between the delays measured with the timewalk scan and the timewalk fit function (see Section 6.4, Fig. 6.9). These oscillations imply that the delay given by eq. 8.12 yields oscillating deviations from the true value. A reason might be the incorrect determination of the conversion between VCAL DAC settings and charge. Probably, the deviations could be avoided using a function with more parameters for the timewalk fit.

The systematic shift of the deviation is quantified as the systematic error, see Table 8.6. It might be caused by different discriminator thresholds in the timewalk scan and in the measurements at ToothPix. As mentioned in Section 8.2.1, the threshold in the production scans, which were executed with TurboDAQ, was approximately 170 e^- higher than the threshold after tuning with STControl. A higher threshold leads to an increased timewalk for low charges, see Section 6.4, but does not influence the timewalk for high charges. Since the timewalk parameters are obtained from the timewalk scan with the higher threshold, this leads to a longer tail of the simulated delay distribution. This results in a lower T_0 from the LVL1A fit and hence to a larger difference between T_0^{true} and T_0. This effect might explain the observed shift qualitatively. However it is not clear, whether it also explains the shift quantitatively. This is not further investigated within this thesis.

As discussed in Section 8.5.4, the errors of T_0 are the largest for strategy 1 and the lowest for strategy 3. This affects the size of the errors of the deviations, which are indicated in Fig. 8.18.

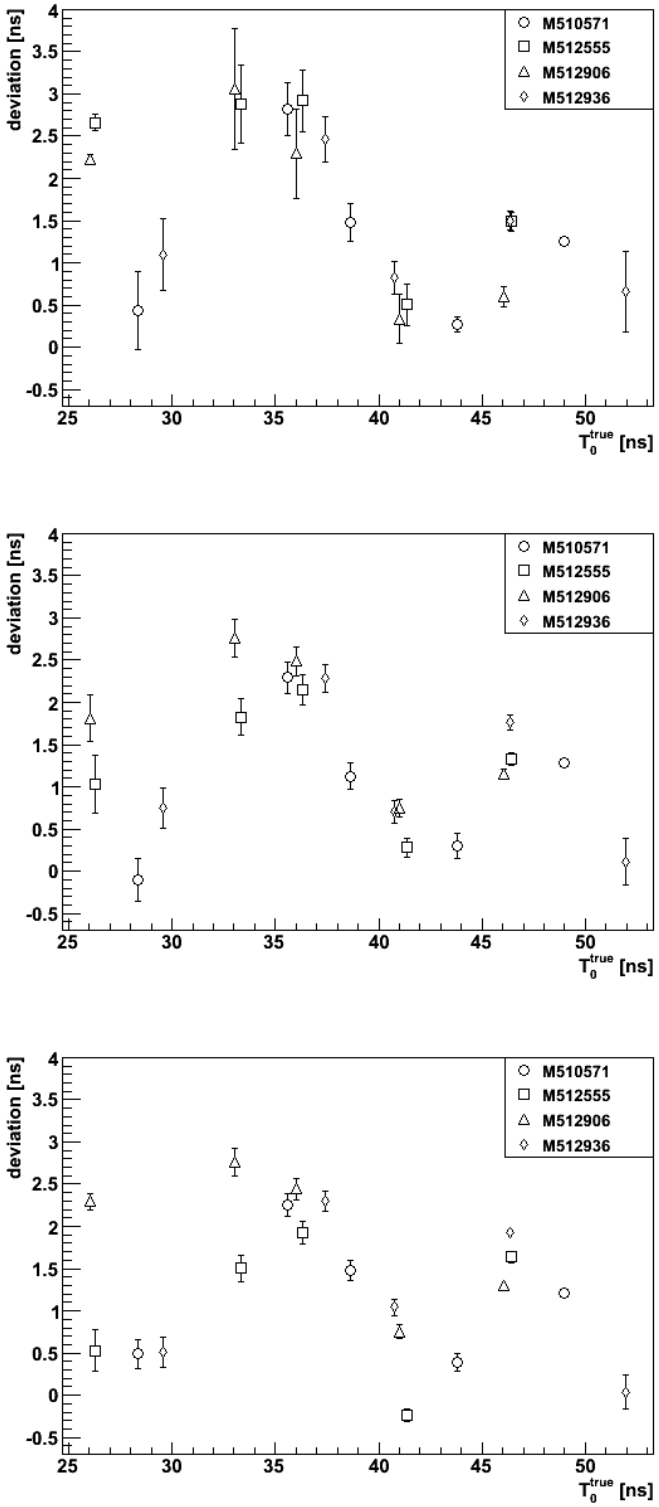

Figure 8.18: Deviation between adjusted and determined T_0, obtained with the LVL1A fit method. The simulation is performed using the calibration parameters determined with strategy 1 (top), strategy 2 (middle) and strategy 3 (bottom).

8.6 Minimum ToT Method

The minimum ToT method is another approach to determine the delay T_0 between the beginning of a clock window and the detection time of the fastest hits. It is based on the fact, that the minimum charge, which can be detected in a certain clock window, is a function of the delay T_0. This method was not applied to the data of the cosmic test (see Chapter 7) due to the low statistics of cosmic data. The achievable precision of the minimum ToT method is investigated in this section. As for the LVL1A fit method, the parameters for timewalk and ToT calibration are obtained according to three different strategies, see Section 8.4.3.

8.6.1 Efficiency

For the analysis with the minimum ToT method, a spectrum containing 400 hits per ToT (or less hits, if the pixel does not have 400 hits for a certain ToT) in the range ToT = 3 . . . 30 BC is selected. This is done for each investigated pixel separately. For each ToT value, the efficiency of the detection of a pulse in LVL1A bin 1 is calculated. Since hits with low ToT are detected in a later readout window, the resulting plot shows an S-curve like profile. This can be seen in Fig. 8.19, where the efficiency curves of the measurements performed with 0 MCC delay counts (top) and 15 MCC delay counts (bottom) are shown. The data obtained with measurements with more delay counts show a larger threshold ToT, above which all pulses are assigned to LVL1A bin 1. This threshold ToT corresponds to the intime threshold.
The threshold ToT is determined with an S-curve fit. As shown in Fig. 8.19, a function given by

$$E(\,ToT) = \frac{1}{2}\left(1 - \mathrm{Erf}\left(\frac{ToT_{\,min} - ToT}{\sqrt{2}\,\sigma}\right)\right) \tag{8.29}$$

is fitted to the data points, where σ indicates the width of the slope and Erf(x) = $\frac{2}{\sqrt{\pi}}\int_0^x \exp(-t^2)\,\mathrm{d}t$ is the error function. The parameter $ToT_{\,min}$ is the ToT which has an efficiency of 50%. The fit is accomplished using the method of least squares. Measurements with $\chi^2_{min} > 50$ are discarded.

The ToT bins are centred at integer values. Since the total number of selected pulses per ToT value is fixed (usually $n = 400$) and the number of hits k in LVL1A bin 1 is correlated with n, Poissonian errors are not appropriate for the efficiency. The error of the efficiency $E(\,ToT)$ is given by [UX07]

$$\sigma_E^2 = \frac{(k+1)\,(k+2)}{(n+2)\,(n+3)} - \frac{(k+1)^2}{(n+2)^2}. \tag{8.30}$$

The extracted value $ToT_{\,min}$ is converted into a delay according to eq. 8.12, which results in the delay between the detection of the fastest hits and the detection of hits with $ToT = ToT_{\,min}$. Since hits with $ToT = ToT_{\,min}$ are detected at the end of LVL1A bin 1, the time between the beginning of LVL1A bin 0 and the detection of the fastest hits is given by

$$T_0 = 50\ \mathrm{ns} - delay\,(\,ToT_{\,min}). \tag{8.31}$$

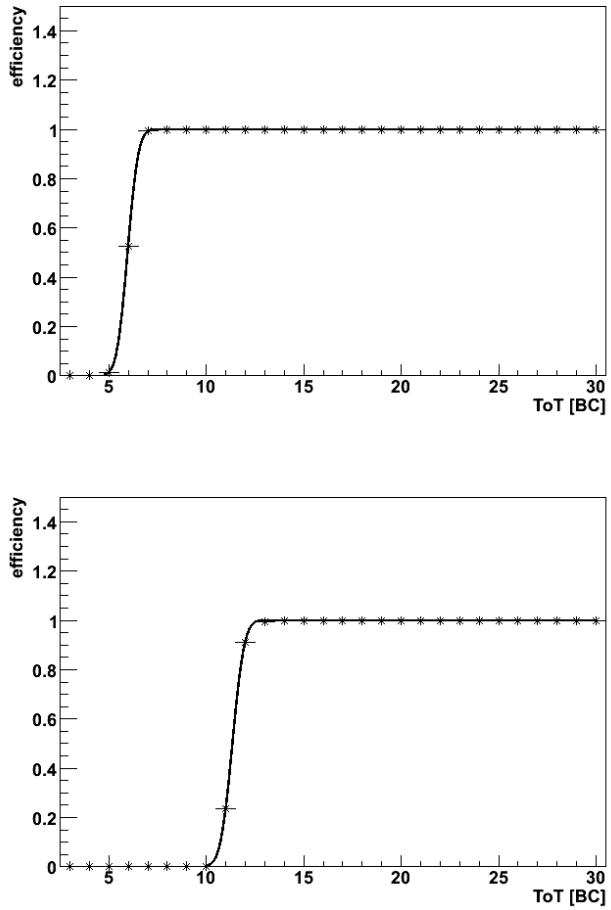

Figure 8.19: Efficiency of detection of a pulse in LVL1A bin 1 against ToT, with S-curve fit according to eq. 8.29. The upper plot shows a measurement with 0 delay counts, the lower plot shows a measurement with 15 delay counts.

8.6.2 Error Analysis

The error of T_0 is given by the error of $delay\,(ToT_{min})$:

$$\sigma_{T_0} = \sigma_{delay}, \tag{8.32}$$

where σ_{delay} is calculated according to eq. 8.20 with the transformation vector given in eq. 8.21 and the covariance matrix given in eq. 8.22. In contrast to the LVL1A fit method, the error of the ToT value, σ_{ToT}, is nonzero for the minimum ToT method. It includes a statistical component and a systematic component.

The statistical component σ^{stat}_{ToT} is the fit error of ToT_{min} from the S-curve fit to the efficiency. The systematic component is determined by executing the S-curve fit twice, once with the parameter σ in eq. 8.29 fixed to $\sigma_{fit} + \Delta\sigma_{fit}$ and once with σ fixed to $\sigma_{fit} - \Delta\sigma_{fit}$, where σ_{fit} is the fit result of the parameter σ from the initial fit and $\Delta\sigma_{fit}$ is its fit error. The results for an efficiency of 50% of these fits, ToT^{-}_{min} and ToT^{+}_{min}, differ

slightly from ToT_{min} determined in the initial fit. The systematic error is then given by

$$\sigma_{ToT}^{sys} = |ToT_{min}^{\pm} - ToT_{min}|, \tag{8.33}$$

where the one of ToT_{min}^{+} or ToT_{min}^{-} is used, which shows the largest deviation from ToT_{min}. Although the systematic error is actually asymmetric, this operation delivers a symmetric error. It has no effect on the results, considering the fact that the systematic error is small compared to the statistical error. The distribution of σ_{ToT}^{stat} and σ_{ToT}^{sys} is shown in Fig. 8.20. This systematic error gives an estimate of the uncertainty induced by the fact, that the real efficiency curve does not show an exact S-curve like profile. The total error of ToT is

$$\sigma_{ToT}^{2} = (\sigma_{ToT}^{stat})^2 + (\sigma_{ToT}^{sys})^2. \tag{8.34}$$

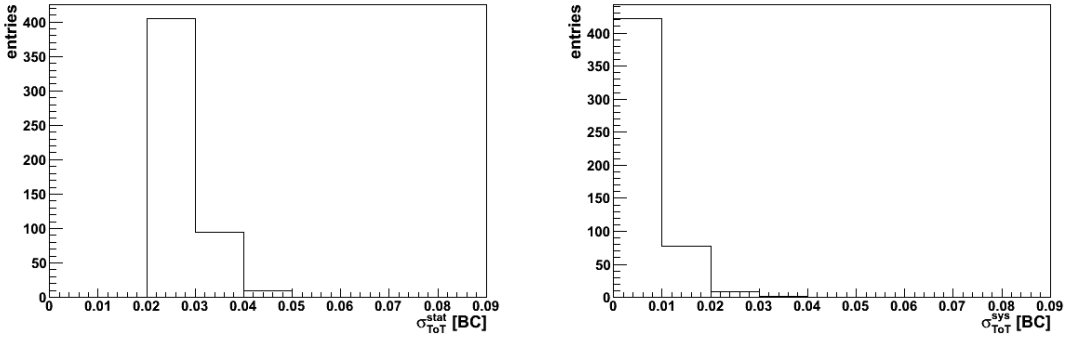

Figure 8.20: Distributions of the error of ToT_{min}: Statistical component σ_{ToT}^{stat} (left) and systematic component σ_{ToT}^{stat} (right).

Figure 8.21 shows the distribution of the errors σ_{T_0} for the three different strategies. As for the error of T_0 determined with the LVL1A method, the error of strategy 1 is the largest, due to the same reasons.

8.6.3 Results

Similarly to Fig. 8.18 for the LVL1A fit, Fig. 8.22 shows the T_0 results for module M512906, obtained with the minimum ToT method (strategy 2). The horizontal lines are fitted to the data points for each delay adjustment. The data points show a good agreement with the fits. The errors decrease with increasing delay.

Table 8.7 summarises the adjusted delays T_0^{true}, given by eq. 8.1, and the determined delays T_0. The T_0 results given are the weighted means of all investigated pixels in a module, determined with horizontal fits as shown in Fig. 8.22. The indicated errors are the fit errors of the horizontal fits. Results for the measurement with 20 MCC delay counts for module M512936 are missing since the fastest hits in this case are determined in LVL1A bin 2, which is not analysed.

The deviations between T_0^{true} and T_0 are shown in figure 8.23 for the three different strategies. The accuracies for the three different strategies, given by the weighted means of the

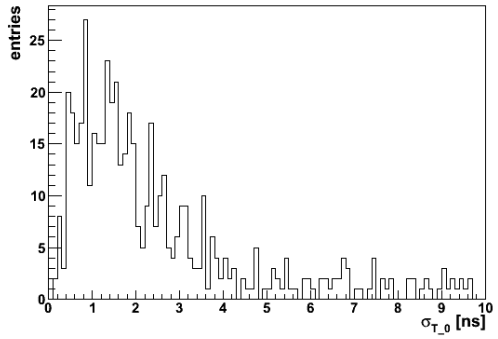

(a) σ_{T_0}, strategy 1

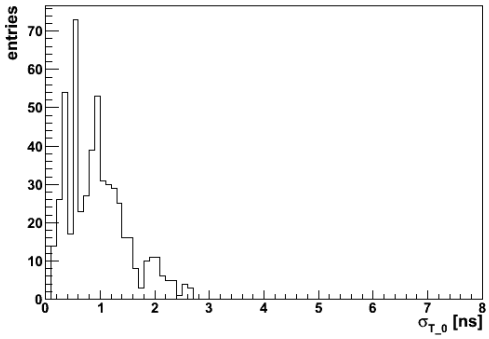

(b) σ_{T_0}, strategy 2

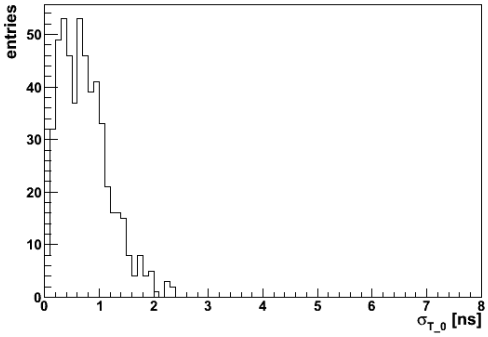

(c) σ_{T_0}, strategy 3

Figure 8.21: Distributions of the error σ_{T_0} determined with the minimum ToT method for the three different strategies.

deviation (eq. 8.27), are summarised in Table 8.8. The indicated errors are the unbiased estimators for the standard deviations, given by eq. 8.28. These values are measures of the precision. The results of the three strategies agree within the one sigma confidence interval.

Similarly to the LVL1A fit method, the deviations in Fig. 8.23 show a systematic shift in positive direction and oscillations. The oscillations have the maxima and minima at the same delays for all methods. The reasons are assumed to be the same as for the LVL1A fit method. Although T_0 is determined differently with the minimum ToT method, the shift could also be caused by the threshold difference between production measurements and the measurements at ToothPix: the higher threshold in the timewalk scan results in larger delays for low charges. According to eq. 8.31, this results in a lower T_0 and hence in a larger difference between T_0^{true} and T_0. The standard deviation of the deviation is the largest for strategy 1 and the lowest for strategy 3. Obviously, using averaged calibration parameters has a non-detrimental effect on the results.

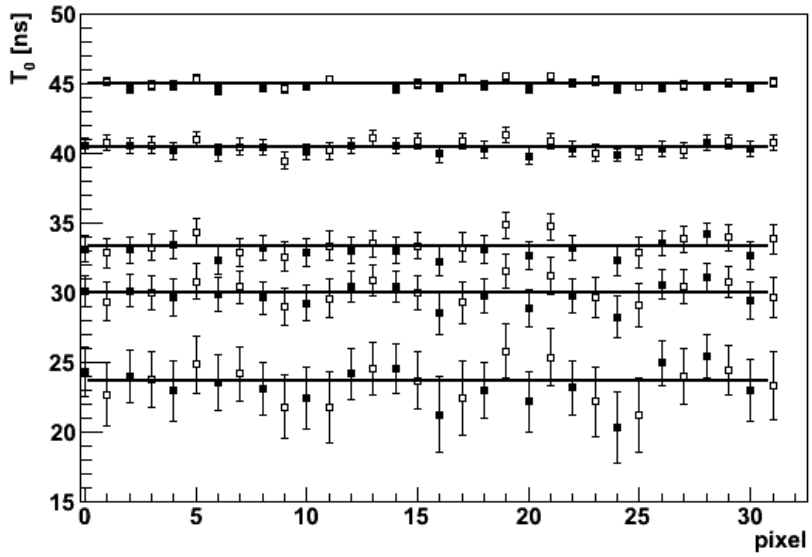

Figure 8.22: T_0 results as a function of the pixel number of module M512906 for each delay setting, determined with the minimum ToT method, strategy 2. Filled squares indicate long pixels, unfilled squares indicate normal pixels. The horizontal lines show a fit to the data points corresponding to the same delay setting: 0, 7, 10, 15, 20 delay counts from the bottom to the top.

Module	Delay Counts	T_0^{true} [ns]	T_0 [ns]		
			Strategy 1	Strategy 2	Strategy 3
M510571	0	28.334 ± 0.002	27.5 ± 0.5	28.2 ± 0.3	28.4 ± 0.2
	7	35.560 ± 0.002	32.6 ± 0.3	33.1 ± 0.2	33.3 ± 0.1
	10	38.656 ± 0.003	37.0 ± 0.2	37.4 ± 0.1	37.4 ± 0.1
	15	43.817 ± 0.003	43.3 ± 0.1	43.37 ± 0.09	43.40 ± 0.06
	20	48.978 ± 0.003	47.75 ± 0.07	47.82 ± 0.04	47.86 ± 0.03
M512555	0	26.284 ± 0.003	23.6 ± 0.8	24.9 ± 0.4	25.4 ± 0.3
	7	33.327 ± 0.003	30.2 ± 0.5	31.3 ± 0.2	31.5 ± 0.2
	10	36.346 ± 0.003	33.4 ± 0.4	34.2 ± 0.2	34.4 ± 0.1
	15	41.377 ± 0.003	40.8 ± 0.2	41.2 ± 0.1	41.23 ± 0.07
	20	46.408 ± 0.003	44.9 ± 0.1	45.06 ± 0.06	45.08 ± 0.04
M512906	0	26.008 ± 0.003	22.8 ± 1.3	23.7 ± 0.4	23.7 ± 0.37
	7	33.015 ± 0.003	29.8 ± 0.7	30.0 ± 0.2	30.1 ± 0.2
	10	36.017 ± 0.003	33.5 ± 0.5	33.3 ± 0.2	33.4 ± 0.1
	15	41.022 ± 0.003	40.9 ± 0.3	40.4 ± 0.1	40.40 ± 0.08
	20	46.026 ± 0.004	45.4 ± 0.2	44.94 ± 0.06	44.90 ± 0.04
M512936	0	29.582 ± 0.003	28.3 ± 0.4	28.6 ± 0.2	28.7 ± 0.2
	7	37.422 ± 0.003	34.8 ± 0.2	35.0 ± 0.2	35.0 ± 0.1
	10	40.782 ± 0.003	39.9 ± 0.2	40.0 ± 0.1	39.90 ± 0.08
	15	46.382 ± 0.003	44.8 ± 0.1	44.83 ± 0.07	44.70 ± 0.05
	20	46.382 ± 0.003	–	–	–

Table 8.7: Results of the minimum ToT method: adjusted delays T_0^{true}, given by eq. 8.1, and calculated delays T_0, which are the weighted means of the T_0 results of all investigated pixels in a module. The errors of T_0^{true} are given by eq. 8.2, the errors of T_0 are the errors of the weighted means.

Calibration Strategy	Systematic Error [ns]
Strategy 1	1.3 ± 0.7
Strategy 2	1.2 ± 0.6
Strategy 3	1.2 ± 0.5

Table 8.8: Minimum ToT method: systematic error and standard deviation for the three strategies used to determine the calibration parameters.

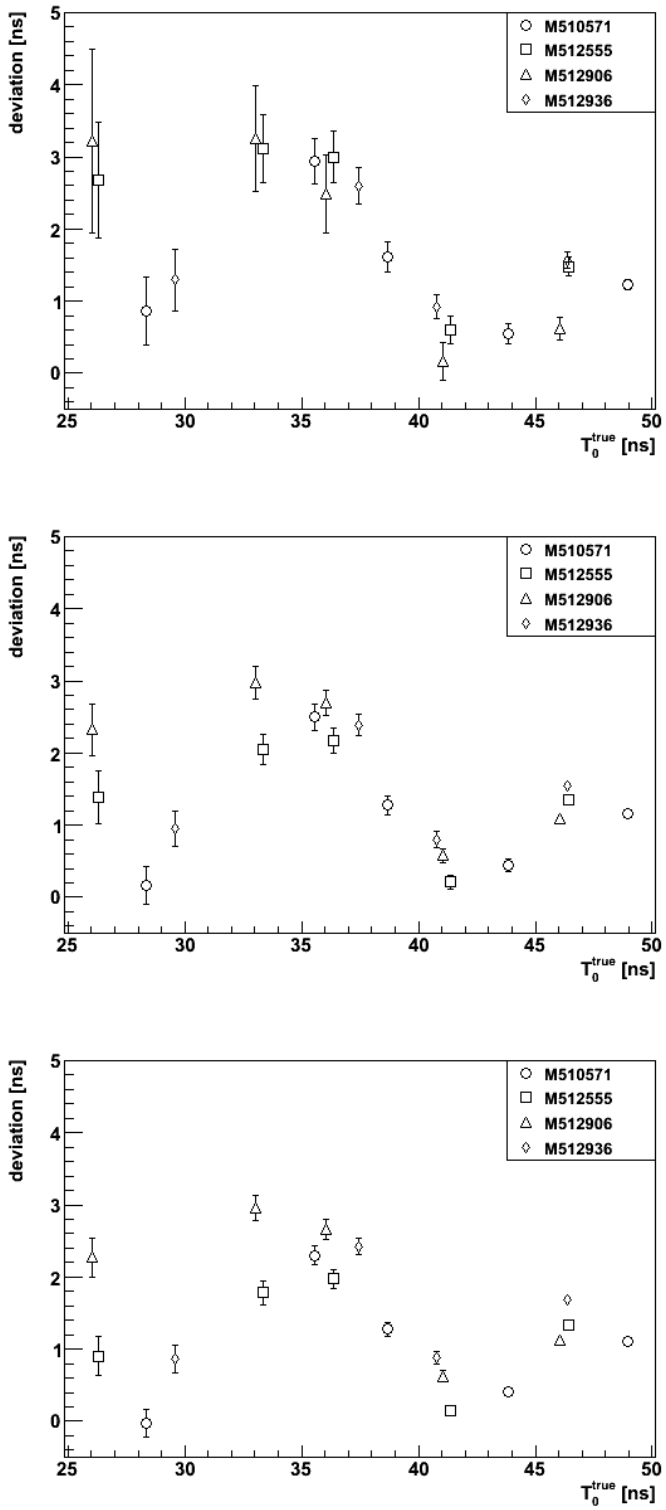

Figure 8.23: Difference between adjusted and determined T_0, obtained with the minimum ToT method. The calibration parameters are determined with strategy 1 (top), strategy 2 (middle) and strategy 3 (bottom).

Chapter 9

Conclusion and Outlook

One of the challenges for the detectors at the LHC is the high bunch crossing rate of 40 MHz. For each event, only the hits assigned to one clock window can be read out. This requires strategies to adjust the timing for each sub-detector. This thesis investigated the timing behaviour of the ATLAS Pixel Detector.

Chapter 6 described the general timing problem of the Pixel Detector and options to adjust the timing. The underlying effect, the timewalk effect, was described and the behaviour of timing related features of the Pixel Detector at different temperatures was studied. For this purpose, timing related calibration scans were performed for temperatures between $T \approx -10°\mathrm{C}$ and $T \approx +23°\mathrm{C}$. These investigations are of particular interest for the timing studies described in Chapter 8. The timing studies use a parameterisation of the timewalk obtained with timewalk scans from the production measurements at $T \approx -10°\mathrm{C}$ as input for the analysis of measurements performed at $T \approx +23°\mathrm{C}$.

The behaviour of the MCC strobe mechanism, which triggers the injection of calibration pulses in the pixel cell, was found to exhibit a dependency on the temperature. The calibration strobe signal can be delayed by specifying a number of delay counts and a delay range, which determines the delay per delay count. Investigated measures are (1) the delay t_0 for zero delay counts between the detection of the highest charge pulses and the beginning of a certain clock window and (2) the delay per MCC strobe delay count. For the delay t_0, a temperature dependency of $\Delta t_0 = (-4.982 \pm 0.003) \times 10^{-2}$ ns/°C was determined. It is the weighted mean of the values obtained for two pixel modules. The delay per MCC strobe delay count for delay range five was found to increase with increasing temperature by $(1.4 \pm 1.9) \times 10^{-3}$ ns/°C, which is the weighted mean of four investigated modules. The quoted values were determined with the analogue T0 scan.

The timewalk effect showed a slight temperature dependency for pulses with charge $8000\ e^- < Q < 15000\ e^-$. However, these deviations are assumed to be negligible for the studies presented in Chapter 8. The timewalk parameterisation used for these studies is given as a fit to the data obtained with the timewalk scan. The deviations between the data points and the fit value are larger than the deviations between measurements at different temperatures.

The investigations of the timing behaviour at different temperatures revealed problems, when delay range six is employed during timing related calibration scans. Probably, the results of the calibration measurements executed with delay range six are not reliable. It is assumed that the TurboDAQ software, which was used for production measurements, handles measurements with delay range six incorrectly.

To achieve a correct assignment of hits to their bunch crossings, the timing has to be adjusted by delaying the clock signal for each pixel module separately. The required delay settings can be obtained with an analysis, which determines the delay between the beginning of a clock window and the detection of the highest charge hits. Such studies were overviewed in Chapter 7 for data from the cosmics test. In Chapter 8, the systematic error of the method applied was investigated.

These investigations are based on data from test measurements executed at the Pixel Detector test setup ToothPix at CERN. The measurements consist of data sets with different delay adjustments. The analysis was executed and the calculated delay was compared to the adjusted delay. Two methods to determine the delay were investigated: the LVL1A fit method (which was applied to the data from the cosmics test) and the minimum ToT method. For both methods, three strategies to determine the calibration parameters, which are required as input, were applied:

1. timewalk parameters determined from the timewalk scan on pixel level, ToT calibration parameters calculated on pixel level,

2. timewalk parameters calculated from the overdrive on pixel level, ToT calibration parameters calculated on pixel level,

3. timewalk parameters calculated from the mean overdrive per FE chip, ToT calibration parameters averaged over the two investigated pixels per FE chip.

The results for the systematic error are summarised in Table 9.1.

Calibration Strategy	Systematic Error [ns] (LVL1A fit)	Systematic Error [ns] (Minimum ToT)
Strategy 1	1.5 ± 0.8	1.3 ± 0.7
Strategy 2	1.3 ± 0.5	1.2 ± 0.6
Strategy 3	1.2 ± 0.6	1.2 ± 0.5

Table 9.1: Determined systematic error and standard deviation of the LVL1A fit method and the minimum ToT method for the three strategies, which are used to determine the calibration parameters.

The systematic errors and the standard deviations of the two methods are comparable. For the analysis of data delivered by the real ATLAS Pixel Detector, the calibration parameters will be available on FE chip level, similarly to strategy 3. The comparison between the determined delay and the adjusted delay revealed systematic effects: a constant shift, which influences the determined value of the systematic error, and oscillations,

which influence the standard deviation. The constant shift is assumed to be due to a difference between the discriminator threshold during the measurements at ToothPix and in the timewalk scan of the production measurements, from which the timewalk parameters were extracted. The oscillations are assumed to be caused by an intrinsic difference between the delays measured in the timewalk scan and the fit to these data points.

Outlook

Both methods investigated to determine the delay use the number of hits detected in several consecutive clock windows. Thus, it is not possible to use these methods at a bunch crossing rate of 40 MHz, when only one clock window is read out. However, during the commissioning phase, the bunch crossing rate at the LHC will be less than 40 MHz and the Pixel Detector can read out several consecutive clock windows for each event selected by a LVL1 trigger decision. The necessary timing adjustments should be determined during this phase. Once adjusted, the timing is assumed to be stable, but changes are possible after irradiation.

To monitor the timing during operation with a bunch crossing rate of 40 MHz and only one readout window, modified methods are necessary. One option could be to apply the minimum ToT method using hits of the first and second bunch crossing after a gap in the LHC bunch train (see Chapter 2). The hits with low ToT values originating from the collisions of the first bunch crossing after a gap are detected in the second readout bin. Therefore, the first readout bin after a gap has no hits with low ToT. Considering an efficiency given by

$$E(ToT) = \frac{Hits_{Bin\ 1}(ToT)}{Hits_{Bin\ 1}(ToT) + Hits_{Bin\ 2}(ToT)}, \tag{9.1}$$

where $Hits_{Bin\ k}(ToT)$ is the number of hits for a given ToT detected in the readout bin k after a gap, leads to a curve as shown in Fig. 9.1. The efficiency ranges from 0 to 0.5. The minimum ToT, which is here the ToT for an efficiency of 25%, can be extracted similarly to the description in Chapter 8.

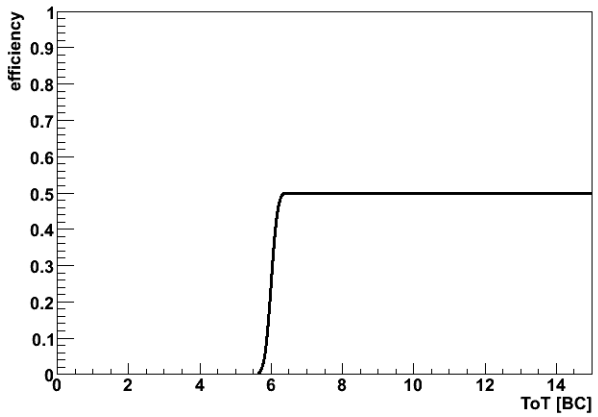

Figure 9.1: S-curve expected for the efficiency defined in eq. 9.1 (simulation).

Appendix A

Temperature Dependency of Timing Scans

A.1 Results of Timing Scans at Different Temperatures

This section contains tables with results of the timing related scans performed at different temperatures. The scans were performed with four modules, identified as M51XXXX.

M510667		M510810		M511455		M513127	
T [°C]	t_0 [ns]	T [°C]	t_0 [ns]	T [°C]	t_0 [ns]	T [°C]	t_0 [ns]
-9.9	$22.1 \pm 0.2^*$	-9.9	20.7 ± 0.2	-10.6	25.5 ± 0.3	-10.5	$19.5 \pm 0.3^*$
$+1.5$	$21.5 \pm 0.3^*$	$+1.1$	19.9 ± 0.2				
$+12.6$	$20.9 \pm 0.3^*$	$+12.0$	19.7 ± 0.4				
$+16.4$	26.9 ± 0.3	$+15.8$	19.3 ± 0.4	$+16.2$	24.2 ± 0.4	$+16.0$	24.9 ± 0.3
$+19.7$	26.5 ± 0.3	$+19.1$	19.0 ± 0.2				
$+23.4$	26.3 ± 0.2	$+22.7$	19.2 ± 0.2	$+22.9$	23.7 ± 0.2	$+22.7$	24.7 ± 0.2

Table A.1: Analogue T0 scan: temperatures and results of t_0. The values given are arithmetic means averaged over all pixels in one module. The indicated errors are standard deviations. Values marked with an asterisk are measured with delay range six, the other ones are measured with delay range five.

M510667		M513127	
T [°C]	$\frac{delay}{count}$ [ns]	T [°C]	$\frac{delay}{count}$ [ns]
-9.9	1.020	-10.5	1.051
$+1.5$	1.038		
$+12.6$	1.059		

Table A.2: Analogue T0 scan: temperatures and delay conversion factors for delay range *six*. Errors are not available.

M510667		M510810		M511455		M513127	
T [°C]	$\frac{delay}{count}$ [ns]	T [°C]	$\frac{delay}{count}$ [ns]	T [°C]	$\frac{delay}{count}$ [ns]	T [°C]	$\frac{delay}{count}$ [ns]
−9.9	0.907	−9.9	1.124	−10.6	0.958	−10.5	0.929
+1.5	0.924	+1.1	1.132				
+12.6	0.937	+12.0	1.153				
+16.4	0.951	+15.8	1.151	+16.2	1.003	+16.0	0.960
+19.7	0.948	+19.1	1.147				
+23.4	0.958	+22.7	1.166	+22.9	1.010	+22.7	0.968

Table A.3: Analogue T0 scan: temperatures and delay conversion factors for delay range *five*. Errors are not available.

M510667			M510810		
T [°C]	*overdrive* $[e^-]$	*CNT*	T [°C]	*overdrive* $[e^-]$	*CNT*
−9.7	$1181 \pm 213^*$	27^*	−9.8	1439 ± 253	23
+1.6	$1197 \pm 207^*$	26^*	+1.1	1457 ± 249	22
+12.7	$1108 \pm 191^*$	24^*	+12.1	1450 ± 239	21
+16.5	1404 ± 216	34	+15.9	1457 ± 236	21
+19.8	1364 ± 209	33	+19.1	1486 ± 239	21
+23.5	1411 ± 211	33	+22.8	1538 ± 241	21

M511455			M513127		
T [°C]	*overdrive* $[e^-]$	*CNT*	T [°C]	*overdrive* $[e^-]$	*CNT*
−10.5	1306 ± 201	32	−10.5	$1206 \pm 188^*$	23^*
+16.4	1333 ± 189	29	+16.0	1471 ± 201	31
+23.0	1320 ± 185	28	+22.8	1502 ± 202	31

Table A.4: Intime threshold scan: temperatures, overdrive and MCC delay counts (denoted as *CNT*). For the overdrive, arithmetic mean values, averaged over all pixels of one module, and standard deviations are given. Overdrive and MCC delay counts marked with an asterisk correspond to measurements with delay range six, the other ones are measured with delay range five.

M510667			M510810		
T [°C]	*overdrive* $[e^-]$	$t_0 - 20$ ns [ns]	T [°C]	*overdrive* $[e^-]$	$t_0 - 20$ ns [ns]
-9.8	$1077 \pm 120^*$	$24.3 \pm 0.3^*$	-9.9	1397 ± 167	25.8 ± 0.3
$+1.5$	$1087 \pm 115^*$	$23.8 \pm 0.2^*$	$+1.0$	1404 ± 167	24.9 ± 0.3
$+12.7$	$1095 \pm 110^*$	$23.0 \pm 0.3^*$	$+12.1$	1429 ± 152	24.8 ± 0.4
$+16.4$	1329 ± 133	31.9 ± 0.2	$+15.9$	1426 ± 165	24.4 ± 0.2
$+19.8$	1327 ± 126	31.5 ± 0.5	$+19.1$	1428 ± 157	24.0 ± 0.2
$+23.4$	1335 ± 129	31.4 ± 0.2	$+22.7$	1466 ± 146	24.2 ± 0.4

M511455			M513127		
T [°C]	*overdrive* $[e^-]$	$t_0 - 20$ ns [ns]	T [°C]	*overdrive* $[e^-]$	$t_0 - 20$ ns [ns]
-10.6	1243 ± 140	30.5 ± 0.3	-10.5	$1184 \pm 137^*$	$21.6 \pm 0.2^*$
$+16.3$	1285 ± 128	29.2 ± 0.3	$+15.9$	1455 ± 144	29.8 ± 0.3
$+22.9$	1297 ± 128	28.8 ± 0.3	$+22.7$	1456 ± 141	29.5 ± 0.3

Table A.5: Timewalk scan: temperatures, overdrive and $t_0 - 20$ ns. For $t_0 - 20$ ns, arithmetic mean values, averaged over all pixels of one module, and standard deviations are given. The overdrive is averaged over all normal pixels of one module. Values of overdrive and $t_0 - 20$ ns marked with an asterisk correspond to measurements with delay range six, the other ones are measured with delay range five.

A.2 MCC Strobe Delay Line Calibration with TurboDAQ

This section gives a technical description of the delay line calibration with TurboDAQ. The problems encountered when delay range six is used (see Section 6.5), are further investigated. All discussions are based on the TurboDAQ source code, release 6.6.

Figure A.1: Three relevant readout bins for the analogue T0 scan: The fastest hits cross the threshold typically at the marked position (for zero delay counts). At the bottom, the first readout window for different trigger delays is indicated.

The delay line calibration is implemented in the function `int Twalk(...)`, which is contained in the file `TurboDAQ_primitives.c`. A preliminary analogue T0 scan is executed for trigger delays 250, 251 and 252 (see fig. A.1). Initially, these scans are performed with delay range five. For each trigger delay, pulses with high charge ($Q \approx 100000\ e^-$) are injected and the number of delay counts is scanned from zero to 63. The efficiency of detected pulses as function of the delay time is fitted with an S-curve, as explained in Section 6.3.2. Since the conversion from delay counts into "real" ns it not yet known in this stage, the delay counts are multiplied by a default value. The default values are assigned in the function `int InitialiseStructuresPortable(void)`, contained in the file `utilities.c`. The values are 1.11 ns for delay range five and 1.25 ns for delay range six. The function `int UpdateCalibrations(void)`, in file `pixana.c`, sets the previously assigned factors to scale the MCC delay counts for the S-curve fit. The fit results of these preliminary analogue T0 scans are saved in so-called scratch data files, which are not part of the production data base. Therefore, it is not possible to access the sratch data files of all production tests.

For each trigger delay, the number of pixels with good fits is counted – a fit is "good", if its χ^2 is below a certain threshold. The results of the S-curve fit for either trigger delay 250 or 252 (the one with more good fitted pixels) is used for the delay line calibration, together with the results of trigger delay 251. In the example of figure A.1, the number of good fits is certainly higher for trigger delay 252, since the hits are already detected with trigger delay 250 if zero delay counts are applied and an hence an S-curve fit is not possible. The delay conversion factor (in ns/counts), as taken from the function `int Twalk(...)`, is

$$\texttt{module\_general.strobe\_delay\_cal[constradd->mcc\_delay\_range]} = \texttt{25.0/(mean\_sd\_252} - \texttt{mean\_sd\_251)}, \tag{A.1}$$

where `mean_sd_25X` denotes the arithmetic mean (averaged over all pixels with good fit) of the delays for trigger delay 25X, converted back into delay counts. For the conversion

back into delay counts, the default conversion factor is used again. Then, it is checked whether the delay per count is big enough. The total delay achievable with 63 counts should be long enough to execute a timewalk scan, which uses trigger delay 252. If the condition

$$63 * \texttt{module\_general.strobe\_delay\_cal}[\texttt{constradd->mcc\_delay\_range}] < \texttt{T0} + 30 \tag{A.2}$$

is fulfiled, the preliminary T0 scans, as described above, are executed again for stepwise increased delay ranges (up to range nine) until the condition in eq. A.2 is false. The second factor in eq. A.2 specifies the delay per delay count, as calculated with eq. A.1. The value for T0 is calculated by TurboDAQ as

$$\texttt{T0} = \texttt{mean\_sd\_251}/ \texttt{module\_general.strobe\_delay\_cal}[\texttt{constradd->mcc\_delay\_range}]. \tag{A.3}$$

T0, as used in the condition in eq. A.2, is expected to be given in units of ns. However, eq. A.3 divides a value given in counts by a value given in ns/counts. This seems to be incorrect – a multiplication is expected. A delay per count for delay range five of smaller than 1 ns causes that the calculated value for T0 is smaller than it should be. Hence, the condition in eq. A.2 is true more often and delay range six is calibrated more often than actually necessary. This is for example the case for the measurement of module M513127 at $T = -10.5°\text{C}$: A multiplication in eq. A.3 would not have initiated the employment of delay range six.

Once the condition in eq. A.2 is found to be false, the final analogue T0 scan is performed with the lastly calibrated delay range. For the S-curve fit, the delay counts are no longer scaled with the predefined delay values, but with the determined values for the delay per delay count. The results of this scan, which are given in units of "real" ns, are stored in the production database and can be evaluated with ModuleAnalysis. If a timewalk scan or an intime threshold scan is executed, the delay line calibration can either be performed initially or be taken from a previously executed analogue T0 scan. Hence, all timing scans are based on the same strategy for the delay line calibration.

The reason for the strange behaviour when delay range six is used could not be pinpointed. However, a hypothesis could be established which can explain the observed behaviour. Suppose that the delay line calibration works fine up to the point before the final T0 scan. The next task for TurboDAQ is to set the scale factor for the MCC strobe delay counts as the determined value of delay per count. If this scale factor is set to the value determined for delay range five, even if delay range six is used, the observed behaviour can be understood. As an example, the measurements of module M510667 at $T = -9.9°\text{C}$ are discussed. The other measurements with delay range six show the same behaviour.

The scratch data from the preliminary T0 scan with trigger delay 251 and delay range six show a mean value $t_0 \approx 30.5$ – the unit of which is neither real ns nor MCC delay counts, as explained above. Dividing this by 1.25, the default conversion factor for delay range six, yields $t_0 \approx 24.4$ counts. Multiplying it by 0.907 ns/count, the determined value of delay

per count for delay range *five*, one obtains $t_0 \approx 22.1$ ns. This is exactly the value which is given as the result of the analogue T0 scan for delay range *six* (see Table A.1). The correct mean value should be a multiplication of the number of delay counts and the delay per count for delay range six, which is 1.02 ns/count: $t_0 \approx 24.4 \text{ counts} \cdot 1.02 \frac{\text{ns}}{\text{count}} = 24.9$ ns. This comes closer to the result obtained during the T0 scan at $T = 16.4°\text{C}$ with delay range five, which is $t_0 = 26.9$ ns. Indeed, there is still a difference, but this might be caused by a different offset of the delay ranges.

The delay for the intime threshold scan was set to 27 counts (see Table A.4). This value can be explained if TurboDAQ adds 5 ns (which is correct so far) to the incorrect T0 result and converts this back into delay counts, but now using the conversion for delay range *six*: $t_0 = (22.1 + 5) \text{ ns}/1.02 \frac{\text{ns}}{\text{count}} \approx 27$ counts. The correct delay, following the hypothesis, would be $t_0 = (24.9 + 5) \text{ ns}/1.02 \frac{\text{ns}}{\text{count}} \approx 29$ counts. Therefore, the charge injections for the intime threshold scan happen about two ns too early. This explains that the overdrive measured with delay range six is lower than the overdrive measured with delay range five (see fig. 6.12).

The hypothesis seems to explain the strange behaviour observed when switching between delay range five and delay range six. However, it has to be emphasised that it is only an assumption which is only motivated by the results. The real reason, why the conversion within TurboDAQ may fail, could not be clarified.

Appendix B

Threshold Scan

This appendix contains a plot showing the threshold distribution after threshold tuning obtained with TurboDAQ (fig. B.1). As mentioned in Section 8.2.1, the threshold tuning with TurboDAQ results in a higher threshold than the desired threshold and shows a larger dispersion than a threshold tuning with STControl.

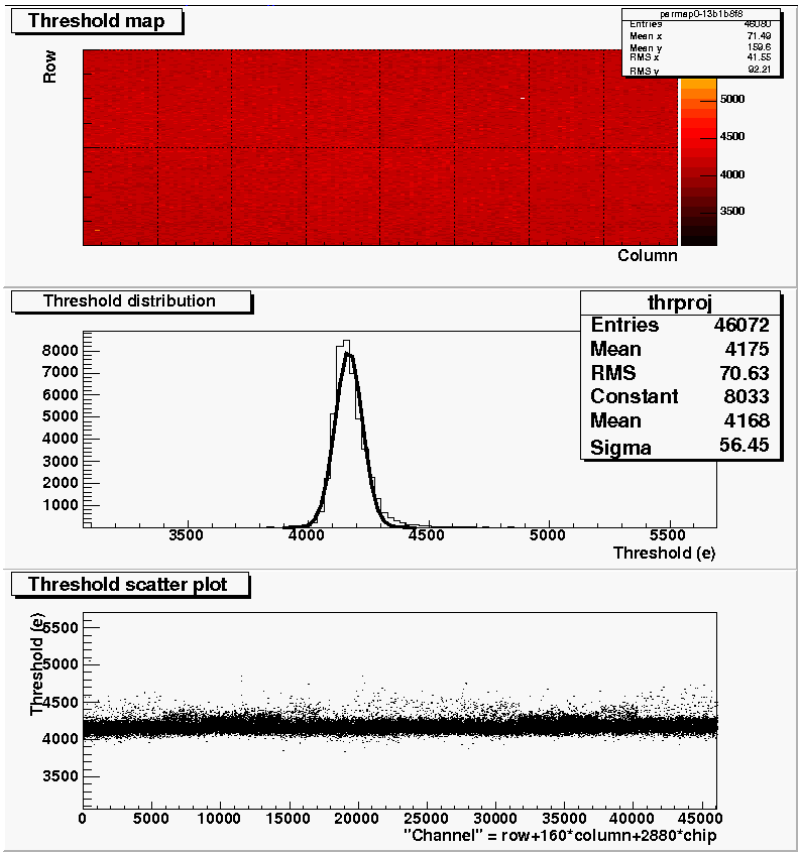

Figure B.1: Threshold scan performed with TurboDAQ, production test: Threshold mean of module M512555 after threshold tuning. In the upper plot, a two-dimensional map of the threshold for each pixel is shown. The middle plot displays a histogram of the same values. The lower plot shows the threshold as a function of the pixel number.

Acronyms and Abbreviations

Notation	Description
ALICE	A Large Ion Collider Experiment
ATLAS	A Toroidal LHC Aparatus
BC	Bunch Crossing
BCID	Bunch Crossing Identifier
BCR	Bunch Counter Reset
BOC	Back Of Crate
BPM	Biphase Mark
CERN	Conseil Européen pour la Recherche Nucléaire (European Organization for Nuclear Research)
CMOS	Complementary Metal–Oxide–Semiconductor
CMS	Compact Muon Solenoid
CSC	Cathode Strip Chamber
CTP	Central Trigger Processor
DAC	Digital Analogue Converter
DAQ	Data Acquisition
DCS	Detector Control System
DORIC	Digital Opto Receiver Integrated Circuit
DSP	Digital Signal Processor
EB	Event Builder
ECR	Event Counter Reset
EF	Event Filter
EM	Electromagnetic
EoC	End of Column
FCal	Forward Calorimeter
FE	Front-End
Fermilab	Fermi National Accelerator Laboratory
FIFO	First In, First Out
HEC	Hadronic End-Cap Calorimeter

Notation	Description
HLT	High Level Trigger
ID	Inner Detector
L1ID	Level 1 (Trigger) Identifier
LAr	Liquid Argon
LEP	Large Electron-Positron Collider
LHC	Large Hadron Collider
LHCb	Large Hadron Collider beauty
LHCf	Large Hadron Collider forward
LTP	Local Trigger Processor
LVDS	Low Voltage Differential Signaling
LVL1	Level 1 (Trigger)
LVL1A	LVL1 Trigger Accept
LVL2	Level 2 (Trigger)
MCC	Module Controller Chip
MDT	Monitored Drift Tube
MIP	Minimum Ionising Particle
$\overline{\text{MS}}$	Modified Minimal Subtraction
MSR	Mark Space Ratio
NIM	Nuclear Instrumentation Standard
PS	Proton Synchrotron
PSB	Proton Synchrotron Booster
pSQP	prototype Service Quarter Panel
RAM	Random Access Memory
RF	Radio Frequency
ROB	Readout Buffer
ROD	Readout Driver
RoI	Region of Interest
ROS	Readout System
RPC	Resistive Plate Chamber
S-LINK	Simple-Link
SCT	Semiconductor Tracker
SEU	Single Event Upset
SM	Standard Model
SPS	Super Proton Synchrotron
TGC	Thin Gap Chamber
TileCal	Tile Calorimeter
TIM	TTC Interface Module

Notation	Description
TMT	Thermal Management Tile
ToothPix	The out of the hole Pixel Detector
ToT	Time over Threshold
TOTEM	Total Cross Section, Elastic Scattering and Diffraction Dissociation at the LHC
TRT	Transition Radiation Tracker
TTC	Timing, Trigger and Control
TTCex	TTC encoder and transmitter
TTCvi	TTC VME interface
VCSEL	Vertical Cavity Surface Emitting Laser
VDC	VCSEL Driver Chip
VME	Versa Module Eurocard

Bibliography

[A+05a] P. B. Amaral et al., *The ATLAS Local Trigger Processor (LTP)*, IEEE Trans. Nucl. Sci. **52** (2005), 1202–1206.

[A+05b] A. Andreazza et al., *ATLAS Pixel Module Electrical Tests Description*, ATL-IP-QP-0144, CERN, Geneva, 2005.

[A+05c] K. E. Arms et al., *ATLAS Pixel Opto-Electronics*, Nucl. Instrum. Methods Phys. Res., A **554** (2005), 458–468. 14 p.

[A+07a] M. Aharrouche et al., *Response Uniformity of the ATLAS Liquid Argon Electromagnetic Calorimeter*, Nucl. Instrum. Methods Phys. Res., A **582** (2007), 429–455.

[A+07b] A. Ahmad et al., *The Silicon Microstrip Sensors of the ATLAS Semiconductor Tracker*, Nucl. Instrum. Methods Phys. Res., A **578** (2007), 98–118.

[A+07c] G. Arduini et al., *Alternative Bunch Filling Schemes for the LHC*, CERN-LHC-Project-note-401, CERN, Mar 2007.

[A+08a] G. Aad et al., *ATLAS Pixel Detector Electronics and Sensors*, Journal of Instrumentation **3** (2008), no. 07, P07007.

[A+08b] E. Abat et al., *The ATLAS Transition Radiation Tracker (TRT) Proportional Drift Tube: Design and Performance*, J. Instrum. **3** (2008), P02013.

[A+08c] J. P. Archambault et al., *Energy calibration of the ATLAS Liquid Argon Forward Calorimeter*, J. Instrum. **3** (2008), P02002.

[ATL96a] ATLAS Collaboration, *ATLAS Calorimeter Performance: Technical Design Report*, CERN-LHCC-96-040, CERN, Geneva, 1996.

[ATL96b] ATLAS Collaboration, *ATLAS Liquid-Argon Calorimeter: Technical Design Report*, CERN-LHCC-96-041, CERN, Geneva, 1996.

[ATL96c] ATLAS Collaboration, *ATLAS Tile Calorimeter: Technical Design Report*, CERN-LHCC-96-042, CERN, Geneva, 1996.

[ATL97a] ATLAS Collaboration, *ATLAS Inner Detector: Technical Design Report, 1*, CERN-LHCC-97-016, CERN, Geneva, 1997.

[ATL97b] ATLAS Collaboration, *ATLAS Inner Detector: Technical Design Report, 2*, CERN-LHCC-97-017, CERN, Geneva, 1997.

[ATL97c] ATLAS Collaboration, *ATLAS Muon Spectrometer: Technical Design Report*, CERN-LHCC-97-022, CERN, Geneva, 1997.

[ATL98a] ATLAS Collaboration, *ATLAS Level 1 Trigger: Technical Design Report*, CERN-LHCC-98-014, CERN, Geneva, 1998.

[ATL98b] ATLAS Collaboration, *ATLAS Pixel Petector: Technical Design Report*, CERN-LHCC-98-013, CERN, Geneva, 1998.

[ATL98c] ATLAS Collaboration, *ATLAS Trigger Performance: Status Report*, CERN-LHCC-98-015, CERN, Geneva, 1998.

[ATL03] ATLAS Collaboration, *ATLAS High Level Trigger, Data Acquisition and Controls: Technical Design Report*, CERN-LHCC-2003-022, CERN, Geneva, 2003.

[ATL07] ATLAS Pixel Collaboration, *Pixel Offline Analysis for EndcapA Cosmic Data*, ATL-INDET-PUB-2008-003, CERN, Geneva, Dec 2007.

[ATL08] ATLAS Collaboration, *The ATLAS Experiment at the CERN Large Hadron Collider*, Submitted to JINST for publication, 2008.

[B+02] R. Beccherle et al., *MCC: The Module Controller Chip for the ATLAS Pixel Detector*, Nucl. Instrum. Methods Phys. Res., A **492** (2002), 117–133.

[B+04a] M. Benedikt et al., *LHC Design Report, Vol. 3: The LHC Injector Chain*, CERN-2004-003-V-3, CERN, Geneva, 2004.

[B+04b] O. S. Bruening et al., *LHC Design Report, Vol. 1: The LHC Main Ring*, CERN-2004-003-V-1, CERN, Geneva, 2004.

[B+04c] O. S. Bruening et al., *LHC Design Report, Vol.2: The LHC Infrastructure and General Services*, CERN-2004-003-V-2, CERN, Geneva, 2004.

[B+06] C. P. Bee et al., *The Raw Event Format in the ATLAS Trigger & DAQ*, ATL-DAQ-98-129, CERN, Geneva, Dec 2006, Major version 3.1.

[B+08] J. Biesiada et al., *ToothPix - The ATLAS Pixel Detector Test Stand in SR1*, ATL-COM-INDET-2008-008, CERN, Geneva, 2008.

[Bar04] R. Barlow, *Asymmetric Errors*, arXiv:physics/0401042v1, January 2004.

[BD04] R. Beccherle and G. Darbo, *MCC-I2.1 Specifications: Register Bank*, September 2004, http://www.ge.infn.it/ATLAS/Electronics/home.html.

[Bic88] H. Bichsel, *Straggling in Thin Silicon Detectors*, Rev. Mod. Phys. **60** (1988), 663–699.

[BL99] D. Boussard and T. P. R. Linnecar, *The LHC Superconducting RF System*, CERN-LHC-Project-Report-316, CERN, Geneva, 1999.

[Bra99] see e.g.: Siegmund Brandt, *Data Analysis: Statistical and Computational Methods for Scientists and Engineers*, third ed., Springer, New York, NY, 1999.

[C+04] M. L. Chu et al., *The Off-Detector Opto-Electronics for the Optical Links of the ATLAS Semiconductor Tracker and Pixel Detector*, Nucl. Instrum. Methods Phys. Res., A **530** (2004), 293–310.

[Col08] C. Collard (ed.), *Searches for the Higgs Boson and Extra Dimensions at the LHC*, ATL-PHYS-CONF-2008-006, Geneva, Jan 2008, Proceedings of the first AFI workshop in Innsbruck.

[D+01] B. Dowler et al., *Performance of the ATLAS Hadronic End-Cap Calorimeter in Beam Tests*, ATL-LARG-2001-019, Max-Planck Inst., Muenchen, Oct 2001.

[Djo05] A. Djouadi, *The Anatomy of Electro-Weak Symmetry Breaking. I: The Higgs Boson in the Standard Model*, hep-ph/0503172. LPT-ORSAY-2005-17, Paris 11. Lab. Phys. Théor., Orsay, 2005.

[DL07] F. De Lorenzi, *Timing Characteristics of the ATLAS Pixel Detector*, Diploma thesis, University of Milan, 2007.

[Dob07] D. A. Dobos, *Commissioning Perspectives for the ATLAS Pixel Detector*, Ph.D. thesis, Technical Univerity of Dortmund, 2007.

[Dop07] J. Dopke, *Studies for Automated Tuning of the Quality of the Back of Crate Card for the ATLAS Pixel Detector*, Diploma thesis, Univ. Wuppertal, 2007.

[F+98] Y. Fukuda et al., *Evidence for Oscillation of Atmospheric Neutrinos*, Phys. Rev. Lett. **81** (1998), no. 8, 1562–1567.

[Fer03] P. Ferrari, *Higgs Boson Searches at LEP*, hep-ex/0305039, CERN, Geneva, May 2003.

[Fis00] P. Fischer, *Pixel Electronics for the ATLAS Experiment*, Nucl. Instrum. Methods Phys. Res., A **465** (2000), no. 1, 153–8.

[Fli06] T. Flick, *Studies on the Optical Readout for the ATLAS Pixel Detector. Systematical Studies on the Functions of the Back of Crate Card and the Timing of the Pixel Detector*, Ph.D. thesis, Univ. Wuppertal, 2006.

[G+02] I. Gorelov et al., *A Measurement of Lorentz Angle and Spatial Resolution of Radiation Hard Silicon Pixel Sensors*, Nucl. Instrum. Methods Phys. Res., A **481** (2002), 204–21. 26 p.

[G+05] V. Giangiobbe et al., *Hadronic Calorimeter Performance in the ATLAS Combined Testbeam 2004*, ATL-TILECAL-PUB-2005-008, CERN, Geneva, Nov 2005.

[GK08] J. Grosse-Knetter, *Vertex Measurement at a Hadron Collider - The ATLAS Pixel Detector*, BONN IR 2008-04, University of Bonn, 2008, Habilitationsschrift.

[Gla80] S. L. Glashow, *Towards a Unified Theory: Threads in a Tapestry*, Rev. Mod. Phys. **52** (1980), no. 3, 539–543, Lectures delivered 8 Dec. 1979 at the presentation of Nobel prizes in physics.

[H+01] F. G. Huegging et al., *Prototype Performance and Design of the ATLAS Pixel Sensors*, Nucl. Instrum. Methods Phys. Res., A **465** (2001), no. 1, 77–82.

[Hau04] R. Hauser, *The ATLAS Trigger System*, Eur. Phys. J. **C34** (2004), s173–s183.

[Hig66] P. W. Higgs, *Spontaneous Symmetry Breakdown Without Massless Bosons*, Phys. Rev. **145** (1966), 1156–1163.

[Hue] F. G. Huegging, University of Bonn, private communication.

[Hue04] F. G. Huegging, *Front-End Electronics and Integration of ATLAS Pixel Modules*, Jan 2004, Presented at 12th International Workshop on Vertex Detectors, Low Wood, UK, 14 - 19 Sep 2003.

[Ibr] I. Ibragimov, University of Siegen, private communication.

[Jac05] J. N. Jackson, *The ATLAS Semiconductor Tracker (SCT)*, Nucl. Instrum. Methods Phys. Res., A **541** (2005), 89–95.

[JJF06] J. Joseph, R. Jared, and D. P. Ferguson, *ROD Operations Manual*, June 2006.

[Leo94] see e.g.: W. R. Leo, *Techniques for Nuclear and Particle Physics Experiments: a How-to Approach; 2nd ed.*, Springer, Berlin, 1994.

[Lut99] G. Lutz, *Semiconductor Radiation Detectors: Device Physics*, Springer, Berlin, 1999.

[McG05] D. P. McGinnis, *FNAL Tevatron Operational Status*, 2005, Prepared for Particle Accelerator Conference (PAC 05), Knoxville, Tennessee, 16-20 May 2005.

[Mol99] M. Moll, *Radiation Damage in Silicon Particle Detectors: Microscopic Defects and Macroscopic Properties*, Ph.D. thesis, Hamburg Univ., Hamburg, 1999.

[Per04] I. Peric, *Design and Realisation of Integrated Circuits for the Readout of Pixel Sensors in High-Energy Physics and Biomedical Imaging*, Ph.D. thesis, University of Bonn, 2004.

[Pon] M. Pontz, Master's thesis, University of Siegen, in preparation.

[PS95] M. E. Peskin and D. V. Schroeder, *An Introduction to Quantum Field Theory; 1995 ed.*, Westview, Boulder, CO, 1995.

[R+98] T. Rohe et al., *Sensor Design for the ATLAS Pixel Detector*, Nucl. Instrum. Methods Phys. Res., A **409** (1998), no. 1-3, 224–228.

[UX07] T. Ullrich and Z. Xu, *Treatment of Errors in Efficiency Calculations*, arXiv:physics/0701199v1, January 2007.

[Wei] J. Weingarten, Technical University of Dortmund, private communication.

[Wun92] R. Wunstorf, *Systematische Untersuchungen zur Strahlenresistenz von Silizium-Detektoren für die Verwendung in Hochenergiephysik-Experimenten (in German)*, Ph.D. thesis, Hamburg Univ., Hamburg, 1992.

[Wun01] R. Wunstorf, *Radiation Tolerant Sensors for the ATLAS Pixel Detector*, Nucl. Instrum. Methods Phys. Res., A **466** (2001), no. 2, 327–34.

[Y+06] W.-M. Yao et al., *Review of Particle Physics*, Journal of Physics G **33** (2006), 1+.

Acknowledgements

Many people supported me for the work for this thesis. I would like to express my gratitude especially to

- my supervisor Prof. Dr. Peter Buchholz for giving me the opportunity to work in his group and on this project, for the guidance and for arranging the extended stay at CERN,
- Prof. Dr. Markus Schumacher for the willingness to read this thesis as a co-reviewer,
- Dr. Iskander Ibragimov for the assistance throughout the entire project, for the patience with me, for arranging the measurements at the ToothPix setup and for proofreading part of this thesis,
- Dr. Wolfgang Walkowiak for – among other things – the support with the TurboDAQ measurements and for proofreading part of this thesis,
- Thorsten Stahl for the support with the TurboDAQ measurements,
- Dr. Matthew Beckingham and Mark Rodgers for proofreading part of this thesis and for helping me in numerous questions concerning grammar, phrasing and spelling,
- all people at CERN who helped me with the measurements at the ToothPix setup – especially Dr. Andrea Odino, Dr. Sara Strandberg, Nicoletta Garelli and Dr. Lucia Masetti,
- the rest of the "timing gang", Michael Pontz and Hendrik Czirr,
- my family and my friends,
- all people I forgot.

Erklärung

Hiermit erkläre ich, dass ich die vorliegende Masterarbeit selbständig verfasst und keine anderen als die angegebenen Quellen und Hilfsmittel benutzt, sowie Zitate und Ergebnisse Anderer kenntlich gemacht habe.

....
(Ort) (Datum) (Unterschrift)